1-1-2014

First-Principles Exploration of the Structural Motifs of Chalcogenides and Their Relationship to Electronic and Photovoltaic Properties

John A. Brehm
University of Pennsylvania, brehmj@sas.upenn.edu

First-Principles Exploration of the Structural Motifs of Chalcogenides and Their Relationship to Electronic and Photovoltaic Properties

Abstract
The bulk photovoltaic effect (BPVE) refers to the production of electric currents from the valence band promotion of electrons to the conduction band in a pure, undoped, and insulating material from the absorption of electromagnetic radiation. For a material to be able to create a current in response to non-polarized solar irradiation, it must be a polar compound with a band gap in the visible spectrum, 1.1 - 3.1 eV. The purpose of this work is to provide computational evidence that the pursuit of materials other than pure oxides for use as bulk photovoltaic materials is worthy. To convince the scientific community that compounds containing isoelectronic elements of O, the chalcogens S and Se, should be synthesized and, as importantly, are capable of being synthesized, three distinct subject areas will be presented. The first demonstrates that it is possible to alloy sulfur with an oxide perovskite, lead titanate (PTO), to create thermodynamically stable polar oxysulfides with band gaps in the visible spectrum. In the second, it will be shown that non-oxide non-perovskite materials can generate BPVE responses larger by an order of magnitude over the oxide perovskites listed in the literature to date. The third area does not address solar energy use directly. Instead, it alerts the scientist that creating ABS3 compounds by using temperature and time profiles used to synthesize ABO3 compounds has probably led to an incomplete characterization of these sulfides. As such, it provides first-principles based evidence that synthesis experimentation involving chalcogens does not and should not simply mirror that of pure oxide synthesis. The scientific community's knowledge of chalcogenides is far from complete, opening up exciting possibilities for new material discoveries.

Degree Type
Dissertation

Degree Name
Doctor of Philosophy (PhD)

Graduate Group
Chemistry

First Advisor
Joseph E. Subotnik

Subject Categories
Chemistry

FIRST-PRINCIPLES EXPLORATION OF THE STRUCTURAL MOTIFS OF CHALCOGENIDES AND THEIR RELATIONSHIP TO ELECTRONIC AND PHOTOVOLTAIC PROPERTIES

John A. Brehm

A DISSERTATION

in

Chemistry

Presented to the Faculties of the University of Pennsylvania in Partial Fulfillment of the Requirements for the Degree of Doctor of Philosophy

2014

Supervisor of Dissertation	Graduate Group Chairperson
Andrew M. Rappe Professor of Chemistry Professor of Materials Science and Engineering	Gary A. Molander Hirschmann-Makineni Professor of Chemistry Chair, Chemistry Department

Dissertation Committee

Joseph E. Subotnik	Associate Professor of Chemistry
Zahra Fakhraai	Assistant Professor of Chemistry
Marsha I. Lester	Edmund J. Kahn Distinguished Professor of Chemistry

To Mom and Dad:

the heart and soul

Acknowledgements

First and foremost, my deepest gratitude and thanks to Professor Andrew M. Rappe. Andrew, thanks for rescuing me. You took a chance when you did not need to, and without that chance, I would not have attained my Ph. D. Nor would I have had the opportunity to learn from you and your deep body of knowledge of mathematics, physics, and chemistry. I hope that I was able to return the favor somewhat by researching interesting new topics that expanded the realm of scientific understanding.

I thank my compatriots in the Rappe Group, Steve Young, Diomedes Saldana-Greco, Hiroyuki Takenaka, and Nathan Koocher, and my compatriots in the Subotnik Group, Brian R. Landry and Ethan Alguire, for answering all of my questions – patiently, with detail and insight, until your wisdom finally penetrated. And, for being my friends. It was fun doing research with you. You made it fun. Just one more question....

I thank Judith Currano, librarian extraordinaire of the Department of Chemistry, without whose help I could not have navigated the digital scientific record. It would have been just a vast mishmash of interfaces without your assistance.

To Cathy McDonald, Requirements Project Manager of the Department of Defense High Performance Computing Modernization Program, and Odessa Murray, S/AAA of the Office of Naval Research, thank you for granting my research group, and thus me, with the millions of computer hours I needed to run the calculations that produced the results in this thesis. To David Dumas, Senior Scientific Systems Analyst at the USACE ERDC

Scientific Computing Resource Center and Rick Roberts of the AFRL at WPAB, thank you for solving those sticky super computer problems so that my programs actually ran.

ABSTRACT

FIRST-PRINCIPLES EXPLORATION OF THE STRUCTURAL MOTIFS OF CHALCOGENIDES AND THEIR RELATIONSHIP TO ELECTRONIC AND PHOTOVOLTAIC PROPERTIES

John A. Brehm

Andrew M. Rappe

The bulk photovoltaic effect (BPVE) refers to the production of electric currents from the valence band promotion of electrons to the conduction band in a pure, undoped, and insulating material from the absorption of electromagnetic radiation. For a material to be able to create a current in response to non-polarized solar irradiation, it must be a polar compound with a band gap in the visible spectrum, 1.1 - 3.1 eV. The purpose of this work is to provide computational evidence that the pursuit of materials other than pure oxides for use as bulk photovoltaic materials is worthy. To convince the scientific community that compounds containing isoelectronic elements of O, the chalcogens S and Se, should be synthesized and, as importantly, are capable of being synthesized, three distinct subject areas will be presented. The first demonstrates that it is possible to alloy sulfur with an oxide perovskite, lead titanate (PTO), to create thermodynamically stable polar oxysulfides with band gaps in the visible spectrum. In the second, it will be shown that non-oxide non-perovskite materials can generate BPVE responses larger by an order of magnitude over the oxide perovskites listed in the literature to date. The third area does not address solar energy use directly. Instead, it alerts the scientist that creating $AB\mathrm{S}_3$ compounds by using temperature and time profiles used to synthesize $AB\mathrm{O}_3$ compounds has probably led to an incomplete characterization of these sulfides. As such, it provides first-principles based evidence that synthesis experimentation involving chalcogens does not and should not simply mirror that of pure oxide synthesis. The scientific community's knowledge of chalcogenides is far

from complete, opening up exciting possibilities for new material discoveries.

Contents

List of Tables

List of Figures

Chapter 1

Introduction

Solid state compounds form a rich tapestry of unit cell shapes that are often categorized by their building blocks. A few of the most common building blocks are termed octahedron, tetrahedron, and trigonal pyramid. These names are the result of an artificial conceptualization that connects nearest neighbor anions that all surround the same cation. For the three cases listed above, what is real, in a coordination chemistry sense, is that, respectively, six anions surround one cation, four anions surround one cation, and three anions bond to a cation in the manners depicted in Figure 1.1. These building blocks join to each other by sharing anions at corners, and, for the first two shapes, edges and faces, resulting in an increase in the variation of compounds containing them. As these motifs are very often negatively charge unbalanced, other cations are necessarily found at the interstitial sites of these motifs to create charge neutral compounds. Further increasing the variation within a set of motifs are the elements that can be chosen to fill the roles of cations and anions as certain choices can lead to distortions of the building blocks, with a building block having differing cation-anion bond lengths. While compound shape is in and of itself an interesting topic, it is in the realization that, for a given compound, different shapes lead to different electronic properties that makes it an important topic, especially given the current quest for

alternative energy creation, storage, and efficiency.

The focus of this thesis is on how to use first-principles calculations in conjunction with solid state concepts, and the solid state motifs discussed above, (especially the octahedron and trigonal pyramid motifs), to design and/or predict which compounds containing the chalcogens of sulfur and selenium will have stable phases that are useful for energy creation when impinged by solar radiation via a process termed the Bulk Photovoltaic Effect (BPVE). The field is ripe for such a discussion, as only only a couple of chalcogenides have been evaluated for the BPVE to date: in their seminal work listing the compounds that have been evaluated for the BPVE, Sturman and Fridkin list only two, ZnS and SbSI.[1] In the paragraphs below, both will be shown to have very limited usefulness for solar cell applications.

The BPVE is a phenomenon usually described as one in which a current can be produced in a pure single-phase non-centrosymmetric material with an electronic band gap when subjected to electromagnetic radiation. While the materials property that the compound have a non-centrosymmetric unit cell is necessary, the constraints of purity and single-phase are not needed in order for a material to have a BPVE, though. However, the formulations describing this phenomena, as well as separating it from other effects in current measurements, require it. Indeed, consider the silicon solar cell which is based on the physics of a pn junction using electron and hole doped adjoined layers of materials to separate photoexcited electrons from their holes via an electric field. If this material, silicon, a centrosymmetric compound, were not doped, it would not yield a current.

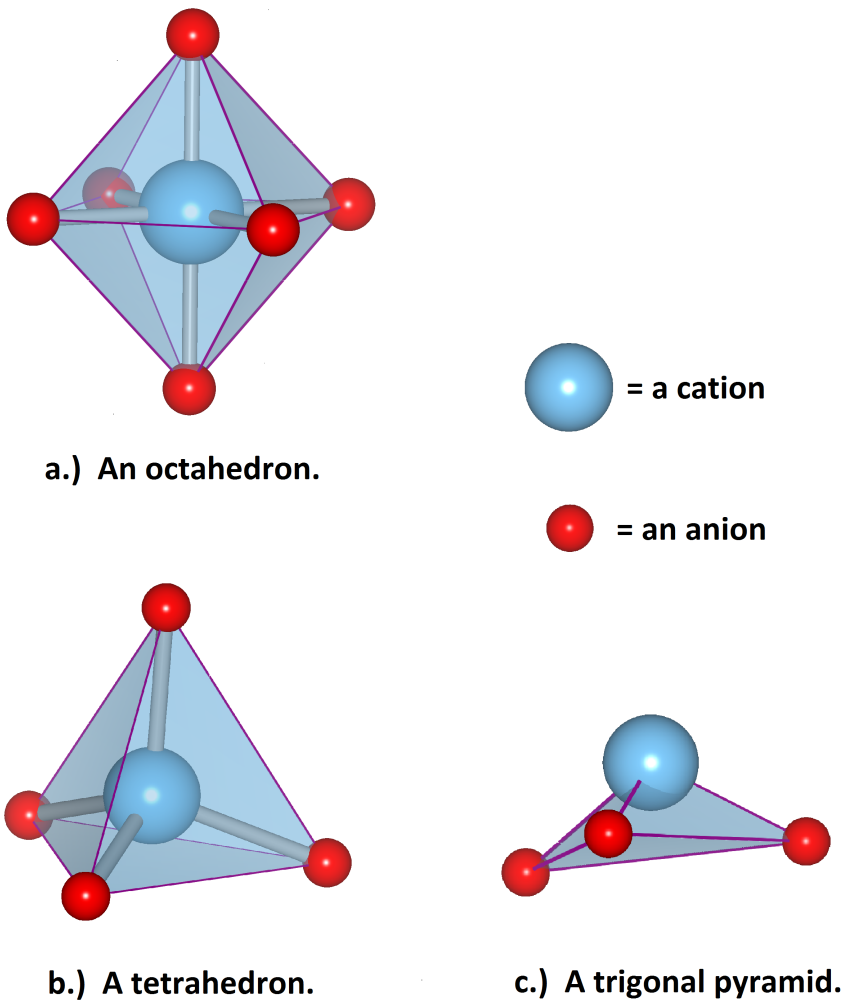

Figure 1.1: Three common solid state motifs: a.) an octahedron, b.) a tetrahedron, and c.) a trigonal pyramid. These images, and all other atomic and lattice depictions, are made with Vesta.[2]

The effect of visible light on the electrons in a system with a energy gap between filled orbitals and unfilled orbitals has been described by two time dependent perturbation theory models that are mathematically equivalent: one by Sipe and Shkrebtii,[3] and the other by Young.[4] Both models invoke the long wave length approximation for light. The long wavelength approximation for light is simply the approximation that the field the electrons experience from electro-magnetic radiation does not vary in space with respect to the lattice. Given that electro-magnetic radiation has wavelengths in the visible spectrum between 300 and 700 nanometers, which is much greater than the unit cell lattice lengths, which are in the Angstrom range, this is a most reasonable assumption. In both of their formulations, the term that arises that is quadratic in the field, which describes the interactions of photons with each other, is very small and therefore omitted.[3]

Young describes the photo-current as arising from photon-electron interactions in the following manner.[4] A first interaction with light causes an electron, originally in a ground state valence orbital, to obtain energy and become an excited electron whose wavefunction is now a combination of valence and conduction orbitals. The interaction with the oscillating photon wave also imparts an oscillating force on the excited electron, causing it to have a motion back and forth, and hence a velocity. A second interaction with a photon whose wave is 180 degrees out of phase with the initial photon leads to a net force of zero. However, for all other phases of the photon, depending on the position and velocity of the electron at the time of the second interaction, the electron has then, in general, a net velocity different from zero. But, if the lattice is centrosymmetric, $i.\ e.$ it has inversion symmetry, then the velocities of all electrons subjected to the light will lead to a net current of zero as all velocities will will cancel. Moreover, a general requirement that the crystal be non-centrosymmetric is not strong enough when one is considering materials for use in non-polarized sunlight. A non-polar piezoelectric is non-centrosymmetric, but it will only generate a BPVE photo-current when polarized light is used and said polarized light

is not parallel to any of the crystal axes.[5] However, if the lattice is non-centrosymmetric and polar, there will be always be a bias, whether or not polarized or non-polarized light is used, and, while many electron pairs will have equal magnitude and opposite direction velocities, many other pairs will not, and a net current will arise.

It is at this juncture that the physical interpretations of the two models diverge. Sipe and Shkrebtii hypothesize the real-space center of charge for the valence bands differs from that of the conduction bands, and that excited electrons promoted from the valence to the conduction band lead to a motion of charge and a shift in the center of charge.[3] They term this motion of electrons the shift vector. In their interpretation, the shift vector is confined to the maximum dimensions of the unit cell. Young, through strict mathematical formalism, though, describes the expression as one of continuous electron flux in which the shift vector can have length units several times the size of a unit cell.[4]

Indeed, in Young's interpretation, in the absence of any external circuit, negative charge will build up on one edge of a physical piece of semiconductor matter, or at the very least, on one side of a domain wall. This has been observed experimentally in bismuth ferrite, $BiFeO_3$.[6] On the other hand, a shift current localized to the unit cell, as defined by Sipe and Shkrebtii would have led to no specimen or domain wall charge build up being observed. Thus, Young's formulation of the shift current is the one used in this thesis.

The compound mentioned in the paragraph above, $BiFeO_3$, belongs to a class of compounds called perovskites. Perovskites are compounds with the general chemical formula ABX_3. They form three dimensional networks of corner sharing BX_6 octahedra with A atoms located in the space between the joined octahedra. Figure 1.2 shows one unit cell of a general non-polar perovskite. Several oxide perovskites, with X = O, have been found useful in electronic applications such as actuators, capacitors, transducers, and in general, dielectrics, as they possess unit cells with polar moments. These polar moments arise as a consequence of the A and B atoms being off-center from the oxygen octahedral cage.

Figure 1.3 shows the A and B offsets relative to a general X_6 octahedral cage. In other perovskites, atomic offsets can be combined with non-collinear octahedra into phases that are termed tilt systems. Tilted perovskites systems are realized in which the perovskite's octahedra are no longer orthogonal to each other in all three Cartesian directions, but are offset. Down a particular axis of connected octahedra, the octahedra can either rotate by the same amount in the same aspect (clockwise), or alternate in aspect by the same amount (one clockwise, one counter-clockwise, one clockwise, etc.). The first type is called an in-phase tilt; the second type is called out-of-phase tilt. A representation of a tilt system with one in-phase tilt and two out-of-phase tilts is shown in Figure 1.4. Those polar perovskites that are susceptible to changing electric field directions in such a manner that the A and B atoms move coherently, changing their directional offsets with respect to the oxygen cage in response, are termed ferroelectrics.

Due to their polarization, polar perovskites are also being evaluated as BPVE materials. If polarization was the only materials requirement, then ferroelectric perovskites would be a naturally easy choice for use in this area of solar cells. The sticking point is that many known ferroelectric perovskites have band gaps with energies in the ultraviolet range or higher, and these energies only comprises a small portion of the solar spectrum. Indeed, the visible range of the solar spectrum, from 1.1 - 3.1 eV, constitutes the strongest output of the sun's radiation.

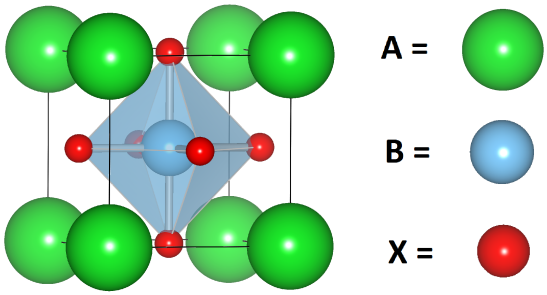

Figure 1.2: The typical ABX_3 cubic perovskite. No octahedral distortions or A or B offsets to X atoms. (Space group: $Pm\overline{3}m$.)

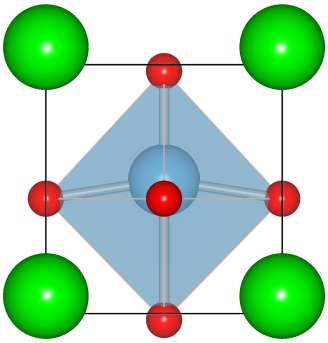

Figure 1.3: ABX_3 tetragonal perovskite. The octahedral distortion is clearly seen in the bonding in the X atoms to B, as well as the$A$- and B- atom offsets to the X-atoms. (Space group: $P4mm$.)

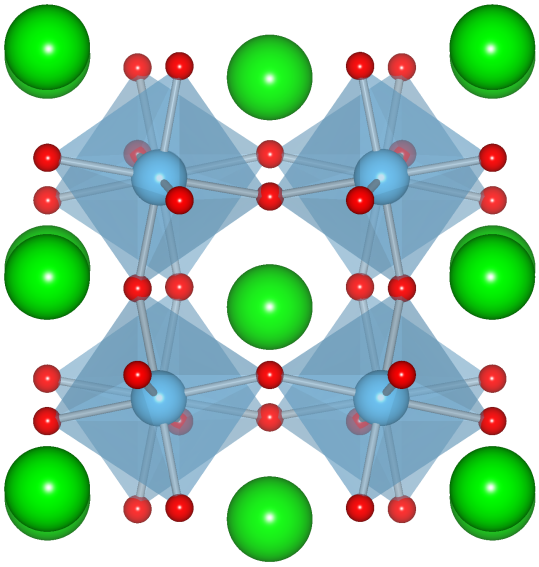

Figure 1.4: ABX_3 with corner-sharing motif and a $a^+b^-b^-$ tilt system. The view highlights the out-of-phase tilt along the b axis. (Space group: $Pnma$.)

Many popular perovskites with B = Ti, such as $PbTiO_3$, $PbZr_xTi_{1-x}O_3$, $BaTiO_3$, $SrTiO_3$ have band gaps tantalizingly just above the 3.1 eV limit of the visible range. Thusly, the materials challenge would be to find a method to lower these oxide perovskites' band gaps while maintaining polarization.

Chemists attempt to do this by changing the composition of the parent material in varying degrees, either by changing A and B sites with isoelectronic elements, or using aliovalent elements and introducing holes. This latter method has led to band gaps of 1-2 eV being calculated for $PbTiO_3$ alloyed with Ni[7] and realized experimentally for $BaTiO_3$ alloyed with Ni and $KNbO_3$.[8] Alloying the X site with aliovalent elements has proved to be difficult, though, and the choices limited. For example, replacing oxygen with fluorine would not suit the purposes sought as such a substitution would lead to an increased band gap. Replacing oxygen with nitrogen has only been accomplished up to small (less than x = 0.03) concentrations with B = Ti and only one non-La A site species, but also led to higher band gaps.[9] Other experimenters have replaced nitrogen with oxygen in non-Ti B-site compounds (ABO_2N A = Ca, Ba, Sr, B = Ta, Nb) and achieved band gaps ranging from 1.5 - 2.5 eV.[10] And in $LaTiO_2N$, band gaps in the visible range also have been observed.[11] However, in both of these cases, the compounds are found only in non-polar structures, and thus unsuitable for bulk photovoltaic purposes. Absent from the literature are results from tests involving the replacement of oxygen by sulfur for these Ti-based oxide perovskites to form $ATiO_2S$ or $ATiOS_2$. The absence of compounds of these forms is strikingly noticeable, especially when one considers that in the field of photoluminescence, the substitution of O for S in compounds is commonly used to tailor band gap reductions.[12-14] It is therefore speculated that the reason for this hole in the literature is due to the nature of sulfur itself: use of sulfur is problematic in modern materials synthesizing methods such as sputtering and molecular beam epitaxy because it contaminates the walls of the vessels it is placed in, leading to situations where no other non-sulfur containing compounds can

be created within it. Other methods of replacing O with S involve the use of poisonous or flammable gases, such as CS_2 and H_2S. Thus, in the absence of proof that such a substitution is possible and will lead to a material with desirable properties, experimentation along this line is avoided.

In Chapter 3 of this thesis, "Density Functional Theory Study Of Hypothetical $PbTiO_3$-Based Oxysulfides," provides this necessary proof. The elements of this system and the parent compound, $PbTiO_3$, were chosen for the particular reasons that titanium is a known getter of oxygen, and lead is a getter of sulfur. Indeed, the natural compound, galena (PbS), is one of the most abundant sulfide materials on earth, as compared to titanium disulfide, TiS_2, which is not. This also contrasts with BaS and SrS which are not naturally abundant. As well, BaO and SrO rank within the top twenty oxides in the lithosphere, but PbO does not.[15] Thus, it is expected that Ti will retain all O as it nearest neighbors in a $PbTiO_{3-x}S_x$ solid solution, and this expectation exceeds that of compounds ATiO$_3$ with A = Ba and Sr. It will be shown that $PbTiO_{3-x}S_x$ compounds are thermodynamically stable, retain high polarization, have PBE0 calculated band gaps between 1.77 and 2.25 eV, and have similar a and b lattice parameters that permit minimal strain layering with each other.

The BPVE has been found in the non-pyroelectric piezoelectric GaAs when this compound is subjected to polarized light.[1] However, as discussed above, the response is little more than a novelty in the solar cell world where non-polarized light from the sun provides the stimulus, leading to a netting out any BPVE effect for these compounds. One important aspect of this compound though is that its band gap is in the neighborhood of 1.1 eV, at the lower end of the visible light spectrum. This contrasts with the overwhelming majority of materials that have been evaluated for the BPVE, both experimentally and theoretically: polar perovskite oxides with band gaps larger than 3.1 eV. The only ternary compound with a band gap lower than 3.1 eV that has been tested for BPVE is $BiFeO_3$, but its response in the visible range is limited from its band gap value of 2.67 eV to the visible edge of 3.1 eV.

When one considers that the majority of visible light intensity received on the surface of earth is between 1.1 and a little over 2 eV, then even this oxide perovskite has a limited usefulness as well. As mentioned earlier, two chalcogenides, ZnS and SbSI, have been shown to have a BPVE response. However, ZnS is a non-polar piezoelectric and has a band gap above 3.5 eV making it unuseful to capture unpolarized sunlight. SbSI has a band gap of 2 eV, but is only polar below 293 K. Above 293 K, it has been classified as a paraelectric, centrosymmetric material.[1]

One proposition of this thesis, then, is that, given that non-oxide, non-perovskite polar ternary compounds with band gaps closer to 1 eV than to $BiFeO_3$'s 2.67 eV do exist, they should be evaluated for BPVE responses. Many of these compounds do not exist in the common tetragonal $P4mm$ and rhombohedral $R3c$ space groups of the perovskites, but in monoclinic and triclinic phases which are distinguishable by their lack of symmetries. Yet, they provide a richer variety of coordinations not present in perovskites locked into BO_6 octahedral sharing. For example, polar monoclinic phases of $LiAsSe_2$, $LiAsS_2$, and $NaAsSe_2$, with band gaps between 1.1 and 1.7 eV, have chains of As-Se or As-S.[16] That these band gaps are lower than perovskite oxides is not surprising. The electronegativity differences between the cation As and the anion S or Se in these three compounds is less than 1, making for less ionic interactions and smaller gaps than oxide based solids. A general periodic table trend is that for Groups 13-16, band gaps of compounds decrease as elements higher in these particular groups are substituted out for those that are lower. Indeed, no solar materials being used today are based on N, O, or F: band gaps with these elements are simply too high for solar cell purposes. Further, most perovskites have transition metal B-sites with flat conduction band structure and, thus, low mobilities of excited electrons. The conduction bands of B-sites of the non-metals or semi-metals of Groups 13-15 are highly disperse p-orbitals having much higher excited electron mobilities. In the chapter titled "First-Principles Calculation of the Bulk Photovoltaic Effect in the Polar

Compounds $LiAsS_2$, $LiAsSe_2$, and $NaAsSe_2$," the BPVE of these three compounds will be calculated. It will be shown that scientists might consider moving away from a strict oxide perovskite BPVE test space.

Even within the family of ABX_3 compounds, the difference in the nature of oxygen and sulfur is seen in the realized phases that have been synthesized with X = O as compared to X = S. The ABO$_3$ family of compounds mostly consists of perovskites (in the hundreds), and ilmenites (in the dozens), and compounds distinguished by BO$_3$ B = B, C, N, S, Cl, Br, and I polyanionic complexes bonded to A-sites (in the dozens as well). A half unit cell representation of an ABO$_3$ with a polyanionic complex, calcite, is shown in Figure 1.5 and is illustrative of these classes. The ilmenites consist of layers of alternating planes of AO$_6$ octahedra and BO$_6$ octahedra. Within a plane the octahedra are edge-connected. The planes are connected by face- and corner- sharing AO$_6$-BO$_6$ octahedra. A typical ilmenite representation is shown in Figure 1.6. Their elemental composition variations find that they have mainly small A-site cations, and both A-site and B-site cations are close in size and are transition metals. Perovskites, as described above, are not layered, and their A-sites are usually non-transition metals while their B-sites are usually transition metals. Indeed, the overwhelming majority of ABO$_3$ compounds with non-transition metals A-sites and transition metal B-sites are perovskites with a corner-connected octahedral motif. Examples of these have been shown earlier in Figures 1.2-1.4. The exceptions to these frequency observations have proved to be few. They are mostly confined to ABO$_3$ compounds with large A-sites that form in a face-sharing octahedral motif (A = Ba, Cs, and Rb), one compound with double rows of edge-sharing octahedra ($RbNbO_3$), and a couple of vanadates which form with either square-pyramidal VO_5 motifs or in a pyroxene-like manner with corner-connected tetrahedra VO_4. A representative generic ternary pyroxene is shown in Figure 1.7.

On the other hand, except for $RbBS_3$ and $TlBS_3$, ABS$_3$ do not form with polyanionic

complexes; nor are $AB\mathrm{S}_3$ ilmenite, tetrahedral, or square-pyramidal sulfide analogs known. As well, while corner-sharing and face-sharing $AB\mathrm{S}_3$ are common, so are edge-sharing $AB\mathrm{S}_3$, in contrast to the lack of edge-sharing $AB\mathrm{O}_3$. Depictions of an edge-sharing $AB\mathrm{X}_3$ and a face-sharing $AB\mathrm{X}_3$ are shown in Figures 1.8 and 1.9.

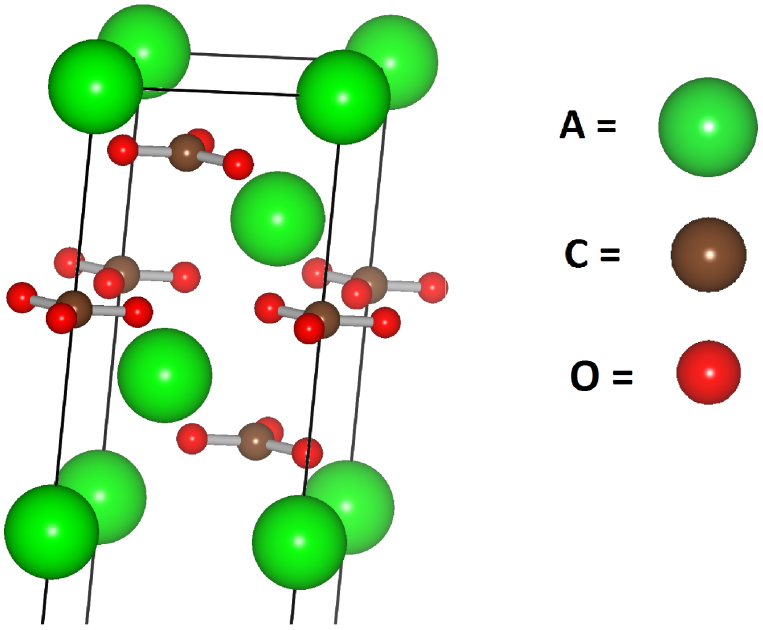

Figure 1.5: 1/2 unit cell of calcite, highlighting the $[CO_3]^{2-}$ polyanions. (Space Group: $R\bar{3}cH$.) ANO$_3$ and ASO$_3$ compounds have this same motif.

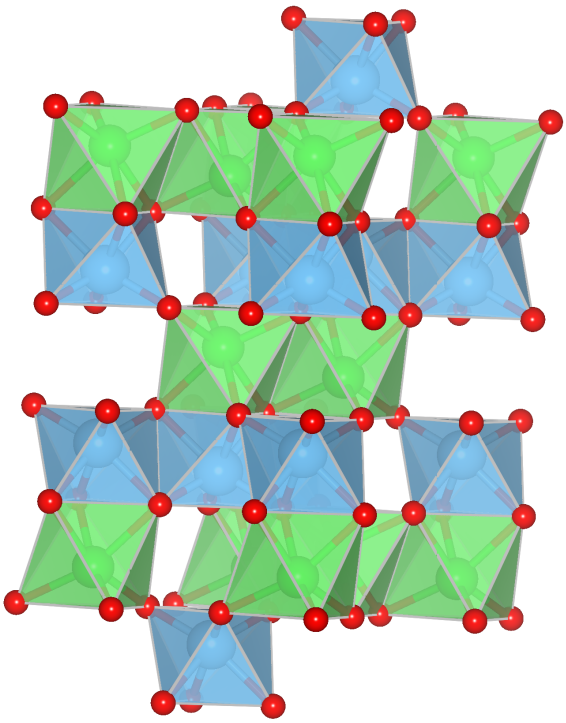

Figure 1.6: Ilmenite unit cell. Note the layered planes of $A\mathrm{O}_6$ and $B\mathrm{O}_6$ octahedra. (Space group: $R\bar{3}H$.)

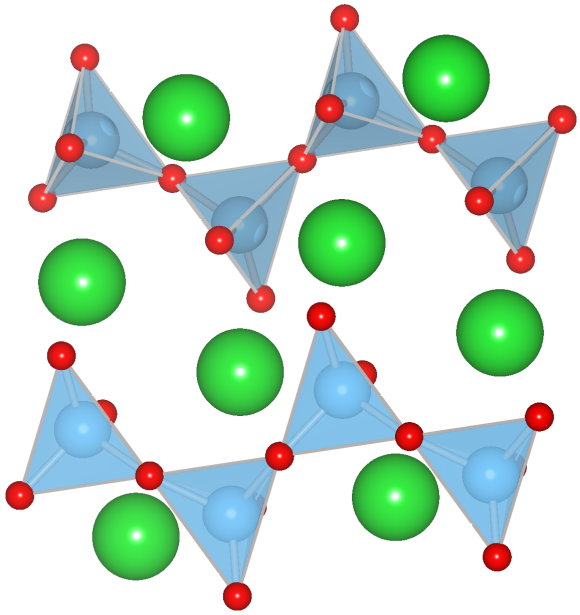

Figure 1.7: Pyroxene $AB\mathrm{O}_3$ with corner-sharing $B\mathrm{O}_4$ tetrahedra. (Space group: $Pbcm$.)

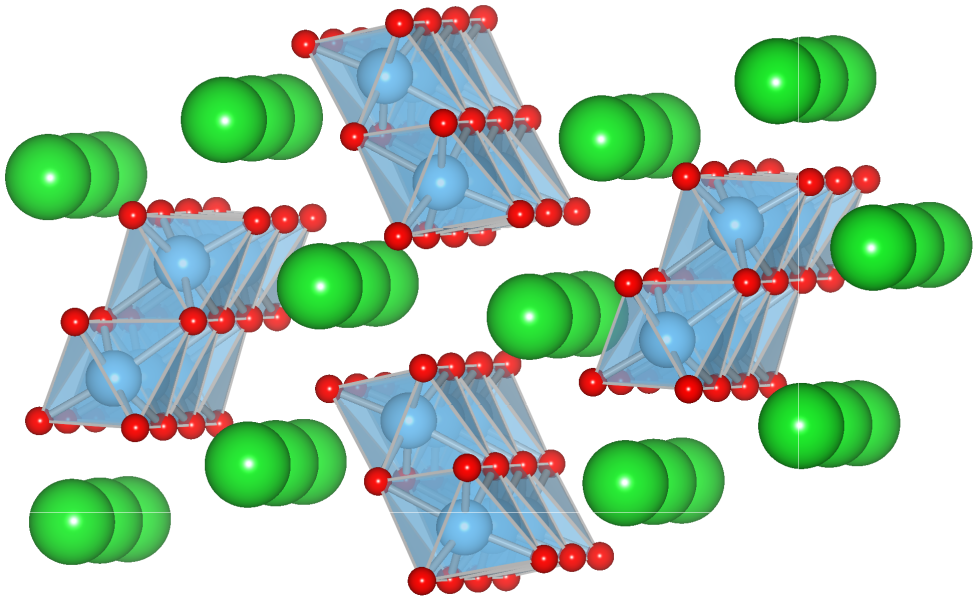

Figure 1.8: ABX_3 with edge-sharing motif. (Space group: $Pnma$.)

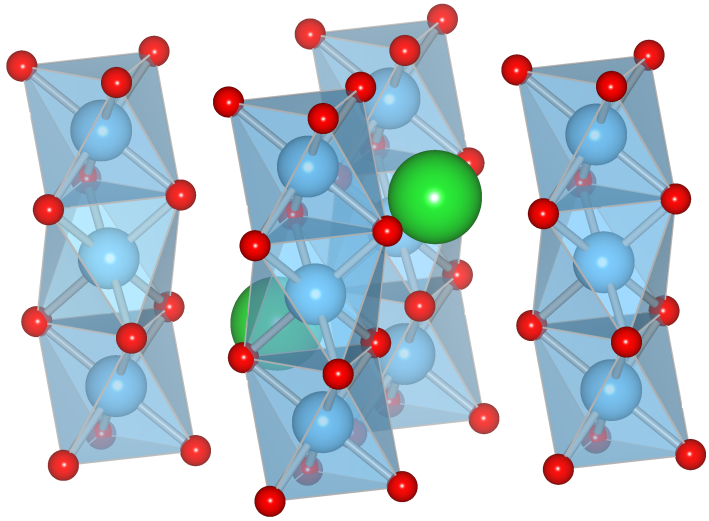

Figure 1.9: ABX_3 with face-sharing motif. (Space group: $P6_3/mmc$.)

In Chapter 5, "The Structural Diversity of ABS$_3$ Compounds with d^0 Electronic Configuration for the B-cation," this difference in realized motifs between oxide and sulfides in ABX_3 will be explored in depth. As well, a statistic used to assess $a\ priori$ the phase of ABO$_3$ compounds, the Goldschmidt tolerance factor, will be applied to ABS$_3$ compounds. The Goldschmidt tolerance factor,[17] t, is defined as

$$t = \frac{r_A + r_X}{\sqrt{2}(r_B + r_X)} \tag{1.1}$$

where the various r represent the ionic radii of the constituent species. Ranges of its values have been found to demark the groups of phases of ABO$_3$ found in nature and experiment. It will be seen though, that the application of t to the realized phases of corner-, edge-, and face-sharing ABS$_3$ compounds, leads to overlapping regions of the statistic and poor demarcation of the phases. This failure of the t factor will be addressed in the chapter as well, and a new factor will be proposed, one that encompasses both oxide and sulfide ABX_3 compounds. This new factor will align with the calculated ground states of 20 ABS$_3$ compounds. The study will demonstrate that several of the listed structures in the literature are a result of experimental conditions: of applying oxide ABO$_3$ synthesizing temperatures and times to the synthesis of sulfides.

Chapter 2

Methodology

2.1 Introduction.

Most pure solid matter are crystalline, consisting of repeatable periodic lattices defined at the Angstrom level of size. In other words, solids are defined by the patterns they adopt at the atomic level, not just those observed macroscopically, as for gemstones, quartz, or salts for example. These statements have been confirmed by countless researchers performing experiments on countless solids using the methods originally discovered by Von Laue and Bragg in the early 1910s and 1920s, called x-ray diffractometry. In these techniques, synchronous x-rays are scattered off a substance at various angles, leading to diffraction patterns consisting of nodes of various intensities, or the absence of nodes if the intensities cancel, depending on state of the superposition of the x-ray waves. These patterns, accrued over an angular range of x-rays aimed at a material, are then used to determine atomic species in a solid. As well, they are used to pinpoint atomic locations and then characterize them based on a well known set of crystalline possibilities, that have been defined by mathematical group theory, called space groups. Microscopy techniques of the late 1900s, among them transmission electron microscopy for thin layers and surfaces, and

atomic probe tomography for thicker solids, confirm the data derived from diffraction results: solids are built of repeatable atomic scale patterns of ions.

The realized periodicity of solids dovetails with the periodic constructs of electron wavefunctions of Born and von Karman and the potentials of Bloch, both theorized in the 1920s. Applying both Born-von Karman and Bloch ideas to density functional theory (DFT) allows for theoretical calculations of lattice shapes and sizes and atomic locations of solid compounds in a computationally reasonable and efficient space. Since the construct of the DFT calculation method is built on finding energy minimums from single-particle electron wavefunctions, it also can provide insights into the electronic structures of solids as well, including polarization and band gap values.

Thus, in the ensuing sections of this chapter, the major aspects of both solid state characterization from experimentation and theoretical constructs will be defined and explained. The terminology of classification of solids, (of crystal classes, point groups, symmetry operations, and space groups) will be discussed first. Then, it will be shown how DFT can be used to model real systems and predict electronic properties. As DFT calculations consider ground states of systems and are performed at 0 K, while x-ray diffraction experiments are performed at all temperatures, but most often at room temperature (300 K), a section on thermodynamics will describe how other terms, including pressure, volume, but most especially lattice vibrations arising from temperature (termed phonons), add to the energy of a solid, or for that matter, any system.

2.2 Bravais Lattices, Crystal Systems, Point Groups and Space Groups.

The following paragraphs contain information describing concepts used to construct enumerations of the various ways to describe sets of unique three-dimensional lattices. The

objective of this exercise is not to offer proofs of the number of possible lattices, but to show how this information can be used for dual purposes: to reduce the number of possible crystal structures that can be expected to have responses to fields (electric, magnetic, or mechanical) and to define which elements of a response matrix or tensor exist ($i.\ e.$ are non-zero) depending on the crystal classification of the material.

In 1848, decades before the work of van Laue and Bragg, Auguste Bravais enumerated the possible ways that units of a crystal, termed unit cells, could repeat in space and form a continuum. His method did not require knowledge of actual composition of the crystals, and thus, is a geometric construct of the periodic lattice with the specific arrangements of ions, groups of atoms, or molecules reduced to a single point. More specifically, given this construct, Bravais enumerated the number of ways a discrete set of points could be arranged and oriented such that the crystal appears exactly the same, regardless from which vantage point the crystal is viewed. He found that a set of fourteen distinct point lattices sufficiently describes the number of ways that the points of a lattice have identical environments.

These fourteen lattices can be further grouped into seven crystal systems. The seven crystal systems are the minimum representation set of point lattices that are categorized by a set of actions that can be performed on a unit cell of a crystal that leaves it unchanged visually. The set of permissible actions are called symmetry operations and each operation has an associated symmetry element. The list of symmetry elements and their associated operation is as follows:

1. center of symmetry: an operation which takes each point of the lattice at position (x, y, z) to an existing lattice position (-x, -y, -z).
2. mirror plane: an operation in which each lattice point on one side of a plane that cuts the lattice is moved to its mirror image on the other side of the plane.
3. n-fold rotation axis: a rotation through an angle of $2\pi/n$, where n is a positive integer.

4. n-fold inversion axis: a rotation through an angle of $2\pi/n$ followed by an inversion of this rotated point to an existing point.

As a whole, the seven crystal systems contain all of the possible symmetry operations or crystallographic point groups, of which there are 32. Table 2.1 lists the 32 point groups, the 14 Bravais lattices, and the seven crystal systems into which they fall. For concise depictions of Bravais lattices and point groups the reader is referred to Cullity and Stock[18] and Nye[19] respectively.

The combination of Bravais Lattices and point groups per crystal class is termed a space group. A simple multiplication of the 3rd and 4th columns of each row in Table 2.1 followed by a summation of the products lead to 61 space groups.[20] Yet, it is well known there are 230 possible space groups. The reason for such a discrepancy between the actual number of space groups and this simple method of multiplying point group symmetry operations by the number of Bravais lattices is that there are additional compound operations involving translations followed by rotations (termed screw axes) and translations followed by reflections (termed glide planes) in which the translations are fractions of a lattice vector. These operations are termed "non-symmorphic," and 157 of the 230 space groups contain these complex operations. [The summation of 61 and 157 is 218. There are an additional 12 symmorphic space groups that arise from two conditions: five from placing a trigonal point group into a hexagonal basis and seven from a few point groups that can be oriented multiple ways in a given Bravais lattice.[20]] Care must be used when evaluating non-symmorphic space groups: for example, the international naming community still labels the point group of a glide plane with the same notation it labels a simple mirror plane.

Table 2.1: Point groups and Bravais lattices, and the crystal systems into which they fall. For the Bravais lattice terminology, "Simple" refers to points only on the corners of the unit cell; $Ba - C$ (base-centered) consists of a Simple lattice and two points centered in two opposing faces; $F - C$ (face-centered) consists of a Simple lattice and a point centered on each of the six faces; and $B - C$ (body-centered) consists of a Simple lattice and a point centered in the lattice. For the point group terminology, "m" refers to a mirror plane, a number refers to n of the rotation operation, and a number with a bar above it refers to a rotation plus an inversion. (For a complete definition, including axis to which each symbol refers, please consult the International Tables for Crystallography.[21])

Crystal System	Unit Cell Lengths and Angles	Bravais Lattice	Point Groups
Cubic	$a = b = c$ $\alpha = \beta = \gamma = 90°$	Simple, $B - C$, $F - C$	23, m3, 432, $\bar{4}$3m, m3m
Tetragonal	$a = b \neq c$ $\alpha = \beta = \gamma = 90°$	Simple, $B - C$	4, $\bar{4}$, 4/m, 422, 4mm, $\bar{4}$2m, 4/mmm
Orthorhombic	$a \neq b \neq c$ $\alpha = \beta = \gamma = 90°$	Simple, $B - C$, $Ba - C$, $F - C$	222, mm2, mmm
Trigonal	$a = b = c$ $\alpha = \beta = \gamma \neq 90°$	Simple	3, $\bar{3}$, 32 3m, $\bar{3}$m
Hexagonal	$a = b \neq c$ $\alpha = \beta = 90°$; $\gamma = 120°$	Simple	6, $\bar{6}$,6/m, 622 $\bar{6}$mm, 6m2, 6/mmm
Monoclinic	$a \neq b \neq c$ $\alpha = \gamma = 90° \neq \beta$	Simple, $Ba - C$	2, m, 2/m
Triclinic	$a \neq b \neq c$ $\alpha \neq \beta \neq \gamma \neq 90°$	Simple	1, $\bar{1}$

Given a space group, there are an infinite ways of decorating the lattice with ions, groups of ions, or molecules. But there is one constraint on the placement of points: the decoration must adhere to at least one of the symmetry operations present for that particular group. The particular points of the lattice at which atoms may be placed are called Wyckoff positions. Wyckoff positions are defined as sets of points that are conjugate subgroups of the space group.

Up to this point, the information on space groups and point groups provides little more than a neat classification scheme for crystals. It is only in conjunction with Neumann's Principle, though, that the above classifications can be made useful to the chemist or physicist seeking to evaluate compounds that respond to external stimuli such as stress, electric fields, or magnetic fields. Neumann's Principle is stated as follows: "The point group of a crystal is a (not necessarily proper) subgroup of the symmetry group of any of its physical properties. It follows that the symmetry group of any property of a crystal must include the symmetry operations of the crystal point group."[21] Inversely, it also follows that the lack of a particular symmetry operation necessary for the physical property to have a non-zero crystal response must also be lacking in the crystal. For example, a crystal with a center of symmetry cannot be a piezoelectric. Further, if a crystal is to be pyroelectric, (or polar), not only must it have no center of symmetry, but it must have a unique axis that is found in no other directions of the crystal. There are ten point groups that meet the conditions for pyroelectricity: 1, 2, m, mm2, 4, 4mm, 3, 3m, 6, and 6mm. This condition is termed necessary as opposed to sufficient as, without experimentation or additional calculation, there is no way to know $a\ priori$ if the compound will produce a significant response. These ten point groups are a subset of the 21 non-centrosymmetric point groups which contain the property that they possess a necessary but not sufficient arrangement of ions or molecules to permit a piezoelectric response. The other eleven non-centrosymmetric space groups are: 222, $\overline{4}$, 422, $\overline{4}$2m, 32, $\overline{6}$, 622, $\overline{6}$m2, 23, $\overline{4}$3m, and 432. Thus, polar compounds are a

subset of piezoelectric compounds.

The manner in which a crystal responds to a stimulus such as heat, electricity, magnetism, stress, or strain can be deduced by the nature of the physical property considered subject to Neumann's Principle. Nye has tabulated many of these properties for each of the 32 point groups.[19] In this thesis, a topic of interest is the BPVE, which is a third rank tensor just like piezoelectricity, with the same non-centrosymmetric requirement. The third rank tensors can be represented in two-dimensional form due to the symmetric nature of the off-diagonal terms. For shift current responses, the matrices have the following possibilities for moduli:

$$\sigma = \begin{bmatrix} \sigma_{xxX} & \sigma_{yyX} & \sigma_{zzX} & \sigma_{yzX} & \sigma_{xzX} & \sigma_{xyX} \\ \sigma_{xxY} & \sigma_{yyY} & \sigma_{zzY} & \sigma_{yzY} & \sigma_{xzY} & \sigma_{xyY} \\ \sigma_{xxZ} & \sigma_{yyZ} & \sigma_{zzZ} & \sigma_{yzZ} & \sigma_{xzZ} & \sigma_{xyZ} \end{bmatrix} \tag{2.1}$$

where σ represents the shift current response to electromagnetic radiation, σ_{ijI} represents a modulus, with the two small letters are indices representing the incoming direction of the first and second phonons interacting with the electrons of the crystal, and the capital letter represents the direction of the induced current.

Tables 2.2, 2.3, and 2.4 depict the relationships of the moduli per point group. From such a representation it is easily seen which moduli are non-zero, and which are necessarily equal to, opposite in sign and equal to, or opposite in sign and twice the size of, one another. The difference between polar space group compounds (left columns in the tables) and ones that are non-polar piezoelectrics (the right columns in the tables) can be seen in the responses of the 21 non-centrosymmetric space groups listed in Tables 2.2-2.4. For non-polar piezoelectrics, only the off-diagonal tensor elements of the third rank tensor have non-zero moduli; while polar compounds have both non-zero diagonal and non-zero off-

diagonal moduli. Young[4] has shown that the responses generated by the off-diagonal moduli sum to zero for non-polarized light, and thus, their existence is not meaningful for generating BPVE currents with sunlight. Therefore, while non-polar piezoelectrics might serve a purpose for applications with polarized light, only polar compounds can be used to effect a current with natural sunlight.

Table 2.2: Piezoelectric moduli matrices for the triclinic, monoclinic, and orthorhombic crystal systems. All • symbols represent non-zero moduli that are not required to be equal to each other. When a symbol other than a • appears in a cell, symbols of the same type are either equal, opposite in sign, or 2 times the opposite of the symbol.[19]

Polar	**Non-polar**
Triclinic	
1	
$\begin{bmatrix} \bullet & \bullet & \bullet & \bullet & \bullet & \bullet \\ \bullet & \bullet & \bullet & \bullet & \bullet & \bullet \\ \bullet & \bullet & \bullet & \bullet & \bullet & \bullet \end{bmatrix}$	No Non-Polar Point Groups
Monoclinic	
2	
$\begin{bmatrix} 0 & 0 & 0 & \bullet & 0 & \bullet \\ \bullet & \bullet & \bullet & 0 & \bullet & 0 \\ 0 & 0 & 0 & \bullet & 0 & \bullet \end{bmatrix}$	No Non-Polar Point Groups
m	
$\begin{bmatrix} \bullet & \bullet & \bullet & 0 & \bullet & 0 \\ 0 & 0 & 0 & \bullet & 0 & \bullet \\ \bullet & \bullet & \bullet & 0 & \bullet & 0 \end{bmatrix}$	
Orthorhombic	
mm2	**222**
$\begin{bmatrix} 0 & 0 & 0 & 0 & \bullet & 0 \\ 0 & 0 & 0 & \bullet & 0 & 0 \\ \bullet & \bullet & \bullet & 0 & 0 & 0 \end{bmatrix}$	$\begin{bmatrix} 0 & 0 & 0 & \bullet & 0 & 0 \\ 0 & 0 & 0 & 0 & \bullet & 0 \\ 0 & 0 & 0 & 0 & 0 & \bullet \end{bmatrix}$

Table 2.3: Piezoelectric moduli matrices for the tetragonal and cubic crystal systems. Nomenclature as defined in Table 2.2.[19]

Polar	**Non-polar**
Tetragonal	
4	**$\bar{4}$**
$\begin{bmatrix} 0 & 0 & 0 & \circ & \star & 0 \\ 0 & 0 & 0 & \star & -\circ & 0 \\ * & * & \bullet & 0 & 0 & 0 \end{bmatrix}$	$\begin{bmatrix} 0 & 0 & 0 & \circ & \star & 0 \\ 0 & 0 & 0 & -\star & \circ & 0 \\ * & -* & 0 & 0 & 0 & \blacksquare \end{bmatrix}$
4mm	**422**
$\begin{bmatrix} 0 & 0 & 0 & 0 & * & 0 \\ 0 & 0 & 0 & * & 0 & 0 \\ \star & \star & \bullet & 0 & 0 & 0 \end{bmatrix}$	$\begin{bmatrix} 0 & 0 & 0 & * & 0 & 0 \\ 0 & 0 & 0 & 0 & -* & 0 \\ 0 & 0 & 0 & 0 & 0 & 0 \end{bmatrix}$
	$\bar{4}$2m
	$\begin{bmatrix} 0 & 0 & 0 & * & 0 & 0 \\ 0 & 0 & 0 & 0 & * & 0 \\ 0 & 0 & 0 & 0 & 0 & \bullet \end{bmatrix}$
Cubic	
	432
No Polar Point Groups.	$\begin{bmatrix} 0 & 0 & 0 & 0 & 0 & 0 \\ 0 & 0 & 0 & 0 & 0 & 0 \\ 0 & 0 & 0 & 0 & 0 & 0 \end{bmatrix}$
	$\bar{4}$3m and 23
	$\begin{bmatrix} 0 & 0 & 0 & * & 0 & 0 \\ 0 & 0 & 0 & 0 & * & 0 \\ 0 & 0 & 0 & 0 & 0 & * \end{bmatrix}$

Table 2.4: Piezoelectric moduli matrices for the trigonal and hexagonal crystal systems. Nomenclature as defined in Table 2.2.[19]

Polar	**Non-polar**
Trigonal	
3	**32**
$\begin{bmatrix} * & -* & 0 & \star & \blacksquare & -2\circ \\ -\circ & \circ & 0 & \blacksquare & -\star & -2* \\ \dagger & \dagger & \bullet & 0 & 0 & 0 \end{bmatrix}$	$\begin{bmatrix} * & -* & 0 & \star & 0 & 0 \\ 0 & 0 & 0 & 0 & -\star & -2* \\ 0 & 0 & 0 & 0 & 0 & 0 \end{bmatrix}$
3m	
$\begin{bmatrix} 0 & 0 & 0 & 0 & \blacksquare & -2\circ \\ -\circ & \circ & 0 & \blacksquare & 0 & 0 \\ \dagger & \dagger & \bullet & 0 & 0 & 0 \end{bmatrix}$	
Hexagonal	
6	$\bar{\mathbf{6}}$
$\begin{bmatrix} 0 & 0 & 0 & \star & * & 0 \\ 0 & 0 & 0 & * & -\star & 0 \\ \dagger & \dagger & \bullet & 0 & 0 & 0 \end{bmatrix}$	$\begin{bmatrix} * & -* & 0 & 0 & 0 & -2\circ \\ -\circ & \circ & 0 & 0 & 0 & -2* \\ 0 & 0 & 0 & 0 & 0 & 0 \end{bmatrix}$
6mm	$\bar{\mathbf{6}}$**m2**
$\begin{bmatrix} 0 & 0 & 0 & 0 & * & 0 \\ 0 & 0 & 0 & * & 0 & 0 \\ \dagger & \dagger & \bullet & 0 & 0 & 0 \end{bmatrix}$	$\begin{bmatrix} 0 & 0 & 0 & 0 & 0 & -2\circ \\ -\circ & \circ & 0 & 0 & 0 & 0 \\ 0 & 0 & 0 & 0 & 0 & 0 \end{bmatrix}$
	622
	$\begin{bmatrix} 0 & 0 & 0 & \star & 0 & 0 \\ 0 & 0 & 0 & 0 & -\star & 0 \\ 0 & 0 & 0 & 0 & 0 & 0 \end{bmatrix}$

2.3 A Computationally Accurate and Efficient Theoretical Framework for the Energy Assessment of Matter.

The previous section discussed the nomenclature for defining the number of ways compounds that are crystalline can be arranged. While many compounds exist in only one form, and others in just a few forms, there are a few compounds like titanium oxide with its eleven polymorphs, that can be found in multiple forms. The challenge then, for a theorist, is to assess the various forms a compound can reasonably be expected to exist in, and determine which of these forms is preferred energetically at various temperatures and pressures. The remaining sections of this chapter will evaluate the framework that has been developed to perform this task.

2.3.1 Density Functional Theory.

In their essence, all compounds at the chemical level of bonding consist of interacting systems of nuclei and electrons. Each can be described by the hamiltonian:[22]

$$\hat{H} = -\frac{\hbar^2}{2m}\sum_{i}^{N}\nabla_i^2 + \sum_{i,I}^{N,K}\frac{Z_I e^2}{|\mathbf{r}_i - \mathbf{R}_I|} + \frac{1}{2}\sum_{i\neq j}^{N}\frac{e^2}{|\mathbf{r}_i - \mathbf{r}_j|} - \sum_{I}^{K}\frac{\hbar}{2M_I}\nabla_I^2 + \frac{1}{2}\sum_{I\neq J}^{K}\frac{Z_I Z_J e^2}{|\mathbf{R}_I - \mathbf{R}_J|} \tag{2.2}$$

where N is the number of electrons, K is the number of nuclei, the lower case subscripts indicate electrons and upper case subscripts nuclei, m and M denote the mass of an electron and a nucleus, **r** and **R** denote electron and nuclei positions, and Z denotes the charge of a nucleus.

The first and fourth terms represent the kinetic energies of the electrons and the nuclei respectively. The second term represents the potential between the electrons and the nuclei.

The third term accounts for electron - electron interactions. The fifth term represents the interaction of nuclei with each other.

This hamiltonian, consisting of kinetic and potential energies, maps directly into the time-independent Schrodinger equation

$$\hat{H}\Psi(\mathbf{r_1}, \mathbf{r_2}, ..., \mathbf{r_N}, \mathbf{R_1}, \mathbf{R_2}, ..., \mathbf{R_K}) = E\Psi(\mathbf{r_1}, \mathbf{r_2}, ..., \mathbf{r_N}, \mathbf{R_1}, \mathbf{R_2}, ..., \mathbf{R_K}) \tag{2.3}$$

where $\Psi(\mathbf{r_1}, \mathbf{r_2}, ..., \mathbf{r_N}, \mathbf{R_1}, \mathbf{R_2}, ..., \mathbf{R_K})$ represents the total wavefunction.

Solving this problem for the eigenvalue energies and wavefunctions of a multi-body system of interacting particles is near impossible in its current form except for a simple hydrogen atom, which is a two-body problem. Fortunately, simplifications grounded in physics have been devised, including the Born-Oppenheimer approximation, the Hohenberg-Kohn theorems, the Kohn-Sham ansatz, plane wave representations, and the pseudopotential method, that make the problem tractable. Each are discussed, briefly, in turn.

2.3.2 The Born-Oppenheimer Approximation

Since the M_I are much more massive than m, the velocities of the nuclei relative to electrons are much smaller. As such, after a change from one ionic configuration to another, (in the neighborhood of the the ground state of the system, which is known as the adiabatic condition), the electrons have already adjusted nearly instantaneously, and will remain in their ground state. In essence, the nuclei and electron motions have been decoupled. This decoupling is known as the Born-Oppenheimer approximation.[23] This approximation implies that the total hamiltonian of the system as represented in equation (2.2) can be separated along electronic and nucleonic terms, and that $\Psi(\mathbf{r}, \mathbf{R})$ can be approximated as $\chi(\mathbf{R_1}, \mathbf{R_2}, ..., \mathbf{R_K})\ \phi(\mathbf{r_1}, \mathbf{r_2}, ..., \mathbf{r_N}; \mathbf{R_1}, \mathbf{R_2}, ..., \mathbf{R_K})$ in which the wavefunction of the electrons $\phi(\mathbf{r}; \mathbf{R})$ depends only on the positions of the nuclei and the wavefunction of the nuclei

$\chi(\mathbf{R_1}, \mathbf{R_2}, ..., \mathbf{R_K})$ is independent of the electrons. Thus, the electronic hamiltonian of the system is the first three terms of (2.2):

$$\hat{H}_{el} = -\frac{\hbar^2}{2m}\sum_i \nabla_i^2 + \sum_{i,I}\frac{Z_I e^2}{|\mathbf{r}_i - \mathbf{R}_I|} + \frac{1}{2}\sum_{i\neq j}\frac{e^2}{|\mathbf{r}_i - \mathbf{r}_j|} \tag{2.4}$$

The last two terms of (2.2) involve only nucleonic species not dependent on electronic contributions. They are treated in a classical sense, and require no further simplifications to compute efficiently. This is not to say that nuclear motions are unimportant. But they can be treated from a static viewpoint of charged points when calculating kinetic and Coulombic energies in neighborhoods of perturbed nuclear positions.

Before proceeding, the notation for each of the terms in (2.4) is identified and condensed for readability. The first term in (2.4) is the kinetic energy operator $\hat{T}$, the second term is the external potential $\hat{V}$, and termed "external" as the potential is not generated self-consistently by electron interactions, but involves nuclei "external" to the all-electron system, and the third term is the Coulombic interaction $\hat{U}$:

$$\hat{T} = -\frac{\hbar^2}{2m}\sum_i \nabla_i^2 \tag{2.5}$$

$$\hat{V} = \sum_{i,I}\frac{Z_I e^2}{|\mathbf{r}_i - \mathbf{R}_I|} \tag{2.6}$$

$$\hat{U} = \frac{1}{2}\sum_{i\neq j}\frac{e^2}{|\mathbf{r}_i - \mathbf{r}_j|} \tag{2.7}$$

2.3.3 Hohenberg-Kohn and Kohn-Sham.

Hohenberg and Kohn proved that for any system of interacting particles, $\hat{V}$ can be determined by the ground state density $n_0[\mathbf{r}]$ of the system.[24] As well, they showed that an

energy functional $E[n]$ in terms of the density $n_0[\mathbf{r}]$ could be minimized to determine the ground state energy of the system, and the corresponding density would be the ground state density $n_0[\mathbf{r}]$. Thus, ignoring the classical terms involving only nuclei, the energy of the system can be re-written in terms of a functional of the density:

$$E[n] = T[n] + U[n] + V[n] \tag{2.8}$$

The Hohenberg-Kohn Theorems state that simply knowing the density implies complete knowledge of the total wavefunction as well as complete knowledge of all other observables, including external potentials.

In and of itself, Hohenberg-Kohn still represents a many-body problem with no suggestion on how to determine the functionals in (2.5) - (2.7). Later work by Kohn, in conjunction with Sham, provide a tractable method.[25] They claim, through an ansatz, that there exists a density based on a non-interacting system of electrons that is equal to the ground state density of the original interacting system. In effect, they claim that $T[n]$ can be separated into sums of single-particle non-interacting electron terms and those that involve correlation of electrons. The single-particle kinetic energy term is the summation of the individual electron kinetic energies, $T_s[n]$. As well, the Coulombic-interaction term can be represented as the sum of the well-known Hartree energy, U_H, and correlation interactions. Thus, the energy functional becomes:

$$E[n] = T_s[n] + U_H[n] + E_{xc}[n] + V[n] \tag{2.9}$$

where $E_{xc}[n]$, known as the exchange-correlation energy, contains the differences $T[n]$ - $T_s[n]$ and $U[n]$ - $U_H[n]$, as well as accounting for the fermion nature of electrons, in which

electrons of the same spin are kept apart by a repulsive interaction. Though $E_{xc}[n]$ is not known with certainty, it is typically smaller in magnitude than $T_s[n]$, $U_H[n]$, and $V[n]$.[26] Approximations of this quantity will be discussed in the next subsection.

Minimizing $E[n]$ in (2.9) with respect to the density functional leads to the following:[26]

$$\begin{aligned}\frac{\partial E[n]}{\partial n[\mathbf{r}]} = 0 &= \frac{\partial T_s[n]}{\partial n[\mathbf{r}]} + \frac{\partial U_H[n]}{\partial n[\mathbf{r}]} + \frac{\partial E_{xc}[n]}{\partial n[\mathbf{r}]} + \frac{\partial V[n]}{\partial n[\mathbf{r}]} \\ &= \frac{\partial T_s[n]}{\partial n[\mathbf{r}]} + v_H(\mathbf{r}) + v_{xc}(\mathbf{r}) + v(\mathbf{r}) \end{aligned} \tag{2.10}$$

If the system is one of non-interacting particles, with a potential $v_s(\mathbf{r})$ and corresponding density $n_s(\mathbf{r})$, this equation becomes:

$$\frac{\partial E[n]}{\partial n[\mathbf{r}]} = 0 = \frac{\partial T_s[n]}{\partial n_s[\mathbf{r}]} + v_s(\mathbf{r}) \tag{2.11}$$

as, in the absence of interactions, the U_H and E_{xc} terms are 0. If the Kohn-Sham ansatz is to hold, then $n_s(\mathbf{r})$ = $n(\mathbf{r})$ and:

$$v_s(\mathbf{r}) = v_H(\mathbf{r}) + v_{xc}(\mathbf{r}) + v(\mathbf{r}) \tag{2.12}$$

This is the main result of the Kohn-Sham ansatz: a noninteracting-body potential can be used to solve an interacting-body density, from which interacting wavefunctions are also determined. The actual calculation used to make these determinations is iterative, with an initial guess of the density field. From this field, the potential $v_s(\mathbf{r})$ is calculated. Then, the Schrodinger equation of the non-interacting system,

$$\Big[-\frac{\hbar^2}{2m}\nabla_i^2 + v_s(\mathbf{r})\Big]\phi_N(\mathbf{r}) = \epsilon_N\phi_N(\mathbf{r}), \tag{2.13}$$

is solved. The resulting wavefunctions, given the occupations of their respective orbitals, f_i, are then used to compute $n(\mathbf{r})$:

$$n(\mathbf{r}) = n_s(\mathbf{r}) = \sum_i^N f_i|\phi_N(\mathbf{r})|^2 \tag{2.14}$$

If the original guess of the density and the calculated density are within a determined limit, the calculation is complete, and all the information concerning total energy, eigenenergies, eigenfunctions, and auxiliary calculations are now computed. If not, then the process repeats, with the new calculated density serving as the input to calculate another potential.

2.3.4 Exchange-Correlation Energy Functionals.

The two most widely known methods for approximating E_{xc} are the Local Density Approximation (LDA) and the family of Generalized Gradient Approximations (GGA). In LDA, the system is considered to have a uniform exchange-correlation energy per volume. This energy per volume is a combination of exchange energy, $e_x(n)$, which is known exactly to scale as $n^{4/3}$ in a homogeneous electron gas, and correlation energy, $e_c(n)$, determined from Quantum Monte Carlo methods. It has been found that LDA usually underestimates E_c by the same amount it overestimates E_x, (due to the exchange-correlation hole sum rule), leading to solutions of the Kohn-Sham equations that are reasonable.[26] In the case of GGA, the uniform electron gas restriction of LDA is removed, and a spatially varying function of density is adopted. This leads to energies at any any point in space being a

function of the density and the gradient of the density. Many such constructs have been developed including ones by Perdew, Burke, and Ernzerhof, Wu and Cohen, and Cooper.[27]

Energy equations for LDA and GGA respectively are:

$$E_{xc}^{LDA} = \int d^3\mathbf{r} e_{xc}^{homo}(n(\mathbf{r})) \tag{2.15}$$

$$E_{xc}^{GGA} = \int d^3\mathbf{r} e(n(\mathbf{r}), \nabla n(\mathbf{r})) \tag{2.16}$$

At this juncture, an unsolvable, multi-body problem has been made solvable by a decoupling of electron and nuclei motion (the Born-Oppenheimer Approximation), the adoption of a single-body approach (Kohn-Sham Ansatz) which uses the density observable not only as a substitute for, but as a determinant of, the ground state wavefunctions (Hohenberg-Kohn Theorems), and with the many-body exchange-correlation term as the only term not completely known with certainty, but well defined through LDA and GGA functional approximations in most cases. Yet, there are still two areas in which the calculation can be made more efficient. The first is in the judicious decision on how to express wavefunctions in a basis set. The second is in the use of the chemical knowledge that only valence electrons are involved in creating chemical bonds. These two areas will be discussed in the subsections below.

2.3.5 Plane Waves.

In crystalline systems, the lattice consists of continuous repeatable unit cells. As such, the potential in a crystal is periodic. By Bloch's theorem, a wavefunction can be represented as the product of a cell-periodic function and a phase factor:[28]

$$\psi_{n\mathbf{k}}(\mathbf{r}) = u_{n\mathbf{k}}(\mathbf{r})e^{i\mathbf{k}\cdot\mathbf{r}} \qquad \text{where } u_{n\mathbf{k}}(\mathbf{r}+\mathbf{R}) = u_{n\mathbf{k}}(\mathbf{r}) \tag{2.17}$$

where $\mathbf{r}$ represents any position in the lattice, $\mathbf{R}$ is any Bravais lattice vector, n is an occupied energy band, and $\mathbf{k}$ is a wave vector.

The cell-periodic function can be represented as set of plane waves defined in reciprocal space:

$$u_{n\mathbf{k}}(\mathbf{r}) = \sum_{\mathbf{G}} c_{n\mathbf{k}}(\mathbf{G}) e^{i\mathbf{G}\cdot\mathbf{r}} \tag{2.18}$$

where $\mathbf{G}$ is a reciprocal lattice vector. Substituting (2.18) into (2.17) the electron wavefunction becomes:

$$\psi_{n\mathbf{k}}(\mathbf{r}) = \sum_{\mathbf{G}} c_{n\mathbf{k}}(\mathbf{G}) e^{i(\mathbf{k}+\mathbf{G})\cdot\mathbf{r}} \tag{2.19}$$

Representation of the wavefunctions in this manner improves the speed of calculation in a couple of ways. First, the form permits Fast Fourier Transforms (FFT). Second, as kinetic energy is directly proportional to $|\mathbf{k}+\mathbf{G}|^2$, the size of the calculation can be limited to a maximum $\mathbf{k}$ by placing a maximum value permissible on kinetic energy, termed E_{cut}. As well, grid steps sizes can be altered for better efficiencies. However, while lower rather than higher values of E_{cut} and grid densities are preferred for computational speed, both should be increased until convergence of results between successive iterations of both variables is achieved.

2.3.6 Pseudopotentials.

Many solid state systems consist of unit cells in which there are hundreds of electrons, each of which has a wavefunction and each of which contribute to $T[n]$, $U[n]$, $V[n]$, and $E_{xc}[n]$.

The size of this problem can be greatly reduced, however, by considering the chemical fact that, in almost all cases, it is only the valence electrons of each atom that participate in bonding. The core electrons can be considered tightly bound to the nucleus of an atom, and the nucleus plus the core electrons can be modeled as an ion with an ionic potential replacing a nucleonic potential, reducing the number of nuclei-electron Coulombic interactions, to interactions of ions and valence electrons. Furthermore, instead of all electrons of a unit cell interacting with one another, the core electrons have been completely localized to their respective nuclei, and now only valence electron - valence electron interactions need to be considered. The size of the computation is further reduced by modeling the wavefunction of the valence electrons such that their radial nodes are removed, thereby generating a smooth wavefunction constructed from fewer plane waves with smaller kinetic energies. The construct that embodies this weaker potential is called the pseudopotential.

Pseudopotential generation methods are not unique and are subject to different construction constraints. In the work of this thesis, norm-conserving pseudopotentials are used. With r_c defined as the core radius of an electron from the nucleus, norm-conserving pseudopotentials are designed with the following properties for each valence electron:

1. For the reference configuration, the eigenvalue energies of the pseudo-wavefunction and the all-electron wavefunction from which it is derived are equal.
2. The integrated charge density generated by the pseudo wavefunction is equal to that of the all-electron wavefunction from r = 0 to r = r_c.
3. The pseudo wavefunction and the all-electron wavefunction, and their first and second derivatives with respect to r, in the region $r >= r_c$ are exactly equal.
4. The first derivatives with respect to energy of the first derivatives with respect to r of the pseudo wavefunction and the all-electron wavefunction must be equal as well for all $r > r_c$. [29, 30]

The legitimacy of a pseudopotential can be judged in two ways: by comparing the results of a DFT calculation using it to the results of a DFT calculation using all-electron wavefunctions, or by comparing the results ($e.\ g.$ lattice parameters) to known experimental values.

2.4 Using Post-DFT Methods to Calculate Electronic Properties of Crystals

2.4.1 Band Gap Methods.

It is widely known that DFT methods can underestimate band gaps of known materials, or, even worse, calculate that a material is metallic when it is a semiconductor.[22, 31] The source of this error lies in the formulation of the exchange-correlation term, E_{xc}[n]. The first derivative of this term, the exchange-correlation potential, $v_{xc}[\mathbf{r}]$, can be expressed as:

$$v_{xc}[\mathbf{r}] = e_{xc}([n], \mathbf{r}) + n(\mathbf{r})\frac{\partial e_{xc}([n], \mathbf{r})}{\partial n[\mathbf{r}]} \tag{2.20}$$

where e_{xc}([n],**r**) is the energy per electron at r that depends only on the $n[\mathbf{r}]$. The derivative in the second term signifies a change in the exchange-correlation hole with density. This expression is discontinuous at the Fermi level. Both LDA and GGA – indeed even Kohn-Sham theory with an exact expression for E_{xc} – predict that this derivative is 0.[26] But it is not.[26] Hence, the error in band gap prediction using these approximations in particular, and the method in general.

Post-DFT methods have been devised to improve band gap results and predictions. Three of these methods, LDA+U, PBE0, and GW, have been used to correct for LDA band

gap underestimation. These methods will be discussed in the paragraphs below. They are termed "post"-DFT as each uses the wavefunctions and eigenvalue energies generated by DFT calculations as initial starting parameters for their respective iterative methods.

The LDA+*U* Method.

LDA+U has been developed as a method to take into account that d and f electron orbitals are localized and, thus, on-site Coulombic interactions are screened. It represents an energy correction to that determined solely by LDA:[32]

$$E_{LDA+U}[n] = E_{LDA}[n] + E_{HubU}[n_m^I] - E_{DC}[n^I] \tag{2.21}$$

where n_m^I are the atomic orbital occupations experiencing the Hubbard effect, and the last term removes double counting of Coulombic interactions contained in both the first two terms.

This equation can be expanded in terms of U:[32]

$$E_{LDA+U}[n] = E_{LDA}[n] + \frac{U}{2}\sum_{i\neq j} n_i n_j - \frac{U}{2}\sum_i n_i(n_i - 1) \tag{2.22}$$

where U is called the Hubbard U term and represents the radial Slater integral value of F^0.

The orbital energies are the derivatives of $E_{LDA+U}[n]$ with respect to orbital occupations n_i:

$$e_i = \frac{\partial E_{LDA+U}[n]}{\partial n_i} = e_{LDA} + U\Big(\frac{1}{2} - n_i\Big) \tag{2.23}$$

The orbital dependent potential is represented similarly, but as an operation involving the derivative of E_{LDA} with respect to $n_i[\mathbf{r}]$:

$$V_i[\mathbf{r}] = V_{LDA}[\mathbf{r}] + U\Big(\frac{1}{2} - n_i\Big) \tag{2.24}$$

These formulae show LDA orbital energies and the orbital dependent energies being shifted by -U/2 for occupied orbitals (n_i = 1) and by +U/2 for unoccupied orbitals (n_i = 0). Thus the additional energy separation achieved by this method is equal to U, which corresponds to the U described for Mott-Hubbard insulators.

There are generally two ways to determine an U value for a substance. The first involves known substances. In this scenario, various U values are substituted in the framework described above and the U value chosen is the one for which the calculated band gap most closely matches the experimental one. As this method cannot be appropriate for theoretical substances or real substances whose band gaps have not been ascertained, another method for determining U has proposed in the literature. This method assesses how the total energy changes with respect to a variation of electrons in the localized orbits. This variation of electrons does not involve an integral number increase or decrease, but a fractional value change. U is defined as a response to the partial injection or partial removal of an electron to/from a site in which an electron has been localized due to the application of an external potential:[32]

$$U = (\chi_0^{-1} - \chi^{-1})_{ii}, \quad \text{where} \quad \chi_{ij} = \frac{\partial n_i}{\partial v_j} \tag{2.25}$$

Here, χ represents an interacting response, χ_0 represents the Kohn-Sham non-interacting response, n_i represents the occupation number of the localized levels associated to site i, and v_j is the potential shift applied on the localized orbit at site j. Fractional occupations are

reasonable in solids where hybridization of localized orbitals is probable, and this method has been show to be useful for solids in which the nominal electronic configuration of the atomic species to which one is considering placing a U value on is not d^0, d^{10}, f^0, or f^{14}. For d^0 and f^0, removal of partial electrons is not reasonable; and for d^{10} and f^{14}, addition of partial electrons is not reasonable. Indeed, in work performed by Gou $et\ al.$[33] on the compound $PbTiO_3$, this method has led to a U_{Ti} = 4.75 eV, and a band gap of 2.17 eV; a result which still severly understimates the experimental band gap of 3.4-3.6 eV.

The PBE0 Method: Accounting for Exact Exchange.

PBE0 is the name of the Perdew-Burke-Ernzerhof GGA functional that allows for the inclusion of exact exchange energies. Perdew, Burke and Ernzerhof[34] based their functional on the work of Becke. Becke proposed that the reason for the poor band gap estimations lies in the strict adherence to the Born-Oppenheimer approximation for the exchange-correlation energy. He sought to rectify this by creating a term which relies on partially interacting systems of electrons:[35]

$$E_{xc} = \int_0^1 U_{xc}^{\lambda} d\lambda \tag{2.26}$$

in which λ is the interelectronic coupling strength parameter (the $1/r_{12}$ Coulomb repulsion term), and U_{xc}^{λ} is the potential energy of the exchange correlation defined at different coupling strengths. A $\lambda = 0$ indicates the completely non-interactive Kohn-Sham condition and a value of 1 indicates a completely interacting system. Becke develops a semi-empirical model defined as:

$$E_{xc} = E_{xc}^{LDA} + a_0(E_x - E_x^{LDA}) + a_x(E_x^{GGA} - E_x^{LDA}) + a_c(E_c^{GGA} - E_c^{LDA}) \quad (2.27)$$

where a_0, a_x, and a_c are determined by fitting the model to experimental data.

In the PBE0 model, this equation becomes:

$$E_{xc} = E_{xc}^{GGA} + a_0(E_x - E_x^{GGA}) \quad (2.28)$$

with a_x = 1 - a_0, a_c = 1, and E_{xc} = E_x + E_c. Perdew, Burke and Ernzerhof suggest at first that a_0 = 1/n, with n being an integer representing the lowest order of perturbation theory that satisfactorily describes the shape of the λ dependence of the exact $E_{xc,\lambda}$:[34]

$$E_{xc} = E_{xc}^{GGA} + (E_x - E_x^{GGA})(1 - \lambda)^{n-1} \quad (2.29)$$

They find that n = 4 provides calculated results that match experimental values of small molecules (up to six atoms), n = 1 describes closed-shell ions, and n >= 4 is useful for chemical conditions such as O_3, where there are degenerate or nearly-degenerate ground states.[34] However, perhaps realizing that their methodology only leads to less than satisfactory results for other solids, they then relax the requirement that n must be an integer and permit it to be any value greater than 1. This leads to continuous values of a_0, but as they note, is a speculative construct.[34] Thus, a_0 becomes an arbitrary value. Unlike the arbitrary application of U for known substances, a single value of a_0 should be applicable to those types of compounds that maintain similar spatial and chemical environments, as Perdew, Burke and Ernzerhof showed for simple molecules or as should be expected for

iso-electronic structures in the same phase space, with phase defined as atoms located at the same Wyckoff positions of the same space group.

The GW Method.

The GW method is a many-body perturbation approach to solving valence and conduction eigenvalue energies that seeks to improve on the Kohn-Sham single-body non-interacting approach which is only valid for valence energies. The term "GW" stands for the combination of techniques its founder, Hedin, used in 1965 to overcome K-S limitations: the "GW" is the product of the "G", a Green's function that describes quasi-particle (in this case electrons) energies, and the screened Coulomb interaction, W.[36] The Green's function describes the probability over time that a hole or electron will propagate to a different energy level. The many-body energy equation contains the same type and number of terms as the K-S equation, but, importantly, the wavefunctions now embody many-body interactions, and the K-S exchange-correlation energy is now termed a self-energy term defined by the GW product – it is still similar in purpose to E_{xc}^{KS}, but now affected by multiple exchange-correlation energies of the system. In its formalism, this self energy is non-local, non-Hermitian, and energy dependent with quasi-particle wavefunctions that are not orthogonal. Further, it leads to quasi-particle energies that have imaginary components.[31]

In order to overcome this imaginary aspect of GW, certain approximation schemes have been developed. The approximation used in this thesis is the self-consistent GW method, $sc-GW$. In $sc-GW$, the complete dynamical matrix is constrained such that it becomes static and Hermitian. The calculation proceeds from the LDA eigenvector wavefunctions as opposed to the many more numerous wavefunctions from the pseudopotentials for all of the electrons of each atom of the system, and iterates to a self-consistent solution of many-body wavefunctions and energies.[37]

2.4.2 Phonons.

Quantized lattice vibrations, due to temperature, are called phonons. Phonon frequencies are an easily attainable DFT matrix quantity. The $3N$ matrix of frequencies, where N represents the number of atoms in the system, are simply the second derivative of the total energy with respect to small perturbations of each nuclei in the unit cell, at any point in the Brillouin zone. There are higher terms present in the perturbation, but these are ignored so that harmonic formulations and approximations can be made. Though simply attained, phonons have a two-fold importance.

First, though the Kohn-Sham calculation leads to an energy minimum in terms of nuclei locations, it is important to assess whether this energy minimum represents, in the least, a metastable state, or if, in fact, other configurations similar to the one found are more stable. If the K-S calculated state produces a phonon frequency matrix in which the second derivatives with respect to the perturbations are all positive, then that state is stable in the neighborhood of the nuclei locations. However, if a second derivative of energy with respect to the perturbation is negative, then there exists a more stable configuration somewhere in that neighborhood.

If the frequency matrix elements are all positive, (and hence the structure is stable), then a second reason to define phonon frequencies is to determine the energy contribution of lattice vibrations, because a DFT calculation alone only determines the enthalpy of the lattice at 0 K. Consider Figure 1.4 and Figures 1.7-1.9. The four structures depicted are common motives of ABX_3 compounds. Figure 1.7 is arranged in a manner agreeing with the $Pbcm$ space group and has a structural motif of single chains of corner-connected BX_4 tetrahedra. The image in Figure 1.9 belongs to $P6_3/mmc$ space group and has face-sharing BX_6 octahedra. The arrangement of atoms in Figures 1.4 and 1.8 are of structures in the $Pnma$ space group, yet they are greatly different: the one in Figure 1.8 has a structural motif of double rows of edge-connected BX_6 octahedra, while the arrangement in Figure

1.4 has corner-connected BX_6 ocathedra. The different phase motifs stem from the different allowed Wyckoff arrangements of the atoms, and highlights the non-uniqueness of compounds in terms of space group assignment. A DFT calculation of each is only a partial assessment of the compound's energy in each configuration. Without calculating the zero point of energy and the phonon contribution to energy at T $>$ 0 K, the energy assessment of each phase is incomplete, and determinations of which phase is more likely, at any temperature, cannot be made. In the paragraphs below, the method to obtain a complete energy assessment of a compound in a particular structural arrangement is described.

The total energy of a system of phonons, which are boson particles, is represented as:[38]

$$E(\{n_k\}) = \sum_k \hbar\omega_k n_k \tag{2.30}$$

where the n_k are the number of particles with energy $\hbar\omega_k$, and ω_k is a boson frequency. Using the partition function of the canonical ensemble:

$$Q(V,T) = \sum_{n_k} e^{-E(n_k)/k_B T} = \sum_{n_k} e^{\sum_k(-\hbar\omega_k n_k/k_B T)} \tag{2.31}$$

where T is temperature and k_B is Boltzmann's constant. Simplifying, by understanding that the number of bosons is not conserved:

$$Q(V,T) = \prod_k \Big(\sum_{n=0}^{\infty} e^{\sum_k(\hbar\omega_k n_k/k_B T)n}\Big) = \prod_k \frac{1}{1-e^{-\hbar\omega_k n_k/k_B T}}\Big) \tag{2.32}$$

In the canonical ensemble, the Helmholtz free energy is defined as F = -$k_B T \ln(Q(V,T))$.

Thus, the boson contribution to energy is:

$$F(V,T) = k_B T\Big(\sum_k \ln(1 - e^{(-\hbar\omega_k n_k/k_B T)}\Big) \tag{2.33}$$

The lattice contribution to energy, $E(n_j)$, for a crystal that has N atoms, each with three normal modes of translational freedom, is:

$$E(\{n_j\}) = \sum_{j=1}^{3N} \hbar\omega_j(n_j + \frac{1}{2}) \tag{2.34}$$

where the n_j are the number of particles in the jth state. This equation separates into two terms. The first term is represented as a constrained form of (2.33), while the second term is a constant applicable at all temperatures and is called the zero-point vibrational energy:[38]

$$F_{vib}(V,T) = k_B T\Big(\sum_{j=1}^{3N} \ln(1 - e^{(-\hbar\omega_j n_j/k_B T)}\Big) + \sum_{j=1}^{3N} \frac{\hbar\omega_j}{2} \tag{2.35}$$

where, strictly, $\omega_j = \omega_j(V)$. The dependence on volume is due to the expansion of the crystal with increasing temperature (for most solids). In the less strict harmonic approximation assumption, the phonon dependence on volume is dropped. Ashcroft and Mermin note that computational schemes that include phonon frequency dependence on volume change due to temperature change are suspect, more so if one considers that it is not even clear whether or not the phases investigated are isotropic.[20] Indeed, even one of the calculation engines (ABINIT) used for calculations in this thesis, states that their algorithmic design for computation of thermodynamic properties represents the least stable and clean aspect of their product.[27] Therefore, though phonon frequencies must depend on nuclei locations that

change with lattice responses to temperature, the effects will be included as anharmonic responses, and beyond the scope of this thesis.

A structure's Helmholtz free energy is then the summation of the energy determined at 0 K from DFT and (2.35). A structure's Gibbs free energy can be represented in terms of the Helmholtz free energy as $G = U - TS + PV = F + PV$. In terms of the total differentials of G and F, the relationship between the two energies is:

$$dG = dF + PdV + Vdp \tag{2.36}$$

In a constant pressure environment, $Vdp = 0$. Further, though G includes PV, the difference in the PV term between normalized unit cells, (cells with the same number of atoms), of the same chemical formula are on the order of 0.0005 eV/unit cell at atmospheric pressure. This difference is even smaller than the accepted limits of error resulting from E_{DFT} of 0.001 eV/unit cell. Therefore, when comparing energetics among phases of a particular chemical formula, the PV term is ignored as well.

Chapter 3

Density Functional Theory Study Of Hypothetical $PbTiO_3$-Based Oxysulfides

Reprinted from J. A. Brehm, H. Takenaka, C. W. Lee, I. Grinberg, J. W. Bennett, M. Rutenberg Schoenberg, and A. M. Rappe, Physical Review B., 89, 195202, 2014.

3.1 Abstract

Using density functional theory (DFT) within the local density approximation (LDA), we calculate the physical and electronic properties of $PbTiO_3$ (PTO) and a series of hypothetical compounds $PbTiO_{3\text{-}x}S_x$ x = 0.2, 0.25, 0.33, 0.5, 1, 2, and 3 arranged in the corner-sharing cubic perovskite structure. We determine that replacing the apical oxygen atom in the PTO tetragonal unit cell with a sulfur atom reduces the x = 0 LDA calculated band gap of 1.47 eV to 0.43 - 0.67 eV for x = 0.2 - 1 and increases the polarization. PBE0 and GW methods predict that the compositions x = 0.2-2 will have band gaps in the visible range. For all values of $x < 2$, the oxysulfide perovskite retains the tetragonal phase of $PbTiO_3$,

and the a lattice parameter remains within 2.5% of the oxide. Thermodynamic analysis indicates that chemical routes using high temperature gas, such as H_2S and CS_2, can be used to substitute O for S in PTO for the compositions x = 0.2 - 0.5.

3.2 Introduction

In this paper, we use first principles calculations to study the physical and electronic properties of hypothetical polar oxysulfide perovskite solid solutions of the chemical formula $PbTiO_{3\text{-}x}S_x$. We seek to identify new photovoltaic materials for efficient solar energy conversion. Photovoltaic materials must have band gaps in the range 1.1 - 2 eV to provide strong light absorption and energy conversion. The best single-junction materials, such as silicon, CdTe, and copper indium selenide, exhibit gaps near the Shockley and Queisser (SQ) detailed balance model optimal value of 1.3 eV. Photons with energies less than the band gap will not promote electrons to the conduction band, while electrons absorbing photons with energies greater than the conduction band minimum will lose energy as the electrons decay to the band edge. To surpass the single-material SQ limit, photovoltaics with a range of band gaps are arranged in multi-junction solar cells, $e.\ g.$ $CuIn_xGa_{1\text{-}x}Se_2$ and InGaP/GaAs/InGaAsN/Ge.[39, 40] In addition to a good match between the band gap and the solar spectrum, excited carrier recombination must be prevented in order to obtain the photocurrent. This is typically done by an electric field generated at a $p-n$ junction that moves the holes and the excited electrons in opposite directions. Another recently studied method has been to use ferroelectric materials, for which the strong inversion symmetry breaking and spontaneous polarization give rise to the separation of charge carriers in the bulk of the material (bulk photovoltaic effect). The known perovskite $BiFeO_3$[41] and new materials including $[KNbO_3]_{1-x}[BaNi_{1/2}Nb_{1/2}O_{3-\delta}]_x$,[8] $KBiFe_2O_5$,[42] and $Bi_4Ti_3O_{12}$-$LaCoO_3$[43] are examples of polar oxide materials with band gaps in the visible range in

which the bulk photovoltaic effect has been observed.

We choose the classic $PbTiO_3$ (PTO) ferroelectric perovskite oxide as a basis for alloying with sulfur on the oxygen sites. PTO is highly polar (P = 0.88 C/m^2) and has an indirect band gap of ≈3.45 - 3.6 eV.[44-47] Excitation across the gap is essentially a charge transfer from the O $2p$ orbitals to the Ti $3d$ orbitals. Therefore, substitution of the more electronegative oxygen by the less electronegative sulfur should lead to a lower band gap, while possibly preserving the ferroelectricity. The substitution of oxygen by sulfur or vice versa in order to tailor band gaps is well documented in other materials.[12-14] Unlike replacement of oxygen with nitrogen or titanium with nickel to lower band gaps,[7, 48] the substitution of isovalent sulfur in place of oxygen does not require vacancies to preserve charge neutrality.

While simple corner-sharing oxysulfide perovskites have yet to be reported in the literature, closely related and more complicated oxysulfides do exist. They have been reported as either Ruddlesden-Popper phases[49-51] or as layered materials with perovskite-like oxide layers alternating with either antifluorite or rock salt sulfide layers.[52-55] Thus the current work is novel in that it explores the feasibility of synthesizing a purely corner-sharing perovskite phase.

3.3 Methodology

All density functional theory (DFT) calculations in this study are performed using the local density approximation (LDA). The DFT packages we use in this study are ABINIT[56] and Quantum Espresso.[57] The atoms are represented by norm-conserving optimized pseudopotentials[58] generated using OPIUM, [59] and all, except oxygen, are further refined using the designed non-local methodology.[30] We pseudize the following orbitals: $2s$ and $2p$ for O; $3s$, $3p$, and $3d$ for S; $5d$, $6s$, and $6p$ for Pb; and $3s$, $3p$, $3d$, $4s$, and $4p$ for

Ti. The pseudopotentials are optimized for a 50 Ry plane-wave cutoff, and all solid-state calculations use this value.

ABINIT is used for relaxation calculations, in order to determine unit cell parameters, atomic positions, and relative energies. For the standard perovskite unit cell of five atoms, a Monkhorst-Pack (MP) k-point grid[60] of $8\times8\times8$ is used (though results using a $4\times4\times4$ grid are quite similar to those using an $8\times8\times8$ grid). For calculations requiring a doubling of the unit cell in a Cartesian direction, the MP grid is set to 4 for that dimension.

In order to determine the preferred location of S atoms for $PbTiO_{3-x}S_x$ with x = 1 and x = 2, we perform two sets of calculations. In the first set, a five-atom unit cell is used. We evaluate all the possible locations of a minority species anion in a tetragonal perovskite cell. We also consider the paraelectric, cubic perovskite and displace the anions above and below an imaginary center plane that intersects four of the six anions of the octahedron. For initial cell parameters, we use two strain states as well: a compressed case and an expanded case. For the compressed case, the cell parameters are a = 3.87 Å and c = 4.07 Å for the tetragonal cells and a = 4.09 Å for the cubic cells. (As will be shown later, the cell parameters used for the tetragonal/compressed case were calculated from a five-atom PTO relaxation.) The a lattice parameter in the cubic case is determined by setting the Pb-O-Pb face diagonal length equal to twice the sum of the ionic radii of a 12-coordinated Pb^{2+} (1.49 Å) and a six-coordinated O^{2-} (1.40 Å). [61] For the expanded cells, cell parameters are increased by a factor of 1.31, which represents the radius ratio of six-coordinated S^{2-} (1.84 Å) to six-coordinated O^{2-}.[61]

For the second set of calculations, we consider ten-atom unit cells consisting of two PTO unit cells with either the a or the c lattice parameter doubled. Ten-atom unit cells also accommodate x = 0.5 concentrations. We evaluate all of the cases in which a S atom may occupy any of the six O positions for the x = 0.5 system, and all of the ways that two minority species anions may occupy the six anion locations for the x = 1 and x = 2 systems.

The systems x = 0 and x = 3, with only one anion species, have only one configuration and were relaxed from five-atom cubic unit cells with an initial starting a lattice parameter derived from ionic radii sums.

In order to extend our analysis to lower concentrations of S, we create unit cells by inserting one, two and three PTO layers into the relaxed x = 0.5 structure while keeping the S atom confined to the (001). These compositions have x = 0.33, 0.25, and 0.2 respectively. All systems are considered to be fully relaxed when successive self-consistent iterations yield total energy differences less than 10^{-8} Ha/cell and atomic forces less than 10^{-4} Ha/Bohr. The FINDSYM package[62, 63] is used to determine the space groups of the relaxed structures. In order to assess whether or not any of the systems prefer a Glazer tilt system structure,[64] a set of relaxation calculations is performed on 40-atom $2\times2\times2$ unit cells for the x = 0, 0.5, 1, 2, and 3 compositions. The starting locations of the S atoms for x = 0.5, 1, and 2 are determined from the earlier five- and ten-atom relaxations. Polarization calculations are carried out using ABINIT, while band gap and projected density of states (PDOS) calculations are performed using Quantum Espresso with $12\times12\times12$ k-point grids. Post-DFT band gap investigation is carried out using the PBE0[34] method as implemented in Quantum Espresso, and the GW[65] method as implemented in ABINIT.[37, 66, 67] The nature of the bonding in x = 0, 0.5, 1, and 2 systems is assessed using a Bader charge analysis package.[68, 69]

3.4 Results and Discussion

3.4.1 Structural and electronic results for end-members $PbTiO_3$ and $PbTiS_3$.

Our calculated results for the end member, $PbTiO_3$, are in agreement with earlier published theoretical work.[70-72] The relaxed lattice parameters are a = 3.87 Å and c = 4.07 Å, yielding a c/a ratio of 1.05. We find an indirect (X-Γ) band gap of 1.47 eV and polarization (strictly in the z direction) of 0.85 C/m^2. These results, as well as all the physical and electronic properties for $PbTiO_{3-x}S_x$ x = 0 and x = 3 and high symmetry $PbTiO_{3-x}S_x$ x = 0.2 - 2 are listed in Tables 3.1 and 3.2. Since the LDA calculated band gap underestimates the experimental band gap, post-DFT methods must be applied. For PTO, we calculate a band gap of 3.44 eV using the PBE0 method, (with the α parameter set to 0.25), and a gap of 4.10 eV by the GW method. To our knowledge, only one other theoretical study[33] has applied the GW method to calculate the band gap in PTO and the calculations are consistent. Since the GW result overestimates the experimental PTO band gap, we investigate whether the semi-core states incur greater exchange-correlation errors by calculating the GW gap without the semi-core states of Pb and Ti in the valence space. However, this leads to only a 0.2 eV reduction in the PTO band gap. We therefore surmise that the PBE0 method is probably a slightly better predictor of the band gap for the oxysulfide systems. We do not use the LDA+U method, as an earlier paper reports a band gap of only 2.17 eV with this technique.[33]

Within the cubic corner-sharing motif, $PbTiS_3$ is found to be a $a^+b^-b^-$ tilt system with $a \approx 12°$ and $b \approx 15°$, as determined from the 40-atom 2×2×2 relaxation. A further relaxation, this time on a standard 20-atom unit cell arranged in the $Pnma$ structure, yields the same structure as the 40-atom relaxation. Thus, we conclude that the ground state for $PbTiS_3$ arranged in the corner-sharing perovskite mode is $Pnma$. While the LDA elec-

tronic structure calculations predict that it is metallic and nonpolar, the PBE0 calculated gap is 0.86 eV. With the minimum representation for the $Pnma$ tilt system being a 20-atom unit cell, the GW method is not applied here as it is computationally expensive. [33] Also, if we restrict the five atom unit cell to the $P4mm$ space group, which is higher in relative energy to the $Pnma$ phase, even though an LDA band gap calculation again shows the compound to be metallic, a gap of 1.60 eV is obtained by the PBE0 method and a 1.19 eV gap by the GW method. With a band gap in the visible range and associated polarization stemming from its non-centrosymmetric nature, $PbTiS_3$ arranged in the $P4mm$ space group has the properties required for a bulk photovoltaic effect material. This contrasts with the low energy $Pnma$ formation, which is centrosymmetric and thus not suitable for bulk photovoltaic effect purposes. However, tempering these results is the fact that $PbTiS_3$ has not been made, and the only synthesized stoichiometries known for the Pb-Ti-S system are misfit layered compounds with chemical formula $(PbS)_{1.18}(TiS_2)$ and $(PbS)_{1.18}(TiS_2)_{0.8475}$.[73] In these compounds, distorted rock salt-like PbS layers are intercalated with TiS_2 edge-sharing sheets.

Table 3.1: Calculated structural properties for $PbTiO_3$, $PbTiS_3$, and high symmetry $PbTiO_{3\text{-}x}S_x$ x = 0.2 - 2. The c/a ratios are normalized according to the number of octahedra in the unit cell. [Reprinted from J. A. Brehm, H. Takenaka, C. W. Lee, I. Grinberg, J. W. Bennett, M. Rutenberg Schoenberg, and A. M. Rappe, Physical Review B., 89, 195202, 2014. Copyright 2014 by the American Physical Society.]

	Unit Cell Lengths (Å) (and Unit Cell Angles where $\neq 90°$)			c/a	Space
x	a	b	c	Ratio	Group
0	3.87	3.87	4.07	1.05	$P4mm$
0.2	3.86	3.86	21.70	1.12	$P4mm$
0.25	3.85	3.85	17.65	1.15	$P4mm$
0.33	3.85	3.85	13.57	1.17	$P4mm$
0.5	3.84	3.84	9.56	1.24	$P4mm$
1	3.78	3.78	5.64	1.49	$P4mm$
2	4.86 (α = 90.37°)	4.86 (β = 89.63°)	3.76 (γ=90.23°)	0.77	$P1$
3	9.31	9.31	9.25	0.99	$Pnma$

Table 3.2: Calculated electronic properties for $PbTiO_3$, $PbTiS_3$, and high symmetry $PbTiO_{3-x}S_x$ x = 0.2 - 2. For x = 0.5, 1, and 2, the LDA band gaps and total polarization ranges for all ten-atom unit cells are included in parentheses. GW band gaps calculated using pseudopotentials without semi-core states are listed in parentheses. In comparison, the experimental band gap for x = 0 has been reported between ≈3.45 - 3.6 eV.[44-46] [Reprinted from J. A. Brehm, H. Takenaka, C. W. Lee, I. Grinberg, J. W. Bennett, M. Rutenberg Schoenberg, and A. M. Rappe, Physical Review B., 89, 195202, 2014. Copyright 2014 by the American Physical Society.]

	Band Gap (eV)			Polarization (C/m^2)			
x	LDA	PBE0	GW	P_x	P_y	P_z	P
0	1.47	3.44	4.10 (3.90)	-	-	0.85	0.85
0.2	0.45	2.08		-	-	0.87	0.87
0.25	0.46	2.11		-	-	0.87	0.87
0.33	0.48	2.12		-	-	0.88	0.88
0.5	0.60 (0.60 - 0.89)	2.19	2.69 (2.50)	-	-	0.92	0.92 (0.92 - 1.13)
1	0.67 (0.14 -1.15)	2.25	2.60 (2.41)	-	-	1.11	1.11 (0.71 - 1.13)
2	0.33 (0.05 - 1.18)	1.77	1.38 (1.33)	0.24	0.23	0.27	0.43 (0.28 - 0.95)
3	0.00	0.86	1.19[a]	-	-	-	-

[a]Band gap evaluated for a five-atom unit cell arranged in the $P4mm$ space group.

3.4.2 Structural Properties of $PbTiO_{3-x}S_x$.

We find that S substitution x = 0.5 and 1 preserves the tetragonal $P4mm$ structure and leads to a small decrease of the a lattice constant and a considerable increase in the c lattice constant and the c/a ratio, reaching c = 5.64 Å and c/a = 1.49 for x = 1. (See Table 3.1.) For x = 0.5, the two octahedra differ, with one having c = 4.58 Å and the other having c = 4.98 Å, as a result of different chemical environments. The large tetragonality values are in agreement with octahedral cage sizes that have been observed experimentally in oxysulfides. For example, in $A_2CoO_2Cu_2S_2$ (A= Sr, Ba) solid solutions, Smura *et al.*[55] have found c/a ratios ranging between 1.52 and 1.66 for CoO_4S_2 octahedra. Similarly, Ishikawa *et al.*[49] have found an average c/a ratio of 1.6 for $Ln_2Ti_2O_5S_2$ (Ln = Pr, Nd, Sm, Gd, Tb, Dy, Ho, Er).

The preferred location for the substituent S atoms is apical for x = 0.5 and 1, such that the B-S-B bonds are along the c-axis. This location for the S atom in x = 1 and x = 0.5 has been observed experimentally in layered oxysulfide perovskites where the S-M-S bonds in MO_4S_2 single octahedra[55] and the S-M-O-M-S bonds for pairs of octahedra of the form MO_5S connected by an oxygen,[49] are linear along the c axes of elongated octahedra. We do not observe any octahedral tilting for these structures. The structures for x = 0, 0.5, 1, and 2 are shown in Figure 3.1.

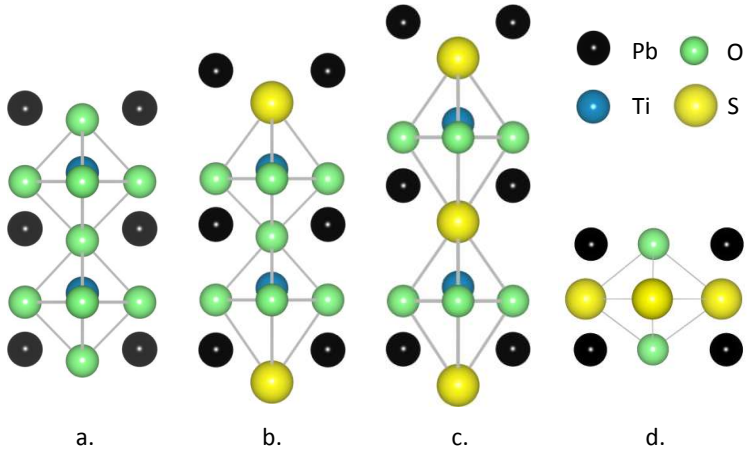

Figure 3.1: Relaxed structures of $PbTiO_{3-x}S_x$: (a.) two unit cells of $x = 0$, (b.) one unit cell of $x = 0.5$, (c.) two unit cells of $x = 1$, and (d.) one unit cell of $x = 2$. The view is of the ac-plane. All dimensions and ionic radii are to scale, except the Ti ions which are enlarged for clarity. Images created with VESTA.[2] [Reprinted from J. A. Brehm, H. Takenaka, C. W. Lee, I. Grinberg, J. W. Bennett, M. Rutenberg Schoenberg, and A. M. Rappe, Physical Review B., 89, 195202, 2014. Copyright 2014 by the American Physical Society.]

Relaxation calculations on compositions x = 0.2, 0.25, and 0.33 show that the a lattice parameters are within 0.5% of each other and the x = 0 and x = 0.5 compositions, the c lattice parameter increases by multiples of the length of the PTO unit cell, 4.07 Å, as one would expect, and the high symmetry $P4mm$ phase is maintained.

The $PbTiO_{3-x}S_x$ compositions x = 0 - 1 have very similar cation-anion bond lengths. These are reported in Table 3.3. Indeed, all Ti-O lengths are nearly equal to the PTO values. In order to corroborate our Pb-S bond length results, we have also calculated the lattice constant and Pb-S bond length for rock salt PbS. Our PbS lattice constant of 5.85 Å is in excellent agreement with the previously reported theoretically calculated values.[74, 75] Also, our Pb-S bond length of 2.93 Å is within 0.02 Å of the values reported in these works. Thus, the compositions $PbTiO_{3-x}S_x$ with x = 0 - 1 form crystals that maintain the nearest neighbor (NN) cation-anion bond lengths of PTO and rock salt PbS.

Table 3.3: Selected cation-anion bond lengths and z-displacements for $PbTiO_{3-x}S_x$ x = 0 - 1. All lengths in Å. NN = nearest neighbor. For x = 0.20, 0.25, and 0.33, average values for Pb - NN apical O, Ti - equatorial O, and Ti - NN apical O are tabulated. Pb - S and Ti - NN S average values are also listed. Δz is defined as the separation in the z coordinate between two ions. [Reprinted from J. A. Brehm, H. Takenaka, C. W. Lee, I. Grinberg, J. W. Bennett, M. Rutenberg Schoenberg, and A. M. Rappe, Physical Review B., 89, 195202, 2014. Copyright 2014 by the American Physical Society.]

	Pb - NN apical O		Pb-S		Ti - equatorial O	
x	bond length	Δz	bond length	Δz	bond length	Δz
0	2.76	0.39	-	-	1.96	0.30
0.20	2.76	0.40	2.92	1.05	1.95	0.32
0.25	2.75	0.40	2.92	1.06	1.95	0.32
0.33	2.75	0.40	2.92	1.06	1.95	0.33
0.50	2.75	0.41	2.93	1.10	1.95	0.35
1	-	-	2.95	1.24	1.95	0.48

	Ti - NN apical O	Ti - NN S
x	bond length	bond length
0	1.78	-
0.20	1.78	2.31
0.25	1.78	2.31
0.33	1.78	2.31
0.50	1.77	2.30
1	-	2.25

The results for the x = 2 composition differ markedly from the x = 0.5 and x = 1 systems. The x = 2 composition has very low symmetry ($P1$), $c/a < 1$, and lattice angles that all differ from 90° by up to 0.37°. Relaxation of the various ten-atom unit cells shows the minority species anions, in this case O, again prefer to be located trans to each other, forming ≈180° O-Ti-O angles. Relaxation of the 40-atom 2×2×2 unit cell does not result in any tilting.

Further analysis of the atom locations in the x = 2 unit cell shows significant distinctions from the x = 0 - 1 compounds. First, the anion displacement is no longer only in the z direction. The S anions are displaced from high-symmetry positions up to ≈0.08 Å in the x and y directions, and the O anion is displaced 0.04 Å in both x and y. Moreover, while the short Ti - apical O bond length is 1.75 Å, which is almost identical to that for compositions x = 0 - 1, (see Table 3), the displacement of the Ti atom relative to the equatorial anions is much reduced relative to those other compositions. The x = 0 - 1 compositions have displacements strictly in the z direction with magnitudes monotonically increasing from 0.30 to 0.48 Å; however the x = 2 system shows displacements in all three Cartesian directions: 0.08 Å in x, 0.02 Å in y, and 0.20 Å in z. This leads to a total displacement magnitude 0.22 Å. Unlike the x = 0 - 1 compounds, the Pb sublattice only displaces by a relatively smaller 0.07 Å in the z direction, but it also displaces 0.19 Å in the x and y directions. The total displacement of 0.27 Å is smaller than the 0.39 Å Pb - O z displacement in PTO and much smaller than the Pb - S displacements in the compounds with x = 0.2 - 1 (which are greater than 1 Å). The offset of Pb in the xy plane leads to two distinct Pb - S bond lengths: one that averages 2.90 Å, and one much larger, averaging 3.21 Å. The smaller Pb - S bond length is in agreement with the data for the x = 0.2 - 1 compounds, and is only 0.03 Å smaller than the calculated Pb - S bond length for rock salt PbS. The Ti - S bond lengths range from 2.40 Å to 2.48 Å. These bond lengths are basically the sum of the ionic radii of Ti (0.605 Å) and S (1.84 Å).

3.4.3 Electronic properties of $PbTiO_{3-x}S_x$.

Table 3.2 clearly shows that as x increases from 0 to 1, $P = P_z$, and P increases monotonically from 0.85 to 1.11 C/m^2. For x = 2, P is reduced to 0.43 C/m^2, with significant P components in each Cartesian direction of ≈0.25 C/m^2. This suggests a morphotropic phase boundary between x = 1 and x = 2, potentially leading to high piezoelectricity. The reduced P for x = 2, with significant components in all three Cartesian directions, is confirmed by the smaller displacement vectors for Pb and Ti as described earlier.

As shown in Table 3.2, the LDA band gap results are all in the infrared range for x = 0.2 - 2. Each gap is X-Γ indirect, as seen experimentally for PTO. Band structure diagrams for x = 0 and x = 1 are shown in Figure 3.2. The narrowing of the band gap for x = 1 relative to x = 0 is evident. The conduction bands are moved up and the valence bands are moved down to correct to the PBE0 values, due to the well-known LDA underestimation of E_g. When PBE0 is applied to x = 0.2 - 2, and GW is applied to x = 0.5, 1, and 2, the calculated gap magnitudes are well within the visible range.

The ranges of LDA band gap and polarization values for all relaxed ten-atom configurations for x = 0.5, 1, and 2 are also included in Table 3.2. However, except for one configuration, the likelihood of achieving a different configuration, (and hence the associated electronic properties), than the high-symmetry one, is very small, as they have relative energies greater than 0.27 eV/five-atoms higher than the respective ground state. The one case, with S atoms sharing the edge of an octahedron in x = 1, has a relative energy 0.05 eV/five-atoms higher than the high symmetry ionic configuration and still has a significant LDA band gap (1.15 eV) and polarization (0.83 C/m^2). Therefore, we expect that replacing O with S in these concentrations will lead to materials suitable for bulk photovoltaic use.

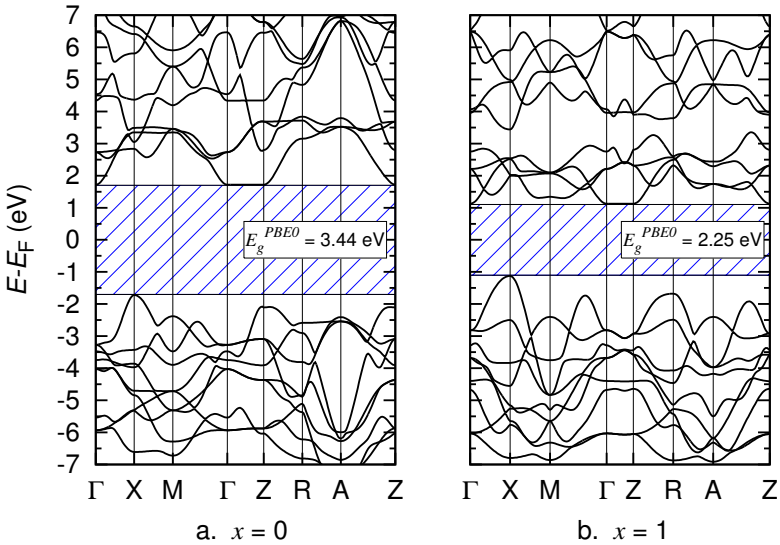

Figure 3.2: LDA band structure with the conduction bands moved up and the valence bands moved down to portray the PBE0 band gap: (a.) $PbTiO_3$ (x = 0) and (b.) $PbTiO_2S$ (x = 1). [Reprinted from J. A. Brehm, H. Takenaka, C. W. Lee, I. Grinberg, J. W. Bennett, M. Rutenberg Schoenberg, and A. M. Rappe, Physical Review B., 89, 195202, 2014. Copyright 2014 by the American Physical Society.]

Atom-projected density of states calculations for x = 0.20, 0.25, and 0.33 are remarkably similar. A representative diagram is shown for x = 0.25 in Figure 3.3. The densities of states show that the reduced band gap relative to PTO is a result of the higher energy S $3p$ orbitals relative to O $2p$ orbitals. Note that the influence of S on the other atoms is limited to its nearest neighbors. Specifically, the top of the valence band has contributions from the $3d$ orbitals of the NN and second NN Ti atoms, the $6s$ and $6p$ orbitals of the NN Pb atom, and the $2p$ of the NN and second NN O atoms.

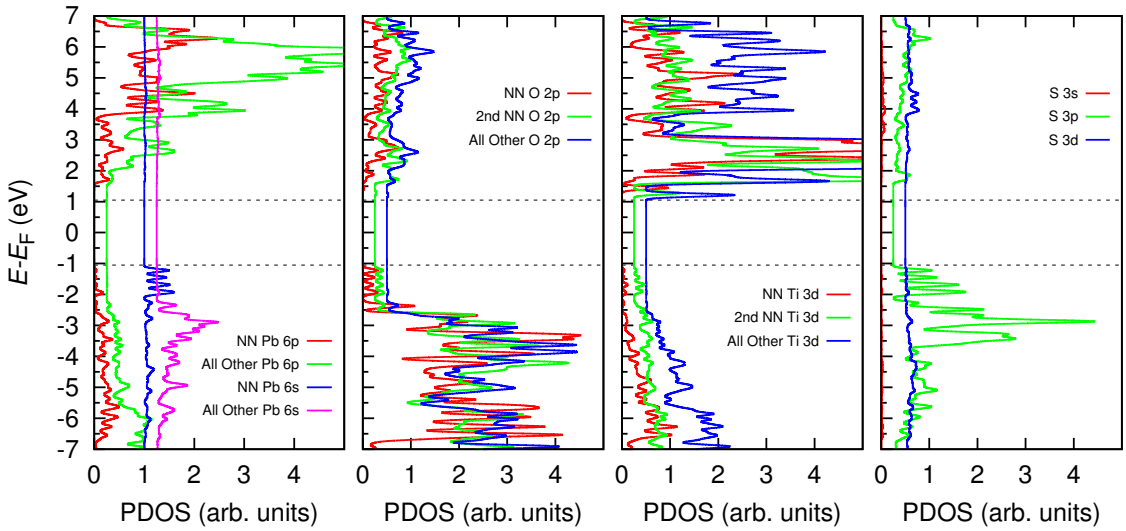

Figure 3.3: Orbital-projected density of states plots for $PbTiO_{3-x}S_x$, x = 0.25, with the conduction states moved up and the valence states moved down to portray the PBE0 band gap of 2.11 eV. NN and 2nd NN stand for nearest neighbor and second nearest neighbor of the species with respect to S. [Reprinted from J. A. Brehm, H. Takenaka, C. W. Lee, I. Grinberg, J. W. Bennett, M. Rutenberg Schoenberg, and A. M. Rappe, Physical Review B., 89, 195202, 2014. Copyright 2014 by the American Physical Society.]

Bader charge analysis can be used to estimate the ionic charges of atoms in molecules and compounds. The Bader charge analysis results, from calculations performed on wavefunctions generated with the post-DFT PBE0 method, are shown in Table 3.4. These data show that as the sulfur concentration increases, there is a monotonic decrease in the ionic charges of the cations and anions (with small exceptions) for the x = 0, 0.5, 1, and 2 compositions, as the compounds become less ionic and more covalent. This is due to the S being less electronegative than O. Further, in x = 0.5, all atomic species closer to S display ionicities smaller than their respective counterparts further away from S. Bader charge analysis can also be used to confirm trends in band gaps of solutions. In general, our Bader charge analysis results suggest that increasing the concentration of S will lead to compounds with smaller band gaps through reduced overall ionicity. However, on increasing S from x = 0.5 to x = 1, the PBE0 band gaps are 2.19 and 2.25 eV but the overall ionicities are 3.54 and 3.46 . An examination of PDOS alleviates this inconsistency and suggests a different correlation between ionicity and band gap. In x = 0.5, the PDOS indicates that electronic states of the NN Ti to S occupy the conduction band edge, while the other Ti (in x = 0.5) has conduction band states that are approximately 0.015 eV higher in energy. This NN Ti to S also has a smaller ionicity of 2.16 as compared to the other Ti (in x = 0.5) which has an ionicity of 2.26. More importantly, the ionicity of this NN Ti to S (in x = 0.5) has a smaller ionicity than the Ti to S in x =1 by 0.03 units. Thus, these data indicate that the relevant correlation is between NN Ti ionicity and band gap, since the orbitals of these atoms set the edge of the conduction band.

Table 3.4: Bader charge analysis results for x = 0, 0.5, 1, and 2. For x = 0.5, two data entries are given per element: the ionicity value for those atoms farther away from the S atoms is listed first. The summation of cation charges (or negative anion charges) per five atoms is represented by $\sum_i C_i$ = -$\sum_i A_i$. [Reprinted from J. A. Brehm, H. Takenaka, C. W. Lee, I. Grinberg, J. W. Bennett, M. Rutenberg Schoenberg, and A. M. Rappe, Physical Review B., 89, 195202, 2014. Copyright 2014 by the American Physical Society.]

	x			
Species	0	0.5	1	2
Pb	1.43	1.39, 1.26	1.27	1.13
Ti	2.31	2.26, 2.16	2.19	2.05
Equatorial O	-1.27	-1.27, -1.19	-1.25	-
Equatorial S	-	-	-	-1.02
Apical O	-1.19	-1.18	-	-1.14
Apical S	-	-0.99	-0.97	-
Charge sum	3.73	3.54	3.46	3.18

3.4.4 Formation energy results for replacing O with S in $PbTiO_3$

Our literature review finds that no $PbTiO_{3\text{-}x}S_x$ have been made. Thus, in this section, we evaluate whether such synthesis is energetically feasible. We consider replacing O with S via gaseous reagents. While several experimenters have used H_2S and CS_2 to convert oxides to sulfides,[76-79] Ishikawa *et al.* have succeeded in replacing just the apical O of the TiO_6 octahedra with S to create ordered oxysulfides.[49] We calculate the standard Gibbs free energy of reaction, ΔG^0, of creating $PbTiO_{3-x}S_x$ with x = 0.2 - 3 in the energetically preferred configurations discussed above by comparing the sum of the G^0 of the products to that of the reactants for three different substitution scenarios:

$$\mathrm{PbTiO_3}(s) + \frac{x}{2}\mathrm{S_2}(g) \;\rightarrow\; \mathrm{PbTiO_{3-x}S_x}(s) + \frac{x}{2}\mathrm{O_2}(g) \tag{3.1}$$

$$\mathrm{PbTiO_3}(s) + x\mathrm{H_2S}(g) \;\rightarrow\; \mathrm{PbTiO_{3-x}S_x}(s) + x\mathrm{H_2O}(g) \tag{3.2}$$

$$\mathrm{PbTiO_3}(s) + \frac{x}{2}\mathrm{CS_2}(g) \;\rightarrow\; \mathrm{PbTiO_{3-x}S_x}(s) + \frac{x}{2}\mathrm{CO_2}(g) \tag{3.3}$$

Here, standard state is defined as $p^0_{\mathrm{O_2}}$ = 1 bar = 0.987 atm. In order to compute ΔG^0 we use:

$$\begin{aligned}\Delta G^0(T) \;=\;& [E_{\mathrm{DFT,solid}} + F_{\mathrm{vib,solid}}(T) + H^0_{\mathrm{gas}} - T(S^0_{\mathrm{gas}})]_{\mathrm{products}} \\ &- [E_{\mathrm{DFT,solid}} + F_{\mathrm{vib,solid}}(T) + H^0_{\mathrm{gas}} - T(S^0_{\mathrm{gas}})]_{\mathrm{reactants}} \\ &+ \Delta(pV) - T\Delta S^{\mathrm{conf}}\end{aligned} \tag{3.4}$$

where p is pressure, V is volume, and S^{conf} is configurational entropy. In a constant pressure reaction, at 0 K and one bar, the difference in pV energy contribution of the solid products and reactants is on the order of 1×10^{-5} eV/5-atom. At reaction temperatures, the volume difference between the products and reactants is not expected to change much,

leaving $\Delta(pV)$ negligible, and it will not be considered further. For S^{conf}, only the solid product needs to be considered as the solid reactant is a pure compound and the gaseous species in both the reactant and product can be regulated to be predominantly the reactant gas, as was the case in the experimental works cited above in which flowing reactant gas was used.[79, 49] For calculation purposes, we assume an ideal solution, with no excess free energy of mixing.

$G^0_{\mathrm{solid}}(T)$ is described as the sum of solid state DFT total energy ($E_{\mathrm{DFT,solid}}$) and the harmonic vibrational Helmholtz free energy [$F_{\mathrm{vib,solid}}(T)$]. The harmonic vibrational Helmholtz free energy is the sum of the harmonic vibrational internal energy and the product of temperature and the harmonic vibrational entropy:

$$F_{\mathrm{vib,solid}}(T) = \sum_{s=1}^{3N} \left\{ \frac{\hbar\omega_s}{2} + k_B T \ln\Big[1 - \exp\Big(\frac{-\hbar\omega_s}{k_B T}\Big)\Big] \right\} \tag{3.5}$$

where N represents the number of atoms in the system, ω_s represents a Γ-point normal mode frequency, k_B is the Boltzmann constant, and T is temperature.

For the gaseous species, the $\Delta G^0(T)$ values at finite temperatures are determined based on their E_{DFT} and the NIST-JANAF thermochemical tables of each species. We calculate molecular total energies by summing atomic energies obtained from spin polarized DFT calculations and the molecular atomization energies obtained from NIST.[80] Vibrational free energies of the gaseous species are determined using frequencies from the NIST-JANAF thermochemical tables. As shown in Table 3.5, our calculations show that in the temperature range 900 - 1300 K, replacing O with S in PTO is energetically favorable in $CS_2(g)$ and $H_2S(g)$ environments for x = 0.2 - 0.5 at atmospheric pressure. At 1300 K, $S_2(g)$ can be used to substitute O for S for x = 0.2 and 0.25.

Table 3.5: $\Delta G^0(T)$ (eV/5-atom PTO unit cell) calculations for various oxysulfide compositions formed by replacing O with S in PTO using the reactant indicated at 900, 1100, and 1300 K. [Reprinted from J. A. Brehm, H. Takenaka, C. W. Lee, I. Grinberg, J. W. Bennett, M. Rutenberg Schoenberg, and A. M. Rappe, Physical Review B., 89, 195202, 2014. Copyright 2014 by the American Physical Society.]

	H_2S			CS_2		
x	900 K	1100 K	1300 K	900 K	1100 K	1300 K
0.2	-0.26	-0.40	-0.54	-0.35	-0.49	-0.63
0.25	-0.20	-0.33	-0.47	-0.31	-0.44	-0.58
0.33	-0.10	-0.21	-0.34	-0.25	-0.37	-0.49
0.5	0.11	0.01	-0.07	-0.12	-0.22	-0.31
1	0.74	0.74	0.74	0.29	0.28	0.28
2	1.08	1.01	0.95	0.17	0.10	0.02
3	1.81	1.74	1.66	0.46	0.36	0.26

	S_2		
x	900 K	1100 K	1300 K
0.2	0.04	-0.10	-0.25
0.25	0.17	0.04	-0.10
0.33	0.39	0.27	0.14
0.5	0.85	0.75	0.65
1	2.24	2.21	2.19
2	4.03	3.94	3.85
3	6.24	6.13	6.00

3.5 Conclusions

We have shown that for the perovskite structure evaluated in ten-atom unit cells, the lowest energy state of $PbTiO_{3-x}S_x$ x = 0.5, 1, and 2 is tetragonal with the minority species atoms located on apical sites of the octahedra. The resulting structures for x = 0.5 and 1, as well as for x = 0.2, 0.25, and 0.33, are tetragonal with a lattice parameters within 2.5% of the parent, $PbTiO_3$. Our results also show that the use of $CS_2(g)$ and $H_2S(g)$ to replace O with S in PTO is a viable method to synthesize the compounds with x = 0.2 - 0.5. With respect to electronic properties, the polarization values of the x = 0.2 - 1 materials are greater than that of the parent PTO and increase with increasing S concentration. The band gaps of the x = 0.2 - 2.0 systems were evaluated by the post-DFT method of PBE0, and, for x = 0.5, 1 and 2, by the GW method as well, and found to be in the visible range. Thus, $PbTiO_{3-x}S_x$ x = 0.2 - 2 are predicted to have significant polarization and low band gaps, and should be considered solar bulk photovoltaic material candidates.

3.6 Acknowledgements

HT and JWB were supported by the Office of Naval Research, under grant N00014-12-1-1033. IG was supported by the National Science Foundation, under grant DMR11-24696. CWL was supported by the Office of Naval Research, under grant N00014-11-1-0664. JAB and MRS were supported by the Department of Energy Office of Basic Energy Sciences, under grant number DE-FG02-07ER46431. AMR was supported by the Air Force Office of Scientific Research, Air Force Material Command, USAF, under grant FA9550-10-1-0248. Computational support was provided by the HPCMO of the U.S. DoD and the NERSC center of the U.S. DoE. The authors thank Prof. Graeme Henkelman for useful discussions on use of his group's Bader Analysis code. The authors also thank Prof. Harold Stokes for useful communication concerning application of his group's FINDSYM code.

Chapter 4

First-Principles Calculation of the Bulk Photovoltaic Effect in the Polar Compounds $LiAsS_2$, $LiAsSe_2$, and $NaAsSe_2$

Work completed in collaboration with S. M. Young, F. Zheng, and A. M. Rappe. Submitted for peer review to the Journal of Chemical Physics on August 12, 2014.

4.1 Abstract

We calculate the shift current response, which has been identified as the dominant mechanism for the bulk photovoltaic effect, for the polar compounds $LiAsS_2$, $LiAsSe_2$, and $NaAsSe_2$. We find that the magnitudes of the photovoltaic responses in the visible range for these compounds exceed the maximum response obtained for $BiFeO_3$ by 10 - 20 times. We correlate the high shift current response with the existence of p states at both the valence

and conduction band edges, as well as the dispersion of these bands, while also showing that high polarization is not a requirement. With low experimental band gaps of less than 2 eV and high shift current response, these materials have potential for use as bulk photovoltaics.

4.2 Introduction.

The bulk photovoltaic effect (BPVE) is the phenomenon in which electromagnetic radiation imparted on a single-phase insulating or semi-conducting material leads to a zero-voltage photo-current. Like traditional photovoltaics, ($e.\ g.$ Si, CdTe, CIGS, and GaAs), in order for a material to exhibit a significant BPVE response from sunlight and thus be useful as a solar energy harvesting material, it needs to have a band gap in the visible spectrum (1.1 - 3.1 eV) or the near-infrared. Unlike traditional photovoltaics, which require an interface between two materials, the BPVE is achieved through the broken inversion symmetry in a single material.[81, 5, 3] Additionally, only materials with nonzero polarization can give a current in response to unpolarized light, making them materials of interest for solar conversion. This constraint stems from the physics of the non-linear optical process termed "shift current," which has been demonstrated in earlier theoretical works is the dominant mechanism for generating the BPVE in the ferroelectrics $BiFeO_3$, $BaTiO_3$ and $PbTiO_3$[4, 81]; if a material is non-centrosymmetric but possesses no polarization, then the directions of the generated shift currents from unpolarized light will sum to zero and produce no net current.[1] Many oxide perovskites have both of these properties, and the BPVE effect has been realized experimentally in them.[8, 82-87]

Further, based on the data from studies on $BaTiO_3$ and $PbTiO_3$, it was suggested that materials with elemental combinations conducive to covalent bonding and delocalized electronic states can lead to large shift current effects.[81] Our data also indicated that the mag-

nitude of polarization is not simply proportional to the shift current produced.[81] These observations have shaped our materials search. We avoid $A_aB_bX_x$ compounds with B-sites that have transition metals possessing localized conduction band electronic states, and concentrate on compounds with B-X electronegativity differences less than one. A natural set of B-X combinations that meet these criteria are compounds with B-sites from Groups 14 and 15, and X-sites from Groups 16 and 17, except for O and F which have too high an electronegativity to meet the covalency requirement. In order to broaden the search, we remove the perovskite requirement of $a = b = 1 = x/3$.

In the current work, we calculate the BPVE of three ternary compounds that meet these criteria: LiAsX_2 (X = S, Se) and $NaAsSe_2$. All three have been synthesized in polar monoclinic space groups: Cc for the first two and Pc for the third.[16] As well, all three compounds have been documented as having experimental band gaps well within the visible spectrum: 1.60 eV for $LiAsS_2$, 1.11 eV for $LiAsSe_2$, and 1.75 eV for $NaAsSe_2$.[16] These compounds are distinguished by their one dimensional infinite As-X chains, as shown in Figure 4.1. The chains in LiAsX_2 and $NaAsSe_2$ are different. In LiAsX_2, the chain atoms are confined to planes not containing Li, and the Li atoms arrange themselves in a nearly square planar arrangement with the remaining non-chain X atoms. On the other hand, in $NaAsSe_2$, the Na atoms do not form square planar arrangements with Se. The differences in the cation arrangements and the chain are clearly visible in Figure 4.1. Additional chain descriptions are detailed in Bera *et al.*[16] A final difference between the two types of compounds is that the β angles, (between the a and c lattice vectors), in $LiAsS_2$ and $LiAsSe_2$ are 113.12° and 113.21°, while β for $NaAsSe_2$ is 90.45°, making this crystal nearly orthorhombic. In this paper, we report the bulk photovoltaic shift current and Glass coefficient of these materials.

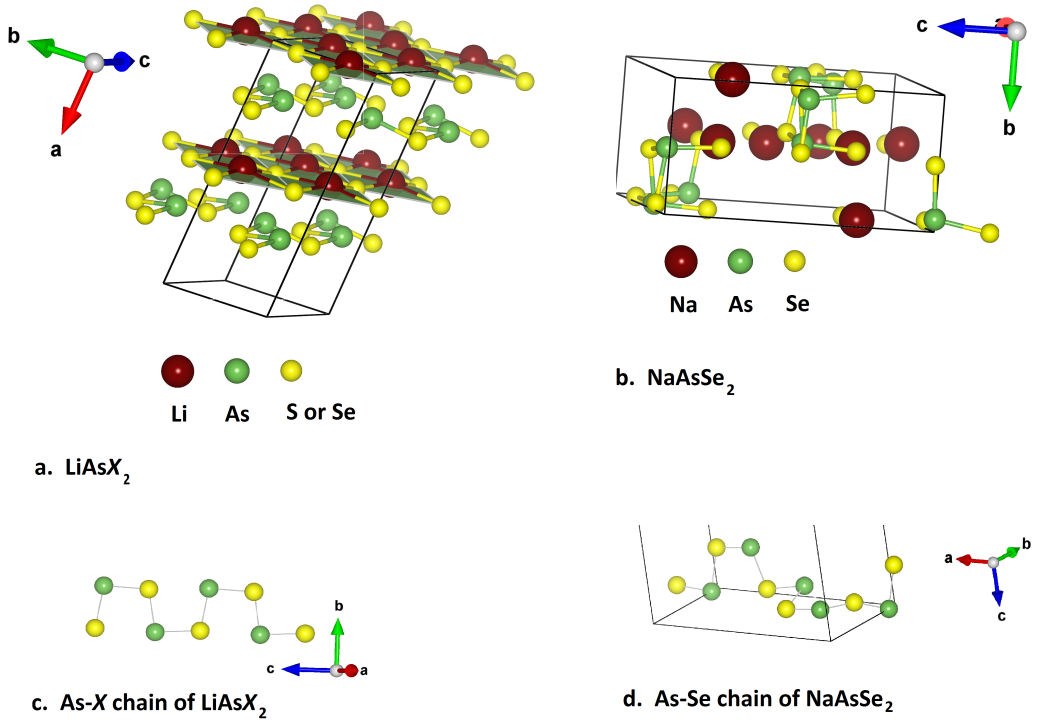

Figure 4.1: Depictions of compounds a) $LiAsS_2$ and $LiAsSe_2$, and b) $NaAsSe_2$. c) As-X chain in LiAsX_2. d) As-Se chain in $NaAsSe_2$. The VESTA graphics software package was used to create these images.[2]

4.3 Methodology.

We use Quantum Espresso[57] to perform density functional theory calculations with the generalized gradient approximation on the three compounds described above. We have found that calculations using experimental geometries, where available, allow for more faithful reproduction of electronic properties. We use the coordinates listed in the FIZ Karlsruhe ICSD database for $LiAsS_2$ and $LiAsSe_2$.[88, 89] The coordinates for $NaAsSe_2$ are taken from the supporting information of Bera *et al.*[16] The results of the SCF calculation are then used to calculate the partial density of states (PDOS) and band structure, and the wavefunctions and energies are also used as inputs for the shift current calculation. We use the nomenclature for the high symmetry points as found in the Bilbao Crystallographic Server to create band diagrams.[90] We use ABINIT to calculate the polarization.[56] Norm-conserving optimized pseudopotentials[58] were created using the OPIUM software package.[59] All calculations use a plane-wave basis set with a 50 Ry plane-wave cutoff.

As explained in detail in References [81, 5, 3] the shift current density is derived using time dependent perturbation theory under a dipole approximation treatment of the classical electromagnetic field. With $\mathbf{J}$ as the current density due to illumination with electric field strength $\mathbf{E}$, the response tensor σ is expressed as:

$$
\begin{aligned}
J_q &= \sigma_{rsq} E_r E_s \\
\sigma_{rsq}(\omega) &= \pi e \left(\frac{e}{m\hbar\omega}\right)^2 \sum_{n',n''} \int d\mathbf{k} \left(f[n''\mathbf{k}] - f[n'\mathbf{k}]\right) \\
&\quad \times \langle n'\mathbf{k}| \hat{P}_r |n''\mathbf{k}\rangle \langle n''\mathbf{k}| s\hat{P}_s |n'\mathbf{k}\rangle \\
&\quad \times \left(-\frac{\partial \phi_{n'n''}(\mathbf{k},\mathbf{k})}{\partial k_q} - [\chi_{n''q}(\mathbf{k}) - \chi_{n'q}(\mathbf{k})]\right) \\
&\quad \times \delta\left(\omega_{n''}(\mathbf{k}) - \omega_{n'}(\mathbf{k}) \pm \omega\right)
\end{aligned} \tag{4.1}
$$

in which n', n'', and $\mathbf{k}$ indicate band index and wavevector, f gives the occupation, $\hbar\omega_n$ is the energy of state n, $\phi_{n',n''}$ is the phase of the momentum matrix element between state n' and n'', and χ_n is the Berry connection for this state.

For the monoclinic space group compounds in this study, the shift current tensor is represented in two-dimensional matrix form as:

$$\sigma = \begin{bmatrix} \sigma_{xxX} & \sigma_{yyX} & \sigma_{zzX} & 0 & \sigma_{xzX} & 0 \\ 0 & 0 & 0 & \sigma_{yzY} & 0 & \sigma_{xyY} \\ \sigma_{xxZ} & \sigma_{yyZ} & \sigma_{zzZ} & 0 & \sigma_{xzZ} & 0 \end{bmatrix} \tag{4.2}$$

When the material is thick enough to absorb all the penetrating light, the Glass coefficient[91] is used to describe the current response, and in the following we report only the terms diagonal in the field, from which the response to unpolarized light of an arbitrary wavevector may be determined. The absorption coefficient enters the Glass coefficient expression as $G_{rrq} = \sigma_{rrq}/\alpha_{rr}$, where α_{rr} is absorption coefficient tensor. The shift current from a thick film can be expressed as:

$$J_q(\omega) = \frac{\sigma_{rrq}(\omega)}{\alpha_{rr}(\omega)} \left| E_r^0(\omega) \right|^2 \mathcal{W} = G_{rrq}(\omega) I_r(\omega) \mathcal{W} \tag{4.3}$$

where $I_r(\omega)$ is intensity and $\mathcal{W}$ is the sample width. Since we are, at present, concerned only with response to unpolarized light, we ignore terms off-diagonal in the electric field, as these cannot contribute to current. To see this, we compute the general response in the Z direction for unpolarized light with wavevector along Y. For arbitrary decomposition of

the unpolarized light we obtain two orthogonal components

$$\mathbf{E}' = E_0 \left[\cos(\theta)\hat{\mathbf{x}} + \sin(\theta)\hat{\mathbf{z}}\right] \text{ and}$$

$$\mathbf{E}'' = E_0 \left[-\sin(\theta)\hat{\mathbf{x}} + \cos(\theta)\hat{\mathbf{z}}\right]$$

The current generated is then

$$\begin{aligned}
J_z =& \left[\sigma_{xxZ} E'_x E'_x + \sigma_{zzZ} E'_z E'_z + 2\sigma_{xzZ} E'_x E'_z\right] + E_0 \left[\sigma_{xxZ} E''_x E''_x + \sigma_{zzZ} E''_z E''_z + 2\sigma_{xzZ} E''_x E''_z\right] \\
J_z =& E_0^2 \left[\sigma_{xxZ} \cos^2(\theta) + \sigma_{zzZ} \sin^2(\theta) + 2\sigma_{xzZ} \cos(\theta)\sin(\theta)\right] + \\
& E_0^2 \left[\sigma_{xxZ} \sin^2(\theta) + \sigma_{zzZ} \cos^2(\theta) - 2\sigma_{xzZ} \sin(\theta)\cos(\theta)\right] \\
J_z =& E_0^2 \left[\sigma_{xxZ} + \sigma_{zzZ}\right]
\end{aligned}$$

Thus, for unpolarized light, elements off-diagonal in the field will give canceling contributions.

4.4 Results and discussion.

Tables 4.1 and 4.2 present the calculated maximum shift current density response and maximum Glass coefficient, as well as the calculated and experimental values for the band gap, for the three compounds, ranked by maximum shift current response. In order to show clearly the maximum responses, we rotate the lattices of the compounds counterclockwise in the $x'z'$-plane. We define γ to be the angle between the c lattice vector and the z-component-aligned polarization of the incoming radiation at which maximum response occurs. These values are also listed in the table. A cartoon of the orientation for LiAsX_2 (X = S, Se) is provided in Figure 4.2. The nearly orthorhombic compound, NaAsSe$_2$, has its maximum shift current response at γ = 0°, while the A = Li compounds, with nearly

identical β angles of 113.12° and 113.25°, obtain maximum shift current response at γ = 11°. $BiFeO_3$ serves as a benchmark having been shown both theoretically and experimentally as having a maximum current density of 5×10^{-4} $(A/m^2)/(W/m^2)$ at 3.3 eV and a maximum Glass coefficient of 5×10^{-9} cm/V at 2.75 eV.[4, 92] Each of the chalcogenide compounds in this study has at least an order of magnitude greater shift current response and Glass coefficient magnitude at least five times larger as well.

Table 4.1: Calculated and experimental band gaps, polarization, and lattice β angle for $LiAsS_2$, $LiAsSe_2$, and $NaAsSe_2$. Values for $BiFeO_3$ are also reported. The experimental band gap values for the chalcogenide compounds are from Bera *et al.*[16]

Compound	Lattice β angle (°)	Band Gap Calculated (eV)	Band Gap Experiment (eV)	Polarization $P_{x'}$ (C/m^2)	Polarization $P_{z'}$ (C/m^2)
$NaAsSe_2$	90.44	1.25	1.75	-0.13	-0.06
$LiAsSe_2$	113.12	0.77	1.11	-0.15	0.06
$LiAsS_2$	113.25	1.07	1.60	-0.18	0.06
$BiFeO_3$	—	2.50[4]	2.67[41]	0	0.90[93]

Table 4.2: Maximum shift current response, relative angle (γ) between the c lattice vector of the compound and z polarization of incoming light at this maximum, and the maximum Glass coefficient at γ for $LiAsS_2$, $LiAsSe_2$, and $NaAsSe_2$. Values for $BiFeO_3$ are also reported.

Compound	Max. Shift Current Density ($\times 10^{-4}$ (A/m^2)/(W/m^2))	γ (°)	Max. Glass Coefficient ($\times 10^{-9}$ cm/V)
$NaAsSe_2$	109	0	-35
$LiAsSe_2$	-98	11	-42
$LiAsS_2$	-49	11	-21
$BiFeO_3$	5[4]	—	5[4]

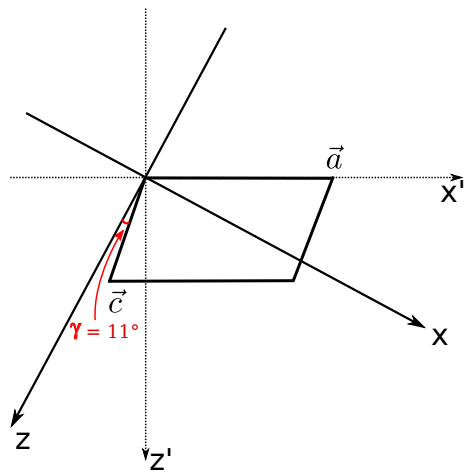

Figure 4.2: Rotation of the $LiAsS_2$/$LiAsSe_2$ crystal in the x′z′ plane relative to incoming light for which the shift current response is a maximum. The lattice vectors $\vec{a}$ and $\vec{c}$ are written in terms of x' and z', while the response and light polarizations are in terms of x and z. The zzZ response is maximized when the z axis is rotated clockwise by $\gamma = 11°$ from $\vec{c}$.

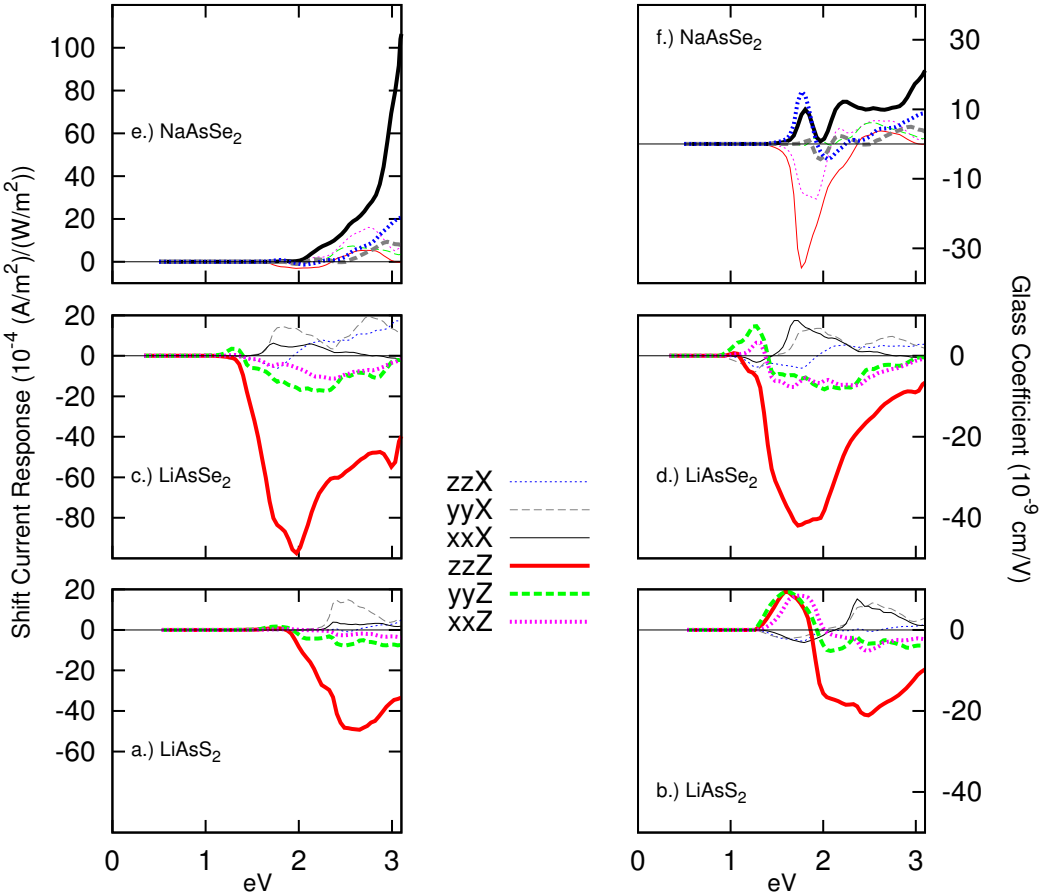

Figure 4.3: Shift current responses and Glass coefficients for $LiAsS_2$, $LiAsSe_2$, and $NaAsSe_2$. The shift current responses are in the left hand column with units of $\times 10^{-4}$ (A/m^2)/(W/m^2) and the Glass coefficient responses are in the right hand column with units of $\times 10^{-9}$ cm/V. The response curves have been adjusted to the right by the difference in the experimental and calculated band gaps. The legend entries are interpreted as follows: zzZ means polarized light from zz direction inducing a current in the Z Cartesian direction.

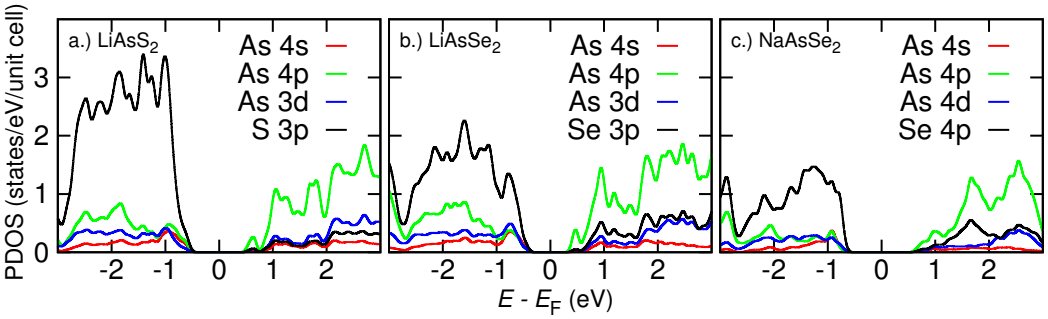

Figure 4.4: PDOS for $LiAsS_2$, $LiAsSe_2$, and $NaAsSe_2$. For uniformity, the PDOS results are all relative to a 16-atom unit cell.

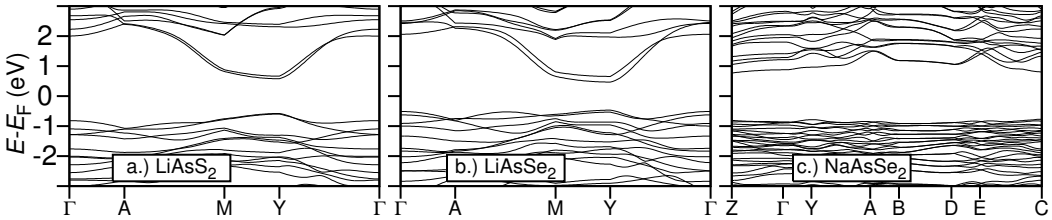

Figure 4.5: Electronic band structures for $LiAsS_2$, $LiAsSe_2$, and $NaAsSe_2$.

The total shift current responses and Glass coefficients are plotted in Figure 4.3 between 0 and 3.1 eV for ABX_2. On each plot, the responses are shifted to the right by the underestimation of the experimental band gap. As depicted, the chalcogenides all show shift current responses for photon energies approximately 1 eV lower than the onset of the response for $BiFeO_3$, due to their smaller band gaps. At all energies below ≈2.9 eV, $LiAsSe_2$ has a superior shift current response and Glass coefficient to $LiAsS_2$ and $NaAsSe_2$. Above ≈2.9 eV, $NaAsSe_2$ has higher responses. The responses are labeled such that the double small letters indicate the direction of the incoming radiation and the capital letter indicates the direction of the induced current. (The reason for the two small letters is that the BPVE is a second-order process in the E field.) With respect to $BiFeO_3$ and its polarization value of 0.9 C/m^2,[93] these data clearly reinforce earlier work showing again that the magnitude of shift current is not simply correlated with magnitude of material polarization.[81]

PDOS results in Figure 4.4 show that in each of the three compounds, the valence band edge down to -3 eV is dominated by S $3p$ or Se $4p$ states, while the conduction band up to 3 eV is dominated by the As $4p$ states. Thus, all electron transitions from the valence to the conduction band are overwhelmingly p - p. Band structures in Figure 4.5 indicate that these three compounds all have direct band gaps. The two compounds with A = Li demonstrate significant dispersion in the conduction band. Given the relative flatness of the conduction and valence bands in the vicinity of the band gap for $NaAsSe_2$, one would expect the other two compounds to have both smaller hole and electron effective masses, and hence higher mobility. Thus, of the three compounds, we would expect $LiAsSe_2$ to produce the most current of the three compounds.

4.5 Conclusions.

We have calculated maximum shift current responses in the visible range, adjusted for theoretical underestimation of experimental band gaps, in the range of 49-109$\times 10^{-4}$ (A/m^2)/(W/m^2) for $LiAsS_2$, $LiAsSe_2$ and $NaAsSe_2$. The maximum shift current response values for $LiAsS_2$, $LiAsSe_2$ and $NaAsSe_2$ represent an order of magnitude improvement in response to visible light in comparison to $BiFeO_3$. Glass coefficient responses are 4 - 8 times greater than that of $BiFeO_3$. With band gaps below 2 eV, these non-perovskite, non-oxide compounds, with smaller polarization magnitudes than other oxide perovskites for which the BPVE has been evaluated, not only offer a higher shift current magnitude response, but capture more of the solar spectrum than $BiFeO_3$ as well.

4.6 Acknowledgments

JAB was supported by the DOE Office of Basic Energy Sciences, under grant DE-FG02-07ER46431. SMY was supported by the AFOSR, under grant FA9550-10-1-0248. FZ was supported by the NSF, under grant DMR11-24696. AMR was supported by the Office of Naval Research, under grant ONR N00014-12-1-1033. Computational support was provided by the HPCMO of the U.S. DOD and NERSC Center of the U.S. DOE.

Chapter 5

The Structural Diversity of ABS$_3$ Compounds with d^0 Electronic Configuration for the B-cation

Reprinted from J. A. Brehm, J. W. Bennett, M. Rutenberg Schoenberg, I. Grinberg,and A. M. Rappe, Journal of Chemical Physics, 140, 224703, 2014.

5.1 Abstract

We use first-principles density functional theory within the local density approximation to ascertain the ground state structure of real and theoretical compounds with the formula ABS$_3$ (A = K, Rb, Cs, Ca, Sr, Ba, Tl, Sn, Pb, and Bi; and B = Sc, Y, Ti, Zr, V, and Nb) under the constraint that B must have a d^0 electronic configuration. Our findings indicate that none of these AB combinations prefer a perovskite ground state with corner-sharing BS$_6$ octahedra, but that they prefer phases with either edge- or face-sharing motifs.

Further, a simple two-dimensional structure field map created from A and B ionic radii provides a neat demarcation between combinations preferring face-sharing versus edge-sharing phases for most of these combinations. We then show that by modifying the common Goldschmidt tolerance factor with a multiplicative term based on the electronegativity difference between A and S, the demarcation between predicted edge-sharing and face-sharing ground state phases is enhanced. We also demonstrate that, by calculating the free energy contribution of phonons, some of these compounds may assume multiple phases as synthesis temperatures are altered, or as ambient temperatures rise or fall.

5.2 Introduction

In a key work, Muller and Roy used the crystal chemistry method of cation-anion coordination to categorize many of the compounds found experimentally in the major ternary structural families A_2BX_4, AB_2X_4, and ABX_3 known at the time of its publication in 1974.[94] In their analysis of ABX_3 compounds, they constructed structure field maps for those compounds with anions X = O, F, and Cl. These maps plot structure as a function of A and B ionic radii and often lead to regions on the diagrams where only certain phases have been realized experimentally. From these maps, the structures for other A and B pairs can be predicted. Absent from their analysis is any structure field map of ABS$_3$ compounds. Indeed, very few of the compounds listed in their ABX_3 section have X = S, and, for those that do, some of these have phases that were reported as not known with certainty ($e.\ g.$ the compounds CaZrS$_3$ and SrZrS$_3$ synthesized by Clearfield[95]).

Since Muller and Roy's work, the number of synthesized ABS$_3$ compounds has increased substantially; these show a distribution of structural motifs that is in stark contrast to their ABO$_3$ analogs. Most ABO$_3$ compounds show networks of corner-sharing BO$_6$ octahedra and are commonly called perovskites. Several form in the ilmenite phase, in which

layers of edge-connected AO_6 octahedra are connected by faces and corners to layers of edge-connected BO_6 octahedra. As well several other ABO_3 do not have any corner-, edge-, or face- sharing designation, but are instead distinguished by BO_3 B = B, C, N, S, Cl, Br, and I anionic complexes. Pyroxenes are also a less common, but still noteworthy, subclass of ABO_3 types, in which BO_4 tetrahedra are corner-connected. Only a couple of ABO_3 have been found in phases with solely face-sharing or edge-sharing BO_6 octahedral motifs. In contrast, ABS_3 compounds are observed with networks of either solely corner-, edge-, or face-sharing BS_6 octahedral motifs. For example, $BaZrS_3$ and $CaZrS_3$ form as corner-sharing perovskites; $PbZrS_3$ and $TlTaS_3$ form the edge-sharing NH_4CdCl_3 phase; and $BaTiS_3$, $BaVS_3$, and $BaNbS_3$ form face-sharing structures. Further, they are not known to form pyroxenes and there are only two instances listed in FIZ Karlsruhe ICSD database in which ABS_3 have anionic complexes with the B mentioned above in ABO_3: $RbBS_3$ and $TlBS_3$.[88, 89] They do not form the layered ilmenite phase either, but there are near stoichiometric compositions of ABS_3 (denoted as misfit sulfides) with sheets of edge-sharing BS_6 octahedra sandwiching incommensurate rock salt-like AS layers. Two examples of misfit layered compounds are $(SnS)_{1.12}TiS_2$ and $(PbS)_{1.18}TiS_2$.

Unlike their ABO_3 analogs, ABS_3 compounds are not neatly classified by the Goldschmidt tolerance factor,[17]

$$t = \frac{r_A + r_X}{\sqrt{2}(r_B + r_X)} \tag{5.1}$$

where the various r represent the ionic radii of the constituent species. A t = 1 indicates ideal packing in the cubic perovskite structure. As shown by Woodward for ABO_3, the corner-sharing perovskite phase is stable for $\approx 0.95 < t < 1.05$, with most octahedral tilts being observed for $t < 1$, and most untilted structures being realized for $t > 1$.[96] Coupled

corner- and face-sharing phases (*e. g.* $SrMnO_3$ and $BaRuO_3$) begin to form when $t > 1.04$, and completely face-sharing phases with no corner-sharing character form when $t > 1.10$ ($e.\ g.$ $BaMnO_3$). The solely edge-sharing phase is rare in ABO_3 according to Goodenough, and he lists just a single case in his extensive review of ABO_3 compounds: $RbNbO_3$ with t = 1.085.[97] The ilmenites form with $t < \approx 0.8$. Except for one or two cases, the pyroxenes and those ABO_3 compounds with BO_3 anionic complexes form with t greater than those of the corner-sharing perovskites. Furthermore, except for a few compounds with B = S or Cl, those compounds with anionic complexes having B = B, C, N, S, or Cl, have t factors strictly greater than those of solely face-sharing structures. However, in the case of ABS_3, just for the compounds listed above, overlapping ranges are obtained: $0.88 < t < 0.95$ for corner-sharing structures, $0.92 < t < 1.01$ for edge-sharing structures, and $0.98 < t < 1.03$ for face-sharing structures.

In the early 1980s, Pettifor developed structure field maps in a different way from Muller and Roy. Instead of using the ionic radii for the abscissa and the ordinate, he defined a chemical scale based on the results of phase groupings of 574 binary compounds.[98] The elements, from hydrogen through the actinides, were scaled in such a manner that the resulting list also mirrored, to a large extent, an ordering of the elements by electronegativity.[99] In 1988, he applied his mapping method to various ternary formula families including ABS_3 compounds.[100] However, unlike the Muller and Roy maps of ABX_3 X=O, F, and Cl, Pettifor's map did not lead to a good demarcation between edge-sharing compounds and corner-sharing ones. Furthermore, if edge-sharing compounds not included in his figure (such as $PbSnS_3$, $BaSnS_3$, $PbZrS_3$, and $SnZrS_3$) are also considered, demarcations between phases of different motifs becomes even more blurred. Finally, the discovery of the stable edge-sharing phase of $SrZrS_3$ by Lee *et al.*[101] in 2005 also diminishes the distinction between edge- and corner-sharing regions of his map.

In the current paper, we investigate the disagreement between t factor expectations and

experimental phase results in ABS$_3$ and develop a methodology for predicting the ground state structures of ABS$_3$ compounds and energetically competitive crystal structures that could be reasonably stabilized. We also calculate the local density approximation (LDA) band gap for the ground state phase and these alternate phases to highlight the structure-property differences.

5.3 Methodology

In order to determine the ground state structural tendencies of ABS$_3$ compounds, we first construct a sample subset of 20 compounds. The A-sites considered are the Group 1 elements K, Rb, and Cs, the Group 2 elements Ca, Sr, and Ba, the Group 13 element Tl, the Group 14 elements Sn and Pb, and the Group 15 element Bi. To focus the study, Period 4 and 5 B-site cations are chosen such that the electron configuration is d^0: Sc, Y, Ti, Zr, V, and Nb. While no combinations of Group 1 or Tl A-sites for ABS$_3$ are known to exist, (except for TlTaS$_3$ with Ta outside the scope of this study), they are considered as interesting extensions to various BaBS$_3$ that do exist: all are as large or larger than Ba^{2+} in 12-fold coordination. Further, ABX_3 oxides and halides with A = K, Rb, and Cs do exist. For each of these compounds, we then arrange the atoms into 22 phases that ABX_3 compounds are known to assume. Then, using density functional theory (DFT) within the LDA approximation, we calculate the relative energy of each phase with the ABINIT computing package.[56]

The set of 22 phases chosen includes the most common experimentally found corner-, edge-, and face-sharing BX_6 octahedral structures. The corner-sharing arrangements chosen are the cubic $Pm3m$, the tetragonal $P4mm$, the low temperature $R3mR$ BaTiO$_3$ phase and two tilt systems denoted by Glazer's naming scheme:[64] the common $a^+b^-b^-$ $Pnma$ and the low temperature $a^0a^0c^-$ $I4/mcm$ of SrTiO$_3$.

For edge-sharing systems, we consider four phases. The first, the commonly found NH_4CdCl_3 $Pnma$ phase, has as its defining pattern double columns of edge-sharing BS_6 octahedra, with each octahedron sharing edges with four others. The second is the $Pna2_1$ phase, which differs from this first phase in that atoms are displaced from high symmetry positions preserving a screw axis symmetry along the direction of the columns. The third edge-sharing phase is similar to the second, but displacements of atoms in the plane perpendicular to the screw axis are permitted. This phase is well known for the family of $YScS_3$ $Pna2_1$ structures, a group of compounds with lanthanide element A sites in which the edge-sharing occurs for AS_6 prisms and the BS_6 are corner-connected. In order to distinguish between these two phases, we term them E_Pna2_1 and C_Pna2_1 respectively, with the E (edge) and C (corner) indicating the connectivity of the BS_6 octahedra. The remaining edge-sharing phase is a very low symmetry $P1$ phase found for $RbNbO_3$.

Four of the face-sharing phases we consider are based on the research of Fagot *et al.* and Ghedira *et al.*:[102, 103] the $Cmcm$, the $C222_1$, the $Cmc2_1$, and the $P6_3/mmc$. Like all face-sharing phases, they have separated single columns of face-sharing octahedra. The first three have an orthorhombic lattice. $Cmcm$ has B cations occupying high symmetry coordinates (0 and 0.5) in all three Cartesian directions leading to collinear B cations in the columnar direction; in $C222_1$, the B cations are non-collinear and zigzag about one of the directions perpendicular to the columns; and in $Cmc2_1$, the B cations zigzag in both directions perpendicular to the columns. The $P6_3/mmc$ phase is similar to the $Cmcm$ phase in that both have two mirror planes and one glide plane. They differ in that $Cmcm$ is an orthorhombic crystal system with a base-centered Bravais lattice, while $P6_3/mmc$ is a hexagonal crystal system with a simple Bravais lattice. $P6_3/mmc$ is classified as a minimal non-isomorphic subgroup of $Cmcm$. Two other hexagonal face-sharing phases, the $P6_3cm$ and $P6_3mc$, are also evaluated. $P6_3mc$ differs from $P6_3/mmc$ in that the former allows B cation shifts from high symmetry positions in the column direction. For the $P6_3cm$ phase,

there are two distinct sets of columns of face-sharing octahedra which are offset by a 1/4 unit vector in the column direction. Thus, in total, six face-sharing phases are evaluated.

The remaining seven phases considered are either one of three types of mixed motif phases, or a corner-sharing tetrahedral phase. Three mixed motif face-sharing and corner-sharing phases are evaluated in this study and are labelled based on the fraction of face-sharing octahedra per unit cell as $2/3$, $1/2$, and $1/3$. They are most easily visualized by considering their projections on the (110) plane: the first consists of stacks of three face-sharing octahedra joined at a corner; the second consists of stacks of two face-sharing octahedra joined at a corner; and the third consists of alternating stacks of two face-sharing octahedra sharing a corner with a single octahedron. Respectively, these phases are known by their structure type names as $BaRuO_3$, $BaMnO_3$, and $BaFeO_{2+x}$. A second type of mixed motif phase, one with mixed edge- and corner-sharing connectivity, is also considered. The $Cmcm$ phase of the compound $CaIrO_3$, (which is proposed to exist under high pressures for $MgSiO_3$),[104] and its subgroup $Cmc2_1$, (in which atoms are no longer confined to high symmetry positions along the z-axis),[105] have this motif and are respectively designated MM_Cmcm and MM_Cmc2_1, with MM signifying "mixed motif". This phase is characterized by planes of BS_6 octahedra, in which the octahedra are connected by edges in one direction in the plane, and by corners in the other planar direction. The last mixed motif phase considered is the ilmenite. This phase, most often characterized by small A and B d-metal elements in ABO_3, has alternating layers of edge-sharing AO_6 octahedra and edge-sharing BO_6 octahedra. The layers are connected by both face- and corner- sharing octahedra. This phase is designated MM_Ilmen. Finally, a pyroxene $Pbcm$ phase consisting of single columns of zig-zag corner-sharing tetrahedra is included, as all compounds with the AVO_3 (A = K, Rb, Cs, and Tl) chemical formula assume this structure.

The elements used in the study are represented in the DFT calculations by non-local,[30] norm-conserving optimized pseudopotentials[58] created with OPIUM.[59] The plane wave

cutoff energy used for both the pseudopotentials and the DFT calculations is 50 Ry. We vary the Monkhorst-Pack (MP) grid[60] depending on the size of the unit cell. A k-point mesh of 16 is used along the reciprocal lattice directions for which the lattice parameter is ≈5 Å; 8 if it is ≈10 Å, and 4 if it is ≈20 Å. All hexagonal phases use grid shifts of 0×0×0.5; all others incorporate a shift of 0.5×0.5×0.5. Where an LDA band gap calculation is required on a relaxed structure for a particular compound, an unshifted MP grid is used. We consider a structure to be relaxed when successive self-consistent iterations yield total energy differences of less than 10^{-8} Ha/unit cell and and atomic forces less than 10^{-4} Ha/Bohr.

For each of the lowest energy phases of the 20 compounds, and for those phases nearest to them in terms of relative energy, we obtain the entropy contribution to the free energy and assess compound stability by calculating the phonon normal mode frequencies at the Γ-point and then using the equation:

$$F_{\text{vib,solid}} = \sum_{s=1}^{3N} \left\{ \frac{\hbar\omega_s}{2} + k_B T \ln\Big[1 - \exp\Big(\frac{-\hbar\omega_s}{k_B T}\Big)\Big] \right\} \tag{5.2}$$

where N represents the number of atoms in the system, ω_s represents a Γ-point normal mode frequency in the harmonic approximation, k_B is the Boltzmann constant, and T is temperature.

For the full set of 20 A-B combinations, we develop two structure field maps to elucidate sulfide structural preferences with respect to A and B cation sizes: one following the method of Pettifor; the other the method of Muller and Roy. In the case of the Muller and Roy type map, we combine the originally separated field maps for $A^{1+}B^{5+}X_3$, $A^{2+}B^{4+}X_3$, and $A^{3+}B^{3+}X_3$ into one plot for brevity. For all ionic sizes, except Sn^{2+}, we use the data found in Seshadri[61] and Shannon.[106] We use the value of 1.4 Å for the ionic radius

for Sn^{2+} which was calculated by Bennett *et al.*[107] We use 12-fold coordination radii for A, and six-fold coordination radii for B and S. Using these radii, we then reassess the Goldschmidt t factor in light of the preferred phases found.

5.4 Results

The calculated ground state phases for the 20 ABS$_3$ compounds are plotted on the Muller and Roy ionic radii type structure field map in Figure 5.1 and the Pettifor type structure field map in Figure 5.2. With the exceptions of two A = Tl based compounds, the Muller and Roy type map demonstrates a well-defined demarcation between the face-sharing and edge-sharing ground state structures. As with the ABO$_3$ structure maps of Muller and Roy, the face-sharing ground state phase is found only in the regions of large r_A and small r_B. Significantly, no pure corner-sharing perovskite is calculated to be the ground state phase. Only the predicted ground state of the mixed motif corner- and edge-sharing MM_Cmc2_1 phase for CaZrS$_3$ has any corner-sharing character. Even for this compound, the pure edge-sharing phase is slightly favored over the pure corner-sharing phase by 0.007 eV/20-atom unit cell. The Pettifor map improves on the Muller and Roy type map in the sense that plotting the ground state structure in the Pettifor map leads to no overlap between the face- and edge-sharing ground state structures. However, in the Pettifor map (Figure 5.2) the mixed motif corner- and edge-sharing CaZrS$_3$ falls within the edge-sharing region.

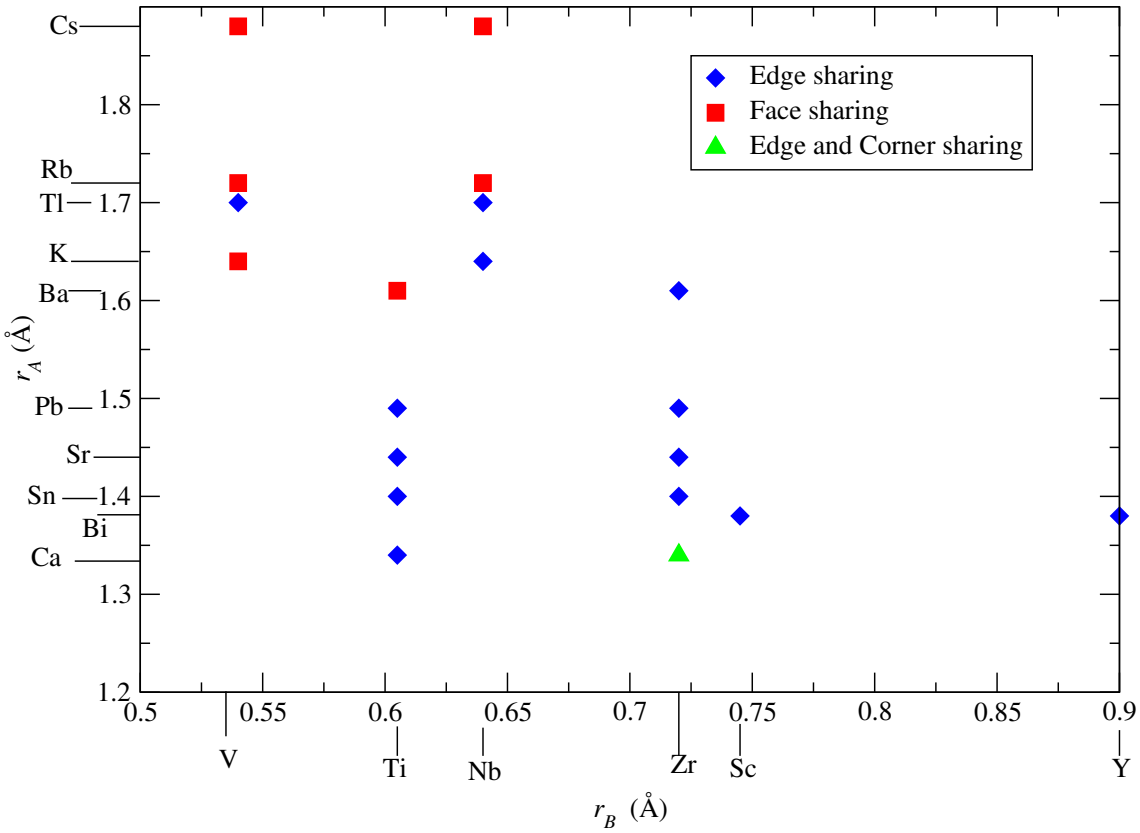

Figure 5.1: Structure field map of ground state $AB\mathrm{S}_3$ structures with various $B\mathrm{S}_6$ octahedral motifs. All r_A assume a coordination number of 12; all r_B assume a six-fold coordination. [Reprinted from J. A. Brehm, J. W. Bennett, M. Rutenberg Schoenberg, I. Grinberg,and A. M. Rappe, Journal of Chemical Physics, 140, 224703, 2014. Copyright 2014 by the American Institute of Physics.]

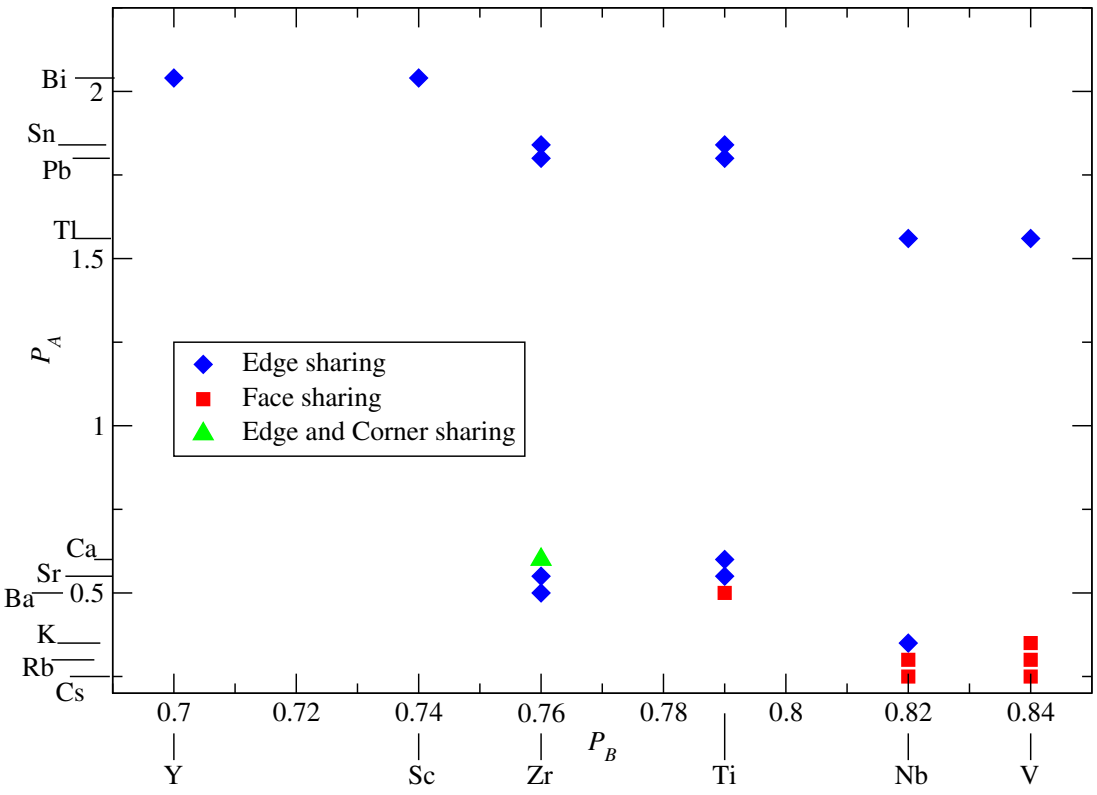

Figure 5.2: Pettifor chemical scale structure field map of ground state $AB\mathrm{S}_3$ structures with various $B\mathrm{S}_6$ octahedral motifs. P_A and P_B represent the values of the scale assigned to each element. The value assigned to each element approximates its electronegativity. Further details as to the construction of this scale can be found in [99]. [Reprinted from J. A. Brehm, J. W. Bennett, M. Rutenberg Schoenberg, I. Grinberg,and A. M. Rappe, Journal of Chemical Physics, 140, 224703, 2014. Copyright 2014 by the American Institute of Physics.]

Tables 5.1 - 5.4 rank, for each compound, the lowest energy phases by motif as obtained by DFT where E_{DFT} = $H(T$ = 0 K). The phonon assessment at the Γ-point shows that, except for three compounds, (ANbS$_3$ A = K, Rb, and Tl), all of the ground state phases are stable with respect to relaxations within the designated space groups. For the three cases where stability within the designated space groups was not established, we lifted the space group restriction and perturbed coordinates to obtain relaxed structures that were evaluated as stable. These were slightly lower in energy by at most 0.009 eV/20-atom unit cell as compared to the higher symmetry structure. These lower symmetry structures maintain the same motif as their higher symmetry parent structures. Addition of zero-point energies (ZPE) to E_{DFT} does not change the rankings. The T_{trans} column indicates the temperature at which the ground state compound and another listed compound have the same free energies as a result of vibrational entropy differences. For many of these phase transitions, the LDA calculated band gaps for the different phases are significantly different, as can be seen for the compounds with A = Ba and B = Ti and Zr.

Table 5.1: Ranking of phases by ΔE, the total energy per 20-atom cell for the five ABS$_3$ B = Ti compounds described in the text. In addition to the ground state energy phase, phases with different BS$_6$ motifs are also presented if they are within ≈1 eV per 20-atom cell of the ground state. C = corner-sharing, E = edge-sharing, E/C = edge- and corner-sharing, and F = face-sharing. The number in the parentheses of the ΔE column is the difference in energy when the zero point of energy (ZPE) obtained from the phonon calculation is included. Structures that were found to be unstable due to negative phonon frequencies at the Γ-point are indicated with NP. The T_{trans} column indicates the temperature at which the different structures have the same free energy relative to the ground state, and the system is predicted to undergo a phase transition. For some phases, there is no transition temperature, labelled NT. LDA band gaps (E_g) are listed and labeled with an I/D = indirect/direct. Please refer to the Methodology Section for space group nomenclature. [Reprinted from J. A. Brehm, J. W. Bennett, M. Rutenberg Schoenberg, I. Grinberg,and A. M. Rappe, Journal of Chemical Physics, 140, 224703, 2014. Copyright 2014 by the American Institute of Physics.]

A	Motif (Sp. Grp.)	ΔE (+ZPE) (eV/unit cell)	T_{trans} (K)	E_g (eV)
		$A^{2+}B^{4+}$		
		Ti		
Sn	E($Pnma$)	0 (0)		0
	E/C (MM_Cmcm)	0 (NP)	——	0
	C ($Pnma$)	0.87 (0.84)	NT	0
Pb	E ($Pnma$)	0 (0)		0.16 (D)
	E/C (MM_Cmcm)	0.26 (0.23)	1150	0
	C ($Pnma$)	0.56 (0.55)	NT	0
	F/E/C(MM_Ilmen))	0.76 (0.79)	>4000	0.32 (I)
Ca	E ($Pna2_1$)	0 (0)		0
	E/C (MM_Cmc2_1)	0.11 (0.09)	305	0
	C ($Pnma$)	0.16 (NP)	——	0.14 (D)
Sr	E ($Pna2_1$)	0 (0)		0.15 (I)
	C ($Pna2_1$)	0.37 (0.38)	NT	0.54 (D)
	E/C (MM_Cmc2_1)	0.51 (0.50)	NT	0
Ba	F ($C222_1$)	0 (0)		0
	C ($Pna2_1$)	0.60 (0.57)	NT	0.38 (D)
	E ($Pna2_1$)	0.92 (0.93)	NT	0.41 (I)

Table 5.2: Ranking of phases by ΔE, the total energy per 20-atom cell for the five ABS$_3$ B = Zr compounds described in the text. The information below is described in the caption of Table 5.1. [Reprinted from J. A. Brehm, J. W. Bennett, M. Rutenberg Schoenberg, I. Grinberg,and A. M. Rappe, Journal of Chemical Physics, 140, 224703, 2014. Copyright 2014 by the American Institute of Physics.]

A	Motif (Sp. Grp.)	ΔE (+ZPE) (eV/unit cell)	T_{trans} (K)	E_g (eV)
		$A^{2+}B^{4+}$		
		Zr		
Sn	E ($Pnma$)	0 (0)		0.65 (D)
	E/C (MM_Cmc2_1)	0.54 (0.49)	1075	0.55 (I)
	C ($Pnma$)	1.03 (0.97)	2475	0.24 (D)
Pb	E ($Pnma$)	0 (0)		0.88 (D)
	E/C (MM_Cmcm)	0.167 (NP)	——	0.76 (D)
	C ($Pnma$)	0.48 (0.44)	2180	0.53 (I)
	F/E/C(MM_Ilmen))	0.90 (0.89)	3750	0.65 (I)
Ca	E/C (MM_Cmc2_1)	0 (0)		0.10 (D)
	E ($Pnma$)	0.23 (0.24)	NT	0.27 (D)
	C ($Pnma$)	0.23 (0.25)	NT	0.96 (D)
	F/E/C(MM_Ilmen))	0.85 (0.89)	NT	1.67 (I)
Sr	E ($Pnma$)	0 (0)		0.24 (D)
	E/C (MM_Cmc2_1)	0.16 (0.14)	1100	0.23 (D)
	C ($Pnma$)	0.29 (0.27)	2050	0.96 (D)
Ba	E ($Pnma$)	0 (0)		0.50 (D)
	C ($Pnma$)	0.05 (0.01)	90	0.74 (D)
	E/C (MM_Cmcm)	0.49 (0.47)	2050	0.32 (D)

Table 5.3: Ranking of phases by ΔE, the total energy per 20-atom cell for the five ABS$_3$ B = V and Sc compounds described in the text. The information below is described in the caption of Table 5.1. [Reprinted from J. A. Brehm, J. W. Bennett, M. Rutenberg Schoenberg, I. Grinberg,and A. M. Rappe, Journal of Chemical Physics, 140, 224703, 2014. Copyright 2014 by the American Institute of Physics.]

A	Motif (Sp. Grp.)	ΔE (+ZPE) (eV/unit cell)	T_{trans} (K)	E_g (eV)
		$A^{1+}B^{5+}$		
		V		
K	F ($C222_1$)	0 (0)		0
	C ($Pna2_1$)	0.23 (0.27)	NT	0
	E ($Pna2_1$)	1.34 (1.31)	>4000	0.20 (I)
Rb	F ($C222_1$)	0 (0)		0
Cs	F ($C222_1$)	0 (0)		0
	E ($P1$)	1.23 (1.26)	>4000	0
Tl	E ($Pna2_1$)	0 (0)		0
	F ($C222_1$)	0.12 (0.16)	1780	0
	E/C (MM_Cmc2_1)	0.46 (0.46)	NT	0
	F/E/C(MM_Ilmen)	0.84 (0.82)	>4000	0.07 (I)
		$A^{3+}B^{3+}$		
		Sc		
Bi	E ($Pnma$)	0 (0)		1.23 (I)
	C ($Pnma$)	0.11 (NP)	—	1.36 (D)
	E/C (MM_Cmc2_1)	0.38 (0.35)	1120	1.43 (I)
	F/E/C(MM_Ilmen)	0.84 (0.82)	2800	1.18 (I)

Table 5.4: Ranking of phases by ΔE, the total energy per 20-atom cell for the five ABS$_3$ B = Nb and Y compounds described in the text. The information below is described in the caption of Table 5.1. [Reprinted from J. A. Brehm, J. W. Bennett, M. Rutenberg Schoenberg, I. Grinberg,and A. M. Rappe, Journal of Chemical Physics, 140, 224703, 2014. Copyright 2014 by the American Institute of Physics.]

A	Motif (Sp. Grp.)	ΔE (+ZPE) (eV/unit cell)	T_{trans} (K)	E_g (eV)
		$A^{1+}B^{5+}$		
		Nb		
K	E ($Sp.Grp.14$)	0 (0)		0.52 (I)
	F ($C222_1$)	0.31 (NP)	——	0
	C ($Pna2_1$)	0.47 (0.52)	NT	0
	F/E/C(MM_Ilmen)	0.54 (0.60)	NT	1.05 (I)
Rb	F ($Sp.Grp.4$)	0 (0)		0
	E ($Pna2_1$)	0.26 (0.40)	3010	0.50 (I)
	F/E/C(MM_Ilmen)	0.60 (0.61)	2680	0.89 (I)
Cs	F ($Cmc2_1$)	0 (0)		0.14 (D)
	E ($Pna2_1$)	0.83 (0.80)	NT	0.61 (I)
	F/E/C(MM_Ilmen)	0.91 (0.92)	>4000	0.64 (I)
Tl	E ($Sp.Grp.14$)	0 (0)		0.01
	E/C (MM_Cmc2_1)	0.44 (0.44)	1960	0
	F ($Cmc2_1$)	1.26 (1.28)	3475	0
	F/E/C(MM_Ilmen)	1.05 (NP)		0.36 (I)
		$A^{3+}B^{3+}$		
		Y		
Bi	E ($Pnma$)	0 (0)		1.26 (I)
	C ($Pna2_1$)	0.41 (0.39)	>4000	1.72 (I)
	E/C (MM_Cmc2_1)	0.42 (0.40)	1420	1.78 (I)
	F/E/C(MM_Ilmen)	0.50 (0.48)	2275	1.49 (I)

As shown in Tables 5.1 - 5.4, for those compounds which favor the edge-sharing ground state motif, none preferred the $P1$ phase. Of particular note, the mixed corner- and edge-sharing phase is often found to have a relative energy between the lowest energy edge-sharing phase and the purely corner-sharing phase, perhaps hinting at a transition path between these two motifs. For those compounds which prefer the face-sharing ground state motif, all prefer one of the two orthorhombic phases, $C222_1$ or $Cmc2_1$, over the hexagonal phases, excepting the low symmetry phase for $RbNbS_3$ which is monoclinic with one unit cell angle equal to 90.67°. As well, of the compounds that prefer the face-sharing motif, only $BaTiS_3$ has the mixed motif face- and corner-sharing phases within 1 eV/20-atom unit cell of the ground state phase. Indeed, $BaTiS_3$ has the most phases within 1 eV/20-atom unit cell of the ground state. An expanded view of its phases is shown in Table 5.5. No other compound has the corner-sharing octahedral $P4mm$, $Pm3m$, and $R3mR$ phases within 1 eV/20-atom unit cell of the ground state. Finally, absent from Tables 5.1 - 5.4 is the corner-sharing tetrahedral $Pbcm$ phase. All compounds evaluated in this phase had energies > 1 eV/20-atom unit cell relative to the ground state.

Table 5.5: Expanded view of the phases of $BaTiS_3$. All energies are with respect to a 20-atom unit cell, which is the number of atoms in the unit cell of the ground state, $C222_1$. NA = phonon frequency/stability not attempted. All other nomenclature as in Table 5.1. [Reprinted from J. A. Brehm, J. W. Bennett, M. Rutenberg Schoenberg, I. Grinberg,and A. M. Rappe, Journal of Chemical Physics, 140, 224703, 2014. Copyright 2014 by the American Institute of Physics.]

Motif (Sp. Grp.)	ΔE (+ZPE) (eV/20-atom unit cell)	T_{trans} (°K)	E_g (eV)
F ($C222_1$)	0.00 (0)		0
F ($Cmc2_1$)	0.01 (NP)	—	0
F ($P6_3cm$)	0.12 (NP)	—	0
F ($P6_3mc$)	0.20 (NP)	—	0
F ($P6_3/mmc$)	0.22 (NP)	—	0
F ($Cmcm$)	0.02 (NP)	—	0
F/C ($2/3$)	0.37 (NA)	—	0
F/C ($1/2$)	0.37 (NA)	—	0
F/C ($1/3$)	0.50 (NA)	—	0
C ($Pna2_1$)	0.59 (0.57)	NT	0.38 (D)
C ($Pnma$)	0.65 (NP)	—	0
C($R3mR$)	0.75 (0.46)	340	0
C ($Pm3m$)	0.75 (0.47)	340	0
C ($P4mm$)	0.80 (0.51)	375	0
E ($Pna2_1$)	0.92 (0.93)	NT	0.41 (I)
E ($Pnma$)	0.95 (NP)	—	0.23 (I)

In Table 5.6, the standard t for the set of 20 compounds used in this study is computed, ranked, and compared to the ground state structural motif. As can be seen from Table 5.6, there are no overlapping regions of t values for edge- and corner-sharing compounds, simply because there are no compounds which have been calculated to have a corner-sharing ground state. With the exception of the Tl-based materials, the ground state face- and edge-sharing phases can also be predicted using the standard t factor. We also define the "Pettifor factor", $Pet_{A/B}$ = P_A/P_B, which we define as the ratio of the Pettifor's chemical scale values for A and B and rank the data accordingly. In this scenario, the A = Tl compounds are no longer out of line. Moreover, for the set of compounds chosen for this study, there is a very strong correlation between P_A and the ranking of the compounds by $Pet_{A/B}$. As mentioned in the Introduction, the standard t factor yields overlapping regions of edge- and corner-sharing compounds while the Pettifor chemical scales yields multiple regions of edge- and corner-sharing compounds. The reason ours do not is that existing materials, which have been synthesized at high temperature, are not always created in the ground state, unlike our DFT calculations which determine the ground-state energy at T = 0 K, as will be discussed in the next section.

Table 5.6: Ranking of compounds by the standard Goldschmidt factor, t, the ratio of the Pettifor chemical scale values for A and B, termed here $Pet_{A/B}$, and a modified t', where $t' = t\Delta\chi(\text{S-}A)/\Delta\chi(\text{O-}A)$. χ represents the Pauling electronegativity. P_A represents the Pettifor chemical scale value for A. [Reprinted from J. A. Brehm, J. W. Bennett, M. Rutenberg Schoenberg, I. Grinberg,and A. M. Rappe, Journal of Chemical Physics, 140, 224703, 2014. Copyright 2014 by the American Institute of Physics.]

A	B	t	Motif	A	P_A	B	$Pet_{A/B}$	Motif	A	B	t'	Motif
Bi	Y	0.831	E	Bi	2.04	Y	0.343	E	Pb	Zr	0.207	E
Ca	Zr	0.878	EC	Bi		Sc	0.363	E	Pb	Ti	0.217	E
Bi	Sc	0.881	E	Sn	1.84	Zr	0.413	E	Bi	Y	0.328	E
Sn	Zr	0.884	E	Pb	1.80	Zr	0.422	E	Bi	Sc	0.347	E
Sr	Zr	0.906	E	Sn	1.84	Ti	0.429	E	Sn	Zr	0.370	E
Ca	Ti	0.920	E	Pb	1.80	Ti	0.439	E	Sn	Ti	0.388	E
Pb	Zr	0.920	E	Tl	1.56	Nb	0.526	E	Tl	Nb	0.532	E
Sn	Ti	0.925	E	Tl		V	0.538	E	Tl	V	0.555	E
Sr	Ti	0.949	E	Ca	0.60	Zr	1.267	EC	Ca	Zr	0.569	EC
Ba	Zr	0.953	E	Ca		Ti	1.317	E	Sr	Zr	0.593	E
Pb	Ti	0.963	E	Sr	0.55	Zr	1.382	E	Ca	Ti	0.596	E
K	Nb	0.992	E	Sr		Ti	1.436	E	Sr	Ti	0.621	E
Ba	Ti	0.998	F	Ba	0.50	Zr	1.520	E	Ba	Zr	0.632	E
Tl	Nb	1.009	E	Ba		Ti	1.580	F	Ba	Ti	0.661	F
Rb	Nb	1.015	F	K	0.35	Nb	2.343	E	K	Nb	0.667	E
K	V	1.034	F	K		V	2.400	F	Rb	Nb	0.682	F
Tl	V	1.052	E	Rb	0.30	Nb	2.733	F	K	V	0.695	F
Rb	V	1.058	F	Rb		V	2.800	F	Rb	V	0.711	F
Cs	Nb	1.061	F	Cs	0.25	Nb	3.280	F	Cs	Nb	0.716	F
Cs	V	1.105	F	Cs		V	3.360	F	Cs	V	0.747	F

The predictive ability of the tolerance factor can be further enhanced by taking electronegativity into account in a manner similar to Pearson,[108] and specifying a new generalized t factor, $t' = t\Delta\chi(X\text{-}A)/\Delta\chi(\text{O-}A)$, where $\Delta\chi(X\text{-}A)$ is the electronegativity difference between X = (S, O) and A, and $\Delta\chi(\text{O-}A)$ is the electronegativity difference between O and A. This results in a ranking of the compounds found in the right side of Table 5.6. The same ranking would also be found if the denominator of the ratio, $\Delta\chi(\text{O-}A)$, was not included in the formula. However, by including it, t' remains equivalent to the original t for oxides. A formulation of t' with a denominator of the ratio set to $\Delta\chi(\text{F-}A)$, would lead to the same ranking again, but now be based on the absolute ranking of electronegativity of the elements in which F has the most negative value. This formulation would be more in the spirit of Pettifor's chemical scale, but it would lose the transferability back to the historic t factor values. Along these same lines, the $\sqrt{2}$ geometric factor in t is not needed to produce the rankings for either t or t', and it loses its significance in phases that have edge-, face-, and mixed-sharing motifs. As with all t factors,[109] the t' construct is not perfect, as now the ranking of face-sharing $BaTiS_3$ and edge-sharing $KNbS_3$ with respect to t' is reversed (but only by 0.006 units).

5.5 Discussion

Several of the 20 compounds considered in our study have been found experimentally to be in a different structural motif phase than the one we calculated as the ground state phase ($BaTiS_3$, $A$$ZrS_3$ with A = Ca, Ba, and the misfit $A$$TiS_3$ with A = Sn, Pb, and Sr) and others have not yet been synthesized (all $A^{1+}B^{5+}S_3$ and $A^{3+}B^{3+}S_3$). Nevertheless, there is experimental evidence that supports our results, specifically that face-sharing ground state phases have been attained for large A and small B cations, as well as the preponderance of edge-sharing ground state phases for all other AB combinations.

Our calculations show that the ground state phase of four out of the five B = Zr compounds in this study is the edge-sharing NH_4CdCl_3 $Pnma$ phase. Only the $CaZrS_3$ ground state is different, being of mixed edge- and corner-sharing motif and, even in this case, the next higher energy state is predicted to be the edge-sharing NH_4CdCl_3 $Pnma$ phase as well. All five of these compounds have been synthesized: two in the edge-sharing $Pnma$ phase ($PbZrS_3$ and $SnZrS_3$),[110-112] two in the corner-sharing $Pnma$ phase ($CaZrS_3$ and $BaZrS_3$),[79, 95] and one in both phases ($SrZrS_3$).[101] Prior theoretical calculations have also shown that the NH_4CdCl_3 $Pnma$ phase is the lowest energy perovskite phase for $BaZrS_3$.[113] Lelieveld *et al.* and Clearfield have also synthesized $SrZrS_3$, but only in the edge-sharing phase.[79, 95]

Our predictions of phase transformations due to small energy differences between the phases provide the insight into the discrepancies between the $SrZrS_3$ results of Lelieveld *et al.*[79] and Clearfield[95] on the one hand and Lee *et al.*[101] on the other hand. In 2005, Lee *et al.* synthesized edge-sharing $SrZrS_3$ by mixing the constituent elements together in stoichiometric proportions and then heating at 1120 K. Performing the same procedures at 1220 K led to the creation of a two-phase material with a major corner-sharing phase and a minor edge-sharing phase.[101] In 1980, Lelieveld *et al.* flowed H_2S gas over mixtures of binary oxides at 1370 K to create a solely corner-sharing perovskite.[79] Thus, it is probably the differences in processing temperatures and starting materials that led to the different results between these two experiments. Interestingly, in 1963, Clearfield explored the effect of temperature on the synthesis of $BaZrS_3$, $SrZrS_3$, and $CaZrS_3$ in a manner similar to that of Lelieveld *et al.* In Clearfield's method, he first combined binary oxides to form $AZrO_3$, then used CS_2 gas to replace O with S. He discovered that for synthesis temperatures between 1020 - 1270 K, an unknown phase of $BaZrS_3$ was present in sizable amounts (10-15% composition of the product); and, for all three, at temperatures below 1270 K, found it impossible to state the space group with certainty.[95] Based on the work

of Lee *et al.*, we suggest that it is possible that Clearfield obtained both the corner- and edge-sharing structures within each composition.

In our theoretical study, we show that for $SrZrS_3$ the corner-sharing phase is preferred at temperatures above 2050 K. With respect to Lee's results, our transition temperature at which the corner-sharing phase is preferred over the edge-sharing phase is approximately 900 K too high. Though we do calculate a phase change near 1200 K, it is for a change to a mixed motif corner- and edge-sharing one, and not a completely corner-sharing phase. Thus, as our calculation method involves only harmonic Γ-point phonon contributions to energy, our errors can be attributed to not including full Brillouin zone averaging and anharmonic energy contributions. For $PbZrS_3$ and $SnZrS_3$, the phase changes from edge-sharing to corner-sharing have similar crossover temperatures to $SrZrS_3$. As they have been synthesized as edge-sharing phases at 1070 K,[110-112] our study suggests that they can also be made as corner-sharing phases by synthesizing at higher temperatures.

For $BaZrS_3$, we calculate that the edge-sharing phase is energetically preferred below 90 K. As temperatures in the vicinity of 90 K are too low for synthesis, it would seem that, by itself, a change in synthesis temperature will not lead to the formation of the edge-sharing phase. While $CaZrS_3$ has only been made in the corner-sharing phase, we have shown that this phase is not energetically preferred over the edge-sharing phase or the mixed motif phase at any temperature. Therefore, it should be possible to achieve these other phases of $CaZrS_3$ through either lower synthesis temperatures alone or in combination with other changes in synthesis procedures such as increased pressure. Supporting this idea is the existence of another ABX_3 compound with A = Ca, $CaIrO_3$, which is created in the mixed edge- and corner-sharing phase through the use of elevated pressures.[105]

Next, we compare our theoretical space group and structure predictions of stoichiometric ternary sulfides in which the A cations have a lone pair electron configuration, (and with B not equal to Zr), with experimental literature for those systems where non-stoichiometric

phases are reported. For ABS$_3$ with A cations that possess a lone pair, (Pb, Sn, and Bi), the nonstoichiometric phases are chiefly composed of single sheets of edge-sharing BS$_6$ octahedra with a chemical formula of BS$_2$ separated by single or multiple planes of distorted rock salt AS.[114] An important point of agreement is that our calculations also predict an edge-sharing structure for each of these. However, the stoichiometric phases prefer pairs of columns of edge-sharing octahedra, rather than the sheets seen in the misfit compounds. Despite this difference, there is experimental evidence that these two findings are compatible. Wiegers and Meerschaut synthesized (LaS)$_{1+x}B$S$_2$ (B = Ti, V, and Cr) misfits under atmospheric pressure conditions.[114] Kikkawa *et al.* formed stoichiometric LaBS$_3$ in the edge-sharing NH$_4$CdCl$_3$ phase for the same B species by applying high pressure to the mixture of reactants.[115] Thus, the elevated pressure synthesis method of Kikkawa *et al.* is probably necessary for the stoichiometric ABS$_3$ formation of the systems containing A = Pb, Sn, and B = Ti.

The compounds in our study in which the A cations have a lone pair configuration, (and with B not equal to Zr), also have another common feature. Our calculations show that several of them transition from the edge-sharing phase to the mixed motif edge- and corner-sharing phases at similar temperatures: 1150 K, 1120 K, and 1420 K for PbTiS$_3$, BiScS$_3$, and BiYS$_3$ respectively. TlNbS$_3$ has the same phase transition at a higher temperature, 1960 K. As well, CaTiS$_3$, which does not have a lone pair for A = Ca, also exhibits the potential for this transformation, at 305 K.

In order to evaluate our results for the six compounds which are found to have the face-sharing motif as the lowest energy phase, we separate them into two groups: five with Group I A = (Cs, Rb, and K), which have not been made experimentally in any phase, and BaTiS$_3$, which has been synthesized by multiple research groups. The face-sharing ground state of these Group I compounds is similar to the related face-sharing structures of ABCl$_3$, with different B. They do not have the $Pbcm$ structural motif of their ABO$_3$

analogs, (single columns of corner-sharing tetrahedra for B = V), nor the double columns of edge-sharing octahedra for B = Nb. This indicates that the face-sharing motif is not only a function of size of Group I A, but a function of the X size as well: both Cl^- and S^{2-} are very large and quite close in size in different environments: their ionic radii are 1.81 and 1.84 Å respectively, when adopting a coordination of 6;[61, 106] and their covalent radii are 0.99 and 1.02 Å respectively.[116] A notable difference between the sulfides and their chloride analogs is that the latter form mostly in a hexagonal lattice, rather than an orthorhombic one. An interesting exception is $RbCrCl_3$, which is nearly orthorhombic at room temperature with a monoclinic classification and an angle deviation from 90° of ≈3°.[117] In conjunction with this observation, we have found that the lowest energy phase for $RbNbS_3$ is also monoclinic albeit with a smaller angle deviation from 90°, 90.67°.

For the lone Group II A that assumes a face-sharing ground state, $BaTiS_3$, we find that it prefers the orthorhombic $C222_1$ space group. In the experimental literature, on the other hand, it is listed in one of two hexagonal space groups, $P6_3/mmc$ or $P6_3mc$.[95, 118, 119] However, Clearfield has noted that at lower temperatures of synthesis (≈970 K), the compound could be characterized with either orthorhombic or hexagonal indexing.[95] As the synthesis temperature was increased to 1370 K, only hexagonal characterization was plausible. Thus, similarly to $SrZrS_3$, the structure of $BaTiS_3$ is sensitive to changes in the synthesis temperature. Further, both Fagot *et al.* and Ghedira *et al.* have shown experimentally that an analog of $BaTiS_3$, $BaVS_3$, undergoes a phase change from hexagonal $P6_3/mmc$ phase to an orthorhombic phase (either $Cmc2_1$ or $C222_1$) when temperature is lowered below ≈250 K.[102, 103] Since our DFT calculations are performed at 0 K, our $BaTiS_3$ results are consistent with their findings and also explain the calculated preferred orthorhombic phases as opposed to hexagonal phases for the Group I face-sharing compounds. Fagot *et al.* proposed that $BaVS_3$ changes to a $C1m1$ phase as the temperature is lowered below 70 K.[102] To test whether this phase was possible for $BaTiS_3$, we per-

formed a relaxation of $BaTiS_3$ assuming the $C1m1$ phase and found that it was slightly lower in energy (ΔE $<$ 0.002 eV/20-atom unit cell) than the previously calculated $C222_1$ ground state; however, the Γ-point phonon calculation showed that this phase was not stable at 0 K. These analyses also demonstrate one limitation of our work: when many phases are similar in energy, our free energy approximation can reorder the phases.

As is shown in Table 5.5, the mixed motif face- and corner-sharing phases for $BaTiS_3$ energy levels fall between the wholly face-sharing phases and the wholly corner-sharing phases. The compound's oxide analog, $BaTiO_3$, is most often cited to be a corner-sharing phase compound. It is worthy of note that $BaTiO_3$ has also been processed in the $1/3$ phase, which is more formally known as the $BaFeO_{2+x}$ phase.[120-122] Thus, our results are consistent with the literature analogs. More importantly though, our calculations indicate that phase changes are possible from face- to corner-sharing motifs, as we calculate transition temperatures from the $C222_1$ phase to the $R3mR$, $Pm3m$, and $P4mm$ phases in the 340-375 K range. Based on the DFT calculations, we propose that $BaTiS_3$ will be found to be a highly structurally flexible material when synthesized by different experimental methods.

5.6 Conclusions

From a set of 22 phases known for ABX_3 compounds, we found that, for ABS$_3$ compounds in which the B element has a d^0 electronic configuration, the preferred phase for all but the largest A cations and smallest B cations are the edge-sharing $Pna2_1$ and NH_4CdCl_3 $Pnma$ phases. These sulfides differ from their oxide counterparts, which favor corner-sharing phases. To predict the preferred structural motifs, we developed a modified Goldschmidt tolerance factor t'. This incorporates the electronegativity difference between the A cation and S, but retains the original t for oxides, by normalizing the difference in electronegativity between the A cation and O. This formulation leads to a neat demarcation between the

compounds that prefer a face-sharing ground state and those that prefer an edge-sharing one.

Several of the ABS$_3$ combinations have phases with different motifs that are within 1 eV/20- atom unit cell of the energy of the ground state phase. Vibrational entropy calculations show that these phases might be achievable under different synthesis conditions than the ones already present in the literature. For the smaller A and B cation combinations in ABS$_3$, high synthesis temperatures under ambient pressure conditions, often with oxide intermediates or binary oxide starting materials, have led to products with the corner-sharing motif forming or to incommensurate phases. Experimental evidence shows that combinations of high pressure, lower processing temperatures, non-oxide starting materials, and long processing times tend to favor the synthesis of the commensurate edge-sharing motif. We suggest that two of the sulfides that are evaluated in this paper, ($BaZrS_3$ and $CaZrS_3$), are candidate compounds that may be produced as edge-sharing phases in this manner. Conversely, though $PbZrS_3$ and $SnZrS_3$ have been synthesized as edge-sharing compounds, higher synthesis temperatures could produce corner- and mixed motif corner- and edge-sharing phases. Lastly, $BaTiS_3$ might achieve both hexagonal and orthorhombic face-sharing motifs and corner-sharing motifs when subjected to different synthesis temperatures. Thus, not only does the family of ABS$_3$ compounds show structural diversity, but even the individual ABS$_3$ compounds themselves exhibit structural diversity with multiple stable phases.

5.7 Acknowledgements

JAB was supported by the Office of Naval Research, under grant N00014-12-1-1033. JWB and MRS were supported by the AFOSR, under grant FA9550-10-1-0248. IG was supported by the National Science Foundation, under grant DMR11-24696. AMR was sup-

ported by the Department of Energy Office of Basic Energy Sciences, under grant number DE-FG02-07ER46431. Computational support was provided by the HPCMO of the U.S. DoD and the NERSC of the DoE.

Chapter 6

Summary and Future Directions.

In two of the three cases that have been presented, it has been shown that compounds containing the chalcogens S and Se have potential applications in the field of photovoltaics, as they meet the symmetry and band gap requirements necessary to generate photo-currents when subjected to solar energy within the visible spectrum via the phenomenon known as the bulk photovoltaic effect (BPVE). In Chapter 3, it was shown that substituting S for O to create solid solutions of $PbTiO_{3-x}S_x$ reduces the band gap of the parent compound, $PbTiO_3$, into the visible range while maintaining the BPVE polarization requirement. In Chapter 4, it was demonstrated that it may be very fruitful to use non-oxide, non-perovskite polar materials for BPVE as they can be designed, through electronegativity considerations, with band gaps that capture the majority of the solar spectrum, between 1-2 eV. The third case presented demonstrated that sulfides in the $AB\mathrm{S}_3$ family of compounds may not be fully characterized due to the use of oxide synthesizing conditions of high temperatures and short hold times, and that the characterization statistic, the Goldschmidt tolerance factor, does not describe this family $in\ toto$, but is a construct of only the oxide $AB\mathrm{O}_3$ family. Using chemical knowledge of electronegativity, it was shown that a new statistic could describe $AB\mathrm{S}_3$ while still describing $AB\mathrm{O}_3$: by expanding the range of elements and com-

pounds considered for ABX_3, hidden symmetries have been exposed. Further, it has been shown that DFT is a useful tool that can be used to predict multiple stable phases of known compounds. The discovery of the experimenters Lee $et\ al.$[101] in which the compound $SrZrS_3$ was made as an edge-sharing compound through the use of lower synthesis temperatures, in contrast to its prior characterization as solely a corner-sharing compound, lends credence to this work.

Given the high shift current responses of the $LiAsS_2$, $LiAsSe_2$, and $NaAsSe_2$ compounds relative to the oxide perovskites, future work evaluating other already-synthesized compounds in the polar monoclinic and triclinic phases is warranted. As well, theoretical compounds – both oxide and non-oxide – should be considered in order to gain an understanding for what combinations of elements lead to high shift current responses. In this manner, the hypothesis suggested in Chapter 4, that covalent interactions coupled to band structures with disperse p-orbitals at the conduction and valence band edges play a major role in obtaining high shift current responses, can be proven, or disproven. Further, it will also provide the database required to ascertain whether or not chain-like motifs between atoms play a role as well. Finally, a large enough database might provide enough information to determine the size of polarization needed to produce a response: is there a limit to how low the polarization can be?

The suggestion to evaluate theoretical compounds is not vacuous. As was shown in Chapter 5, several sulfides classified as corner-sharing compounds in the literature actually have ground states conforming to an edge-sharing phase. While these compounds with the ground state edge-sharing phase are for the most part centrosymmetric $Pnma$, some do have the polar phase $Pna2_1$. The point here is not that these compounds have BPVE possibilities, though. It is that there exist other families of compounds which have related polar and non-polar phases. Consider the polar monoclinic phases examined in this study, Cc and Pc. Overall, there are another approximately 16 other compounds that have this

phase. Yes, these should be evaluated for the BPVE. Just as importantly, though, there are many compounds that have been synthesized in two centro-symmetric monoclinic space groups, $C2/c$ and $P2_1/c$ which differ from Cc and Pc only in that the latter lack inversion symmetry. A few compounds have even been synthesized in both the centrosymmetric and non-centrosymmetric phases, $e.\ g.$ the compound Cd_2P_3Cl. This compound has been synthesized by chemical transport in both the $C2/c$ and the Cc phases. The first phase was achieved using starting chemicals Cd, P, and PCl_3 with hot end/cold end temperatures of 700 °C/300 °C.[123] The second phase was achieved using starting chemicals $CdCl_2$ and CdP_2 with hot end/cold end temperatures of 620 °C/590 °C.[124] As well, even one of the compounds analyzed in this thesis, $LiAsSe_2$ has been made both as a polar compound and as a centrosymmetric compound: the former when slow a cooling rate is used; the latter when quenched.[16] Thus, these two sets of experimental results suggest that perhaps other compounds might be able to be made in other phases, too. The theoretician can return the favor to the experimental community by providing guidance as to which of those chemical formulae that have only been listed in centrosymmetric space groups or non-polar piezoelectric space groups, should be attempted to be made in non-centrosymmetric polar groups by showing which compounds in the non-centrosymmetric polar phase will have worthwhile values for band gaps, polarization, and shift current responses.

Additionally as many compounds are being processed as thin films that are synthesized on substrates with non-matching lattice sizes, they are often formed either tension or compression states. Compressive strain conditions can lead to non-pyroelectric piezoelectrics and centrosymmetric structures becoming polar, and thus, they might have significant BPVE responses. These conditions are simple to model and evaluate with first-principles calculation and post-DFT tools.

The suggestions for future work are enumerated as follows:

1. Investigate the BPVE response for the 16 other compounds in the Cc space group

which have p-block B-sites.

2. Calculate the expected structure of those centrosymmetric compounds in the $C2/c$ and $P2_1/c$ space groups. If they are determined to be polar, calculate the BPVE.

3. Expand the compound possibilities in the $AB\mathrm{S}_3$ study by allowing the B site to have electron configurations other than d^0 and permitting d-block elements with filled f-shells.

In conclusion, solid state chemistry is a rich tapestry of variegated elemental threads – but it is an unfinished tapestry. By stepping back from what has been woven, one can find a bigger theme and weave new scenes.

Bibliography

[1] B. I. Sturman and V. M. Fridkin, ”The photovoltaic and photorefractive effects in noncentrosymmetric materials,” Gordon and Breach Science Publishers, Philadephia, PA, USA (1992).

[2] K. Momma and F. Izumi, VESTA graphics software package: Visualization for Electronic and Structural Analysis, V. 2.1.6, (2011).

[3] J. E. Sipe and A. I. Shkrebtii, Phys. Rev. B **61**, 5337 (2000).

[4] S. M. Young, F. Zheng, and A. M. Rappe, Phys. Rev. Let. **109**, 236601 (2012).

[5] R. von Baltz and W. Kraut, Phys. Rev. B **23**, 5590 (1981).

[6] A. Bhatnagar, A. R. Chaudhuri, Y. H. Kim, D. Hesse and M. Alexe, Nature Comm. **4**, 2835-1 (2013).

[7] J. W. Bennett, I. Grinberg, and A. M. Rappe, J. Am. Chem. Soc. **130**, 17409 (2008).

[8] I. Grinberg, D. V. West, M. Torres, G. Gou, D. M. Stein, L. Wu, G. Chen, E. M. Gallo, A. R. Akbashev, P. K. Davies, J. E. Spanier, and A. M. Rappe, Nature **503**, 509 (2013).

[9] I. Marozau , M. Dobelli, T. Lippert, D. Logvinovich, M. Mallepell, A. Shkabko, A. Weidenkaff, and A. Wokaun, Appl. Phys. A **89**, 933 (2007).

[10] Y.-I. Kim, P. M. Woodward, K. Z. Baba-Kishi, and C. W. Tai Chem. Mater. **16**, 1267 (2004).

[11] M. Yashima, M. Saito, H. Nakano, T. Takata, K. Ogisu, K. Domen, Chem. Comm. **46**, 4704 (2010).

[12] T. Kosugi, K. Murakami, and S. Kaneko, Thin-Film Structures for Photovoltaics. Symposium, 273 (1998).

[13] N. Barreau, J. C. Bernede, S. Marsillac, and A. Mokrani, J. of Cryst. Growth **235**, 439 (2002).

[14] K. Ogisu, A. Ishikawa, Y. Shimodaira, T. Takata, H. Kobayashi, and K. Domen, J. Phys. Chem. C **112**, 11978 (2008).

[15] M. Fleischer, ed. ”Data of Geochemistry,” 6th Ed., Chapter 6,” U. S. Govt. Printing Office (1967).

[16] T. K. Bera, Joon I. Jang, J.-H. Song, C. D. Malliakas, A. J. Freeman, J. B. Ketterson, and M. G. Kanatzidis, J. Amer. Ceram. Soc. **132**, 3848 (2010)

[17] V. M. Goldschmidt, Die Naturwissenschaften **21**, 477 (1926).

[18] B. D. Cullity and S. R. Stock “Elements of X-Ray Diffraction,” Third Edition, Prentice Hall, Upper Saddle River, New Jersey, USA (2001).

[19] J. F. Nye, ”Physical Properties of Crystals,” Clarendon Press, Oxford, UK (1985).

[20] N. W. Ashcroft and N. D. Mermin, ”Solid State Physics,” Thomson Learning, Inc., United States of America, (1976).

[21] T. Hahn ”International Tables for Crystallography, Volume A, Space-Group Symmetry,” Ed.: T. Hahn, Fourth edition revised, Kluwer Academic Publishers, Boston, MA, USA (1996).

[22] R. M. Martin ”Electronic Stucture: Basic Theory and Practical Methods,” Cambridge Univeristy Press, Cambridge, UK (2004).

[23] M. Born and J. R. Oppenheimer, Ann. Phys. **84**, 457 (1927).

[24] P. Hohenberg and W. Kohn, Phys. Rev. B **136**, 864 (1964).

[25] W. Kohn and L. J. Sham, Phys. Rev. A **140**, 1133 (1965).

[26] K. Capelle Brazilian J. of Phys. **36** 1318 (2006).

[27] ABINIT website, http://www.abinit.org/documentation.

[28] F. Bloch, Z. Physik **52**, 555 (1928).

[29] D. R. Hamann, M. Schlueter, and C. Chiang, Phys. Rev. Lett **43**, 1494 (1979).

[30] N. J. Ramer and A. M. Rappe, Phys. Rev. B **59**, 12471 (1999).

[31] V. I. Anisimov, ”Strong Coulomb Correlations in Electronic Structure Calculations: Beyond the local density approximation,” Ed.: V. I. Anisimov, Gordon and Breach Science Publishers, Amsterdam, (2000).

[32] M. Cococcioni and S. de Gironcoli, Phys. Rev B **71**, 035105-1 (2005).

[33] G. Y. Gou, J. W. Bennett, H. Takenaka, and A. M. Rappe, Phys. Rev. B **83**, 205115 (2011).

[34] J. P. Perdew, M. Ernzerhof, and K. Burke, J. Chem. Phys. **105**, 9982 (1996).

[35] A. D. Becke, J. Chem. Phys. **98**, 5648 (1993).

[36] L. Hedin, Phys. Rev A. **139**, 796 (1965).

[37] F. Bruneval, N. Vast, and L. Reining, Phys. Rev. B **74**, 045102 (2006).

[38] D. A. McQuarrie ”Statistical Mechanics,” United Science Books, Sausalito, (2000).

[39] S. Teshima, H. Kashiwabara, K. Masamoto, K. Kikunaga, K. Takeshita, T. Okuda, K. Sakurai, S. Ishizuka, A. Yamada, K. Matsubara, S. Niki, Y. Yoshimura, and N. Terade, Mat. Res. Soc. Symp. Proc. **1012**, 1012-Y03-19 (2007).

[40] Y. Ohsita, H. Suzuki, N. Kojima, T. Tanaka, T. Honda, M. Inagaki, M. Yamaguchi, J. of Cryst. Gr. **318**, 328 (2011).

[41] S. R. Basu, L. W. Martin, Y. H. Chu, M. Gajek, R. Ramesh, R. C. Rai, X. Xu, and J. L. Musfeldt, Appl. Phys. Lett. **92**, 091905 (2008).

[42] G. Zhang, H. Wu, G. Li, Q. Huang, C. Yang, F. Huang, F. Liao, and J. Lin, Scientific Reports **3**, 1723-1 (2013).

[43] W. S. Choi, M. F. Chisholm, D. J. Singh, T. Choi, G. E. Jellison, Jr., and Ho N. Lee, Nature Comm. **3**, 689-1 (2012).

[44] C. H. Peng, J-F. Chang, and S. B. Desu, Mat. Res. Soc. Symp. Proc. **243**, 21 (1992).

[45] M. P. Moret, M. A. C. Devillers, K. Woerhoff, P. K. Larsen, J. of Appl. Phys. **92**, 468 (2002).

[46] D. Bao, X. Yao, N. Wakiya, K. Shinozaki, and N. Mizutani, Mat. Sci. and Eng. **B94**, 269 (2002).

[47] I. Grinberg and A. M. Rappe, Phys. Rev. B **70**, 220101 (2004).

[48] R. Asahi, T. Morikawa, T. Ohwaki, K. Aoki, and Y. Taga, Science **293**, 269 (2001).

[49] A. Ishikawa, T. Takata, T. Matsumura, J. N. Kondo, M. Hara, H. Kobayashi, and K. Domen, J. Phys. Chem. B **108**, 2637 (2004).

[50] O. J. Rutt, T. L. Hill, Z. A. Gal, M. A. Hayward, and S. J. Clarke, Inorg. Chem. **42**, 7906 (2003).

[51] D. O. Charkin, A. V. Sadakov, O. E. Omelyanovskii, and S. M. Kazakov, Mat. Res. Bull. **45**, 2012 (2010).

[52] W. J. Zhu and P. H. Hor, J. of Sol. St. Chem. **153**, 26 (2000).

[53] G. Hyett, Z. A. Gal, C. F. Smura, and S. J. Clarke, Chem. Mater. **20**, 559 (2008).

[54] V. Meignen, L. Cario, A. Lafond, Y. Moelo, C. Guillot-Deudon, and A. Meerschaut, J. of Sol. St. Chem. **177**, 2810 (2004).

[55] C. F. Smura, D. R. Parker, M. Zbiri, M. R. Johnson, and Z. A. Gal, J. Amer. Chem. Soc. **133**, 2691 (2011).

[56] X. Gonze, J.-M. Beuken, R. Caracas, F. Detraux, M. Fuchs, G.-M. Rignanese, L. Sindic, M. Verstraete, G. Zerah, F. Jollet, M. Torrent, A. Roy, M. Mikami, Ph. Ghosez, J.-Y. Raty, and D. C. Allan, Comp. Mat. Sci. **25**, 478 (2002).

[57] P. Giannozzi, S. Baroni, N. Bonini, M. Calandra, R. Car, C. Cavazzoni, D. Ceresoli, G. L. Chiarotti, M. Cococcioni, I. Dabo, A. Dal Corso, S. de Gironcoli, S. Fabris, G. Fratesi, R. Gebauer, U. Gerstmann, C. Gougoussis, A. Kokalj, M. Lazzeri, L. Martin-Samos, N. Marzari, F. Mauri, R. Mazzarello, S. Paolini, A. Pasquarello, L. Paulatto, C. Sbraccia, S. Scandolo, G. Sclauzero, A. P. Seitsonen, A. Smogunov, P. Umari and R. M. Wentzcovitch, J. of Phys.: Cond. Matter **21**, 395502 (2009).

[58] A. M. Rappe, K. M. Rabe, E. Kaxiras, and J. D. Joannopoulos, Phys. Rev. B **41**, 1227 (1990).

[59] http://opium.sourceforge.net.

[60] H. J. Monkhorst and J. D. Pack, Phys. Rev. B **13**, 5188 (1976).

[61] R. Seshadri, http://www.mrl.ucsb.edu/ seshadri/Periodic/index.html.

[62] H. T. Stokes, http://stokes.byu.edu/findsym.html.

[63] H. T. Stokes and D. M. Hatch, J. Appl. Cryst. **38**, 237 (2005).

[64] A. M. Glazer, Acta Cryst. **B28**, 3384 (1972).

[65] L. Hedin, Phys. Rev. **139**, A796 (1965).

[66] S. Lebegue, B. Arnaud, M. Alouani, and P. E. Bloechl, Phys. Rev. B **67**, 155208 (2003).

[67] V. I. Anisimov, "Strong Coulomb Correlations in Electronic Structure Calculations," Gordon and Breach, Amsterdam, The Netherlands, (2000).

[68] G. Henkelman, A. Arnaldsson, and H. Jonsson, Comp. Mat. Sci. **36**, 354 (2006).

[69] A. Arnaldsson, W. Teng, S. Chill, G. Henkelman, http://theory.cm.utexas.edu/bader.

[70] S. Piskunov, E. Heifets, R. I. Eglitis, and G. Borstel, Comp. Mat. Sci. **29**, 165 (2004).

[71] B. Meyer, J. Padilla, and D. Vanderbilt, Faraday Discussions **114**, 395 (1999).

[72] G. Saghi-Szabo, R. E. Cohen, and H. Krakauer, Phys. Rev. B **59**, 12771 (1999).

[73] I. M. N. Meerschaut, C. Auriel, and J. Rouxel, J. of Alloys and Compounds **183**, 129 (1992).

[74] M. Lach-hab, D. A. Papaconstantopoulos, and M. J. Mehl, J. of Phys. and Chem. of Solids **63**, 833 (2002).

[75] N. S. Dantas, A. F. da Silva, and C. Persson, Optical Materials **30**, 1451 (2008).

[76] N. Sato, A. Kirishima, J. of Nuclear Mat. **414** 324 (2011).

[77] J. Cuya, N. Sato, K. Yamamoto, H. Takahashi, and A. Muramatsu, Thermochimica Acta **419**, 215 (2004).

[78] O. M. Saad, T. Kuzuya, S. Hirai, and M. Ohta, Matls. Trans. **51**, 2289 (2010).

[79] R. Lelieveld and D. J. W. Ijdo, Acta Cryst. B **36** 2223 (1980).

[80] http://webbook.nist.gov/chemisry, NIST Chemistry Webbook, U. S. Secretary of Commerce.

[81] S. M. Young and A. M. Rappe, Phys. Rev. Let. **109**, 116601 (2012).

[82] F. S. Chen, J. Appl. Phys. **40**, 3389 (1969).

[83] W. T. H. Koch, R. Munser, W. Ruppel, and P. Wurfel, Ferroelectrics **13**, 305 (1976).

[84] T. Choi, S. Lee, Y. Choi, V. Kiryukhin, and S.-W. Cheong, Science **324**, 63 (2009).

[85] W. Ji, K. Yao, and Y. C. Liang, Adv. Mater. **22**, 1763 (2010).

[86] J. P. Chakrabartty, R. Nechache, C. Harnagea, and F. Rosei, Optics Express **22** A80 (2014).

[87] R. Nechache, C. Harnagea, S. Licoccia, E. Traversa, A. Ruediger, A. Pignolet, and F. Rosei, Applied Phys. Lett. **98**, 202902 (2011).

[88] A. Belsky, M. Hellenbrandt, V. L. Karen, and P. Luksch, Acta Cryst. B **58**, 364 (2002).

[89] FIZ Karlsruhe ICSD Database Data Release 2013.2.

[90] Bilbao Crystallographic Server http://www.cryst.ehu.es

[91] A. M. Glass, D. von der Linde, and T. J. Negran, Phys. Lett. **25**, 233 (1974).

[92] W. Ji, K. Yao, and Y. C. Liang, Phys. Rev. B **84**, 094115 (2011).

[93] J. Wang, J. B. Neaton, H. Zheng, V. Nagarajan, S. B. Ogale, B. Liu, D. Viehland, V. Vaithyanathan, D. G. Schlom, U. V. Waghmare, N. A. Spaldin, K. M. Rabe, M. Wuttig, and R. Ramesh, Science **299**, 1719 (2003).

[94] O. Muller and R. Roy, "The Major Ternary Structural Families," Springer-Verlag, New York, NY, USA (1974).

[95] A. Clearfield, Acta Cryst. **16**, 135 (1963).

[96] P. M. Woodward, Acta Cryst. **B53**, 44 (1997).

[97] J. B. Goodenough, Rep. Prog. Phys. **67**, 1915 (2004).

[98] D. G. Pettifor, Sol. St. Comm. **51**, 31 (1984).

[99] R. Ferro and A. Saccone, "Physical Metallurgy," 4th Ed., edited by R. W. Cahn and P. Haasen, Elsevier Science, Amsterdam, The Netherlands, (1996), Vol. I, Chap. 4.

[100] D. G. Pettifor, Mat. Sci. and Tech., **4**, 675 (1988).

[101] C.-S. Lee, K. M. Kleinke, and H. Kleinke, Sol. St. Sci. **7**, 1049 (2005).

[102] S. Fagot, P. Foury-Leylekian, S. Ravya, J. P. Pouget, M. Annec, G. Popov, M. V. Lobanov, M. Greenblatt, Sol. St. Sci. **7**, 718 (2005).

[103] M. Ghedira, J. Chenavas, F. Sayetat, M. Marezio, O. Massenet, and J. Mercier, Acta Cryst. **B37**, 1491 (1981).

[104] M. Murakami, K. Hirose, K. Kawamura, N. Sata, and Y. Ohishi, Science **304**, 855 (2004).

[105] C. D. Martin, R. I. Smith, W. G. Marshall, and J. B. Parise, Amer. Mineralogist **92**, 1912 (2007).

[106] R. D. Shannon, Acta Cryst. **A32**, 751 (1976).

[107] J. W. Bennett, I. Grinberg, P. K. Davies, and A. M. Rappe, Phys. Rev. B **83**, 144112 (2011).

[108] W. B. Pearson, J. Phys. Chem. Solids **23**, 103 (1962).

[109] A. S. Bhalla, R. Guo, and R. Roy, Mat. Res. Innovat. **4**, 3 (2000).

[110] R. L. Lelieveld and D. J. W. Ijdo, Acta Cryst. **B34**, 3348 (1978).

[111] S. Yamaoka, J. Of Amer. Cer. Soc. **55**, 111 (1972).

[112] A. Meetsma, A. Wiegers, and J. L. DeBoer, Acta Cryst. **C49**, 2060 (1993).

[113] J. W. Bennett, I. Grinberg, A. M. Rappe, Phys. Rev. B **79**, 235115 (2009).

[114] G. A. Wiegers and A. Meerschaut, J. of Alloys and Comp. **178**, 351 (1992).

[115] S. Kikkawa, Y. Fujii, Y. Miyamoto, F. Kanamaru, A. Meerschaut, A. Lafond, and J. Rouxel, J. of Sol. St. Chem. **139**, 233 (1998).

[116] R. T. Sanderson, "Chemical Periodicity," Reinhold Publishing Corp., New York, NY, USA (1962).

[117] H. W. Zandbergen and D. J. W. Ijdo, J. of Sol. St. Chem. **38**, 199 (1981).

[118] L. A. Aslanov and L. M. Korba, Russ. J. Inorg. Chem. **9**, 1317 (1964).

[119] J. Huster Zeitshrift for Naturforschung **35**, 775 (1980).

[120] J. Akimoto, Y. Gotoh, and Y. Oosawa, Inorganic Compounds C **50**, 160 (1994).

[121] R. D. Burbank and H. T. Evans, Jr., Acta. Cryst. **1**, 330 (1948).

[122] M. Yashima, T. Hoshina, D. Ishimura, S. Kobayashi, W. Nakamura, T. Tsurumi, and S. Wada, J. of App. Phys. **98**, 014313 (2005).

[123] P. C. Donohue J. of Sol. St. Chem. **5**, 71 (1972).

[124] A. Rebbah, J. Yazbeck, R. Lande, and A. Deschanvres, Mat. Res. Bull. **16**, 525 (1981).